Phase stabilization of field-distributed quantum states for fiber-based continuous-variable QKD protocols

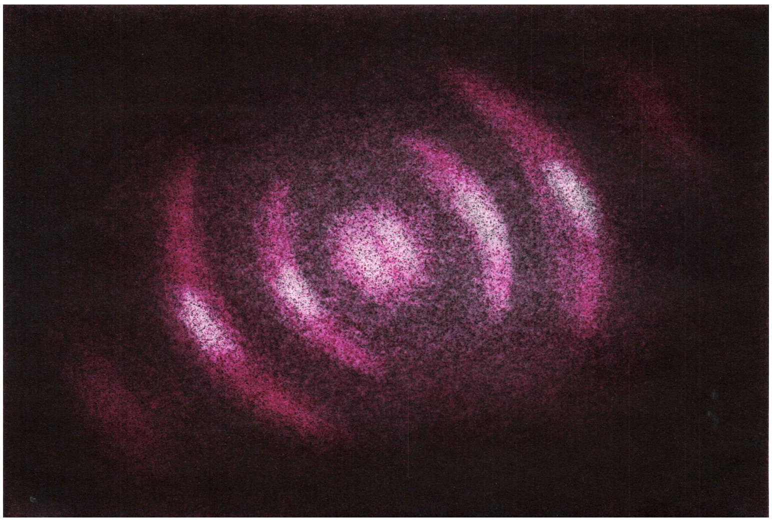

Sophie R. Verclas

2026

Phase stabilization of field-distributed quantum states for fiber-based continuous-variable QKD protocols

Dissertation
zur Erlangung des Doktorgrades
an der Fakultät für Mathematik, Informatik und Naturwissenschaften
Fachbereich Physik
der Universität Hamburg

vorgelegt von

Sophie R. Verclas

Hamburg

2026

Gutachter der Dissertation:	Prof. Dr. Roman Schnabel Prof. Dr. Ludwig Mathey
Zusammensetzung der Prüfungskommission:	Prof. Dr. Roman Schnabel Prof. Dr. Ludwig Mathey Prof. Dr. Robin Santra Prof. Dr. Dieter Horns Dr. Christoph Becker
Vorsitzender der Prüfungskommission:	Prof. Dr. Robin Santra
Datum der Disputation:	17.07.2026
Vorsitzender Fach-Promotionsausschuss Physik:	Prof. Dr. Johannes Haller
Leiter des Fachbereichs Physik:	Prof. Dr. Markus Drescher
Dekan der Fakultät MIN:	Prof. Dr. - Ing. Norbert Ritter

Abstract

Squeezed light is a key resource that exhibits quantum correlations and is subject of current research and application. First described in 1970, squeezed light is used today in gravitational wave detectors and is being researched and developed for fields such as quantum sensing, quantum communication, and photonic quantum computers. By overlapping the outputs of two squeezed light sources, entangled states are created that exhibit quantum correlated results of quadrature measurement. Together with the no-cloning theorem, these two properties form a basis for the realization of continuous-variable quantum key distribution. The potential key rate is proportional to the bandwidth of the generated squeezed states. For this reason, monolithic squeezed light resonators with GHz bandwidth were chosen for this work.

The focus of this dissertation is on the distribution and phase stabilization of squeezed vacuum states and entangled (two-mode squeezed) states, which were distributed over a noisy fiber channel of one kilometer length to another building. To compensate for environmental disturbances, I developed and implemented control loops based on the principle of a quantum noise lock. In a first application, the phase stabilization of squeezed vacuum states after 1 km of fiber transmission was demonstrated. Noise reduction of 4.7 dB at a sideband frequency of 30 MHz and over 2 dB above 1 GHz were measured, and a long-term measurement of five minutes was completed. In a second step, I extended the scheme to include real-time synchronization and subtraction to stabilize the readout phase of spherically symmetric entangled states. Without distribution, a correlated noise reduction of approximately 4 dB was achieved, and approximately 3 dB with states distributed between two laboratories. The results show that the feedback control scheme is suitable for this application and exhibits no fundamental limitations. An extension to approximately 5 km of fiber length is possible, as is implementation in other applications such as distributed fiber sensing.

Kurzfassung

Gequetschtes Licht ist eine Schlüsseltechnologie, die Quantenkorrelationen zeigt und Gegenstand aktueller Forschung sowie Anwendung ist. Erstmals im Jahr 1970 beschrieben, wird gequetschtes Licht heute in Gravitationswellendetektoren eingesetzt und unter anderem für die Gebiete Quantensensorik, Quantenkommunikation und photonische Quantencomputer erforscht und entwickelt. Werden die Ausgänge zweier Quetschlichtquellen überlagert, entstehen verschränkte Zustände, die quantenkorrelierte Ergebnisse bei Quadraturmessungen aufweisen. Zusammen mit dem No-cloning Theorem bilden diese beiden Eigenschaften eine Grundlage für die Realisierung von Quantenschlüsselverteilung mit kontinuierlichen Variablen. Dabei ist die mögliche Schlüsselrate proportional zur Bandbreite der erzeugten gequetschten Zustände. Aus diesem Grund wurden für diese Arbeit monolithische Quetschlichtresonatoren mit GHz Bandbreite gewählt.

Der Fokus dieser Dissertation liegt auf der Verteilung und Phasenstabilisierung von gequetschten Vakuumzuständen und verschränkten (zwei Moden gequetschten) Zuständen, die über einen rauschbehafteten Faserkanal mit einem Kilometer Länge in ein anderes Gebäude verteilt wurden. Um die umweltbedingten Störeinflüsse zu kompensieren, habe ich Regelschleifen nach dem Schema eines quantum noise locks entwickelt und implementiert. In einer ersten Anwendung wurde die Phasenstabilisierung von gequetschtem Vakuum nach 1 km Fasertransmission gezeigt. Dabei habe ich eine nichtklassische Rauschunterdrückung von 4.7 dB bei 30 MHz Seitenbandfrequenz sowie über 2 dB oberhalb von 1 GHz gemessen und eine Langzeitmessung von fünf Minuten abgeschlossen. In einem zweiten Schritt habe ich das Schema um Echtzeitsynchronisierung und -subtraktion erweitert, um die Auslesephase von kreissymmetrischen verschränkten Zuständen zu stabilisieren. Ohne Verteilung konnte ich eine korrelierte Rauschunterdrückung von etwa 4 dB erreichen und mit zwischen zwei Laboren verteilten Zuständen etwa 3 dB. Die Ergebnisse zeigen, dass das Schema für diese Anwendung geeignet ist und keine fundamentalen Limitierungen aufweist. Eine Erweiterung zu ca. 5 km Faserlänge ist ebenso möglich wie die Implementierung in anderen Anwendungen wie z.B. verteilter Fasersensorik.

Contents

Acronyms

ADC Analog-Digital Converter

BHD Balanced Homodyne Detector

CV Continuous Variable

CV-QKD Continuous-Variable Quantum Key Distribution

DAQ Data Acquisition

DM Dichroic Mirror

DMC Diagnostic Mode Cleaner

DV Discrete Variable

ENT Entanglement

EOM Electro-Optical Modulator

EPR Einstein-Podolsky-Rosen

FG Frequency Generator

FPGA Field-Programmable Gate Array

FSR Free Spectral Range

HF High Frequency

IQP Institut für Quantenphysik

KTP Potassium Titanyl Phosphate

LF Low Frequency

LO Local Oscillator

osdi one-sided device-independent

PBS Polarizing Beam Splitter

PC Polarization Controller

PCB Printed Circuit Board

PD Photo Diode

PDC Parametric Down-Conversion

PID Proportional-Integral-Derivative

ppKTP Periodically Poled KTP

PS Phase Shifter

QKD Quantum Key Distribution

QRNG Quantum Random Number Generator

SHG Second Harmonic Generation

SNR Signal-to-Noise Ratio

SQZ Squeeze Laser

ZOQ Zentrum für optische Quantentechnologien

CHAPTER 1

Introduction

From a historical perspective, secure communication is a very old topic that was already of concern to the ancient Greeks and Romans. Cryptosystems were developed in almost all cultures with famous examples like the Caesar cipher and the Enigma machine, constantly increasing the security level over time. Nowadays, encryption methods are at the core of modern society, not only in emails or text messages but more importantly in applications like online banking or sensitive data traffic. Currently, the security is based on mathematical complexity, i.e. on algorithms which require either a lot of computational power and/or computational time to be decoded, making them very unlikely to be successfully attacked and decrypted by a malicious third party within a meaningful time. However, the increasing performance of classical computers and the development of quantum computers make a decryption of established algorithms more likely.

Quantum key distribution (QKD) offers a different approach to share a secret message between two or more parties. Instead of computationally complex algorithms, the security is based on principles of quantum physics. Specifically, the properties of entanglement, real (quantum) randomness, and the no-cloning theorem [Woo+82; Par70] make it an extremely powerful tool to not only exchange a secret key but also reveal any eavesdropper trying to intercept it. The first QKD protocol was proposed in 1984 by Bennett and

Brassard [Ben+14], using single photons with the information encoded in their polarization. Five years later, the first entanglement-based protocol was developed by A. Ekert [Eke91], originally with spin 1/2 particles. Today, discrete-variable (DV) protocols [Yan+24; Fol+22] as well as continuous-variable (CV) protocols using Gaussian states as in [Gro+03; Haj+24] are subject to research and commercialization, trying to maximize either the secret key rate or transmission distance or both. Transmission channels range from optical fibers [Zha+20; Che+21; Zah+24] to free space or satellite-based approaches [Yin+20; Eck+21; Lia+17; Hug+02; Urs+07]. Another source to generate entangled pairs for CV-QKD is squeezed light [Got+01; Cer+01; Ngu+26].

The first experimental demonstration of squeezed light was performed by Slusher et al. in 1985 [Slu+85] using four-wave mixing and only a year later by Kimble et al. [Wu+86] using degenerate parametric down-conversion in a nonlinear crystal, which is the state-of-the-art technique to generate squeezed light today. It took a bit more than two decades to further develop the systems and setup designs for observations of 10 dB and up to 15 dB of noise reduction in the following years [Vah+08; Sch+18; Vah+16]. Today, squeeze lasers with a squeeze factor of up to 10 dB are commercially available [Noi]. The properties of squeezed light in combination with their robustness and reproducibility led to the first implementation in gravitational wave detectors [Aba+11; Gro+13]. In 2019 AdvancedLIGO and AdvancedVIRGO received upgrades with squeezed light leading to the detection of a new event almost every week [Tse+19; Ace+19]. Other fields of research also discovered the potential use of squeezed light. It is used or proposed for biological measurements [Tay+13], quantum sensing [Gra+20; Kan+25], photonic quantum computers [Bra+05; End+25] and quantum key distribution [Mad+12; Geh+15]. Research on the transmission of squeezed light was conducted in 2014 through free space [Peu+14], and later shifted to a fiber-based approach, as it was shown that the coupling into single-mode fibers can be achieved with high efficiency [Meh+10]. In [Qin+19], a noise reduction of 2.5 dB after 1.6 km was measured, with the squeezed states and local oscillator being transmitted in the same fiber. [Sul+22] generated the local oscillator locally at the receiver side and measured 3.5 dB after a 1 km fiber. Distribution of two-mode squeezed states between two separated buildings was shown by [Cha+23] with up to 0.5 dB over a bandwidth of 12 MHz.

In this work, I used two sources of squeezed vacuum states ("squeeze lasers" [Sch+22] to generate entangled (two-mode squeezed) vacuum states for an entanglement-based continuous-variable QKD protocol, offering one-sided device-independence (osdiQKD) [Fur+12; Geh+15]. The condition for this level of security, that includes the proper functionality of the devices at the receiver side, is an overall detection loss smaller than 50 %. Especially for short distances of some kilometers, the secret key rate of QKD protocols can in general be improved by using CV instead of DV protocols [Pir+17], to maximize the bits per channel use. Our quantum channel for the transmission of the states is an optical fiber of 1 km length, which sets an upper limit to the transmission distance of four to five kilometers [Geh+15]. We use a second fiber of the same length for the transmission of the local oscillator. This experiment was set up before in a laboratory-only environment with the fibers spooled up under the optical table [Ebe13]. It did not experience any disturbances occurring outside of a clean room environment with temperature stabilization. To come closer to a real-world application, I distributed the states via a 1 km optical fiber to a second laboratory in a different building. This led to a high amount of phase noise in the measurement results of the remote station. Besides the implementation of the setup, I focused on the development of two feedback control loops. The first is for the phase stabilization of squeezed vacuum states, transmitted through the optical fiber link as a proof of concept for the quantum noise lock scheme [Ver+26]. The second is for the synchronization of the read-out phases from the two measurement stations in order to measure two-mode squeezed states in the same quadrature simultaneously with both detectors. This included the challenges of real-time synchronization of signals in the MHz regime. It was carried out on a Moku:Pro, a field-programmable gate array (FPGA)-based device with a high sampling rate and flexible tuning options. Together with the previous work by [Ebe13] and [Toh25], the successful phase stabilization in a noisy close-to-application setting made the realization of the protocol a feasible goal.

Structure of this thesis

This thesis contains the following parts:

Chapter 2 is a theoretical description of the physical principles used in this work. It includes the formalism for a quantized light field, nonlinear optical effects, squeezed and entangled states of light, quantum key distribution, feedback control theory and optical fiber theory.

Chapter 3 describes experimental methods of squeezed light generation and optical phase control schemes. It also summarizes the different steps of our quantum key distribution protocol.

Chapter 4 is an overview of the experimental setup in the two laboratories and a presentation of the fiber link.

Chapter 5 presents the long-term evaluation of the monolithic squeeze lasers used in this thesis.

Chapter 6 provides the results for the phase-stabilized distribution of squeezed vacuum states through the fiber link.

Chapter 7 demonstrates the phase-stabilized distribution of entangled (two-mode squeezed) states through the fiber link.

Chapter 8 gives a conclusion and discusses optimization ideas for the current setup. Also, the extension to a 5 km fiber link is analyzed here.

CHAPTER 2

Theoretical background

2.1 Quantization of the electromagnetic field

The classical description of light fields, primarily given by Maxwell's equations, does not cover quantum mechanical states of light. In this chapter, I introduce the most important states and formalisms, mainly following [Ger+05]. To derive the field energy or the Hamiltonian H of a single-mode field, we consider a one-dimensional cavity of length L with boundaries at $z = 0$ and $z = L$. It is confined by perfectly conducting walls and is free from any radiation sources or media. As the components of an electromagnetic field are orthogonal to each other and to the direction of propagation, we find the two components for a light field traveling in the z direction to be $\vec{E} = (E_x, 0, 0)$ and $\vec{B} = (0, B_y, 0)$, given by

$$E_x(z,t) = \sqrt{\frac{2\omega^2}{V\varepsilon_0}} q(t) \sin(kz), \tag{2.1}$$

$$B_y(z,t) = \left(\frac{\mu_0\varepsilon_0}{k}\right) \sqrt{\frac{2\omega^2}{V\varepsilon_0}} p(t) \cos(kz), \tag{2.2}$$

with the electric permittivity ε_0, the magnetic permeability μ_0, the frequency of the mode ω and the wave number k, satisfying $k = \frac{\omega}{c}$. Here $q(t)$ and $p(t)$

are the canonical position and momentum with $p(t) = \dot{q}(t)$. The Hamiltonian for this single-mode field is given by

$$H = \frac{1}{2} \int dV \left[\varepsilon_0 E_x^2(z,t) + \frac{1}{\mu_0} B_y^2(z,t) \right] \tag{2.3}$$

$$= \frac{1}{2} \left(p^2 + \omega^2 q^2 \right). \tag{2.4}$$

This is formally equivalent to a one-dimensional harmonic oscillator and the canonical variables q and p can be replaced by their Hermitian operator equivalents $\hat{q}$ and $\hat{p}$. They fulfill the commutation relation $[\hat{q}, \hat{p}] = i\hbar$ and lead to the Hamiltonian

$$\hat{H} = \frac{1}{2} \left(\hat{p}^2 + \omega^2 \hat{q}^2 \right). \tag{2.5}$$

2.1.1 Number states and ground state

It is convenient to introduce the annihilation operator $\hat{a}$ and the creation operator $\hat{a}^\dagger$, which are non-Hermitian and defined in terms of $\hat{q}$ and $\hat{p}$:

$$\hat{a} = \frac{1}{\sqrt{2\hbar\omega}} (\omega \hat{q} + i\hat{p}) \tag{2.6}$$

$$\hat{a}^\dagger = \frac{1}{\sqrt{2\hbar\omega}} (\omega \hat{q} - i\hat{p}) \tag{2.7}$$

These operators are useful for the description of a quantized field and fulfill the commutation relation $[\hat{a}, \hat{a}^\dagger] = 1$. The Hamiltonian can now be written as

$$\hat{H} = \hbar\omega \left(\hat{a}^\dagger \hat{a} + \frac{1}{2} \right). \tag{2.8}$$

The product $\hat{a}^\dagger \hat{a}$ defines the number operator $\hat{n}$, which has the number states $|n\rangle$ as eigenstates:

$$\hat{a}^\dagger \hat{a} |n\rangle = \hat{n} |n\rangle = n |n\rangle \tag{2.9}$$

with the eigenvalues $n \in [0, 1, 2, ..., \infty)$. The number states $|n\rangle$ are eigenstates of the Hamiltonian in equation (2.5)with the eigenvalues E_n:

$$\hat{H} |n\rangle = \hbar\omega \left(\hat{a}^\dagger \hat{a} + \frac{1}{2} \right) |n\rangle = E_n |n\rangle . \tag{2.10}$$

Applying the creation operator $\hat{a}^\dagger$ to the equation above, leads to

$$\hat{H}\hat{a}^\dagger |n\rangle = \hbar\omega \left(\hat{a}^\dagger \hat{a}^\dagger \hat{a} + \frac{1}{2}\hat{a}^\dagger \right) |n\rangle = E_n \hat{a}^\dagger |n\rangle , \tag{2.11}$$

which can be written as

$$\hbar\omega \left((\hat{a}^\dagger \hat{a} \hat{a}^\dagger - \hat{a}^\dagger) + \frac{1}{2}\hat{a}^\dagger \right) |n\rangle = E_n \hat{a}^\dagger |n\rangle \tag{2.12}$$

using the commutation relation $[\hat{a}, \hat{a}^\dagger] = 1$. We obtain for the creation operator and equivalently for the annihilation operator with the energy eigenvalue $(E_n \pm \hbar\omega)$:

$$\hat{H}\hat{a}^\dagger |n\rangle = \hbar\omega \left(\hat{a}^\dagger \hat{a} + \frac{1}{2} \right) (\hat{a}^\dagger |n\rangle) = (E_n + \hbar\omega)(\hat{a}^\dagger |n\rangle) \tag{2.13}$$

$$\hat{H}\hat{a} |n\rangle = \hbar\omega \left(\hat{a}^\dagger \hat{a} + \frac{1}{2} \right) (\hat{a} |n\rangle) = (E_n - \hbar\omega)(\hat{a} |n\rangle) \tag{2.14}$$

From this equation the names and physical interpretation of $\hat{a}$ and $\hat{a}^\dagger$ become apparent: Applied to a number state, they destroy or create one quantum of energy with the value $\hbar\omega$, which corresponds to the energy of a photon. This operation can be performed multiple times but as the energy can't become negative, the annihilation operator applied to the ground state gives

$$\hat{a} |0\rangle = 0. \tag{2.15}$$

The equation for the lowest energy eigenvalue therefore reads

$$\hat{H} |0\rangle = \hbar\omega \left(\hat{a}^\dagger \hat{a} + \frac{1}{2} \right) |0\rangle = \frac{1}{2}\hbar\omega |0\rangle \tag{2.16}$$

and leads to $E_0 = \frac{1}{2}\hbar\omega$, the zero-point energy of the ground state $|0\rangle$. Using the number operator introduced in equation (2.9) we can also calculate the energy eigenvalues E_n:

$$\hat{H} |n\rangle = \hbar\omega \left(\hat{a}^\dagger \hat{a} + \frac{1}{2} \right) |n\rangle = \hbar\omega \left(\hat{n} + \frac{1}{2} \right) |n\rangle = \hbar\omega \left(n + \frac{1}{2} \right) |n\rangle = E_n |n\rangle . \tag{2.17}$$

The energy eigenvalues $E_n = \hbar\omega\left(n + \frac{1}{2}\right)$ are the energy of the number states $|n\rangle$ and also describe the energy levels of a harmonic oscillator with frequency ω. The annihilation and creation operators act on the number states with the following relations:

$$\hat{a}\,|n\rangle = \sqrt{n}\,|n-1\rangle\,, \tag{2.18}$$

$$\hat{a}^\dagger\,|n\rangle = \sqrt{n-1}\,|n+1\rangle\,. \tag{2.19}$$

The number n can be interpreted as the number of particles in a state with $\hat{a}$ and $\hat{a}^\dagger$ reducing or increasing that number. From the ground state $|0\rangle$, also called vacuum state, with no particles, the number states $|n\rangle$ can be generated by the repeated application of $\hat{a}^\dagger$:

$$|n\rangle = \frac{(\hat{a}^\dagger)^n}{\sqrt{n!}}\,|0\rangle \tag{2.20}$$

Number states form a complete set with states of different numbers being orthogonal to each other, i.e. $\langle n|m\rangle = \delta_{nm}$. They are a useful description for several applications but have their limits when describing continuous-wave laser light, for which the coherent states are introduced in the next section.

2.1.2 Coherent states

Coherent light emitted by a laser does not have a well-defined number of photons and requires an additional formalism for its description. Several approaches exist for introducing coherent states which were first described in 1963 by [Gla63]. Here I follow [Ger+05] (p. 46) as this method is equivalent to the definition of squeezed states, which are introduced in section 2.2. Coherent states $|\alpha\rangle$ can be described as displaced vacuum states

$$|\alpha\rangle = \hat{D}(\alpha)\,|0\rangle\,, \tag{2.21}$$

where $\hat{D}(\alpha)$ is the displacement operator:

$$\hat{D}(\alpha) = e^{\alpha\hat{a}^\dagger - \alpha^*\hat{a}}. \tag{2.22}$$

Coherent states can also be expressed in terms of number states:

$$|\alpha\rangle = \hat{D}(\alpha)\,|0\rangle \tag{2.23}$$

$$= e^{-\frac{1}{2}|\alpha|^2}\sum_{n=0}^{\infty}\frac{\alpha^n}{\sqrt{n!}}\,|n\rangle\,. \tag{2.24}$$

To calculate the mean photon number of a coherent state, we can find its expectation value, using the number operator $\hat{n} = \hat{a}^\dagger \hat{a}$

$$\bar{n} = \langle \alpha | \hat{n} | \alpha \rangle = |\alpha|^2. \tag{2.25}$$

$|\alpha|$ can therefore be interpreted as the classical amplitude of a laser light field. The photon number fluctuation is given by

$$\Delta n = \sqrt{\langle \hat{n}^2 \rangle - \langle \hat{n} \rangle^2} = \sqrt{\bar{n}} \tag{2.26}$$

which is a typical Poissonian process. Thus, the probability of detecting n photons in the field is given by the distribution

$$P_n = |\langle n | \alpha \rangle|^2 = \frac{|\alpha|^{2n} e^{-|\alpha|^2}}{n!}. \tag{2.27}$$

Both, coherent and ground states, are members of the group of minimum uncertainty states. They are further described in the next section.

2.1.3 Field quadratures

For a single-mode field, the annihilation operator $\hat{a}$ can be expressed as a linear combination of two Hermitian operators $\hat{X}$ and $\hat{Y}$ [Wal+08], p. 16:

$$\hat{a} = \frac{\hat{X} + i\hat{Y}}{2}. \tag{2.28}$$

These operators are called the amplitude quadrature operator $\hat{X}$ and the phase quadrature operator $\hat{Y}$ and are defined as

$$\hat{X} = \hat{a} + \hat{a}^\dagger \tag{2.29}$$

$$\hat{Y} = i(\hat{a}^\dagger - \hat{a}) \tag{2.30}$$

using the annihilation and creation operators introduced in section 2.1.1. They represent the dimensionless amplitudes for the quadrature phases of a single-mode field, oscillating with a 90° phase offset relative to each other. They emerge from the generic quadrature operator

$$\hat{X}(\theta) = \hat{a} e^{-i\theta} + \hat{a}^\dagger e^{i\theta} \tag{2.31}$$

for $\theta = 0$ and $\theta = \frac{\pi}{2}$.

These operators do not commute and are thus limited by the Heisenberg uncertainty principle. Since any two non-commuting observables $\hat{A}$ and $\hat{B}$ cannot be measured simultaneously, they satisfy the commutation relation

$$\Delta^2\hat{A}\Delta^2\hat{B} \geq \frac{1}{4}\left|\langle[\hat{A},\hat{B}]\rangle\right|^2 = 1. \tag{2.32}$$

This shows that the outcome of measurements of these observables is always associated with an uncertainty, which is minimized by certain states. The variance $\Delta^2\hat{A}$ for an arbitrary state Ψ is given by $\Delta^2\hat{A} = \langle\hat{A}^2\rangle - \langle\hat{A}\rangle^2 = \langle\Psi|\hat{A}^2|\Psi\rangle - \langle\Psi|\hat{A}|\Psi\rangle^2$. The commutation relation for $\hat{X}$ and $\hat{Y}$ is

$$[\hat{X},\hat{Y}] = 2i = 4[\hat{q},\hat{p}] \tag{2.33}$$

resulting in the uncertainty relation

$$\Delta^2\hat{X}\Delta^2\hat{Y} \geq 1 \tag{2.34}$$

without making any specific assumptions about the quantum states. To obtain the variance of both quadrature operators for a coherent state $|\alpha\rangle$ and the ground state $|0\rangle$, we calculate

$$\langle\hat{X}^2\rangle = \langle\alpha|\left(\hat{a}+\hat{a}^\dagger\right)^2|\alpha\rangle \tag{2.35}$$
$$= 1 + \alpha^2 + \alpha^{*2} + 2\alpha\alpha^* \tag{2.36}$$
$$\langle\hat{X}\rangle^2 = \left(\langle\alpha|\hat{a}+\hat{a}^\dagger|\alpha\rangle\right)^2 \tag{2.37}$$
$$= \alpha^2 + \alpha^{*2} + 2\alpha\alpha^* \tag{2.38}$$
$$\langle\hat{X}^2\rangle - \langle\hat{X}\rangle^2 = 1 = \Delta^2\hat{X} \tag{2.39}$$

and

$$\langle\hat{Y}^2\rangle = \langle\alpha|\left(i(\hat{a}^\dagger-\hat{a})\right)^2|\alpha\rangle \tag{2.40}$$
$$= 1 - \alpha^2 - \alpha^{*2} + 2\alpha\alpha^* \tag{2.41}$$
$$\langle\hat{Y}\rangle^2 = -\alpha^2 - \alpha^{*2} + 2\alpha\alpha^* \tag{2.42}$$
$$\langle\hat{Y}^2\rangle - \langle\hat{Y}\rangle^2 = 1 = \Delta^2\hat{Y}. \tag{2.43}$$

The same results for $\Delta^2\hat{X}$ and $\Delta^2\hat{Y}$ emerge for the ground state $|0\rangle$ and therefore

$$\Delta^2\hat{X}\Delta^2\hat{Y} = 1 \tag{2.44}$$

is true for both states. Consequently, they possess the smallest possible uncertainty product, a property also shared by squeezed vacuum states. Squeezed vacuum states exhibit reduced and amplified variances in the field quadratures and are introduced in the next section. At this point, I would like to note that there are two different definitions for the minimum uncertainty value. While I primarily follow [Wal+08] in this section, other sources (e.g., [Ger+05]) use the convention $\Delta^2\hat{X}\Delta^2\hat{Y} = \frac{1}{16}$.

2.2 Squeezed states of light

Squeezed states of light are quantum states that exhibit reduced noise in one quadrature at the expense of increased noise in the orthogonal quadrature, while still satisfying Heisenberg's uncertainty principle (2.32). This property makes them a valuable tool for a variety of applications, including this work. In the following section, I introduce the theoretical background for squeezed states, their properties in the presence of optical losses, and their detection using balanced homodyne detection.

2.2.1 Representation and description of squeezed states

Just as vacuum and coherent states, squeezed states of light are part of the minimum uncertainty states for which $\Delta^2\hat{X}\Delta^2\hat{Y} = 1$ holds. They can be generated by applying the squeeze operator $\hat{S}$ to either a ground state or a coherent state, resulting in a squeezed vacuum state or a displaced squeezed state, respectively. $\hat{S}$ is defined as [Bac+19; Wal+08]

$$\hat{S}(\xi) = \exp\left(\frac{1}{2}\xi^*\hat{a}^2 - \frac{1}{2}\xi\hat{a}^{\dagger 2}\right) \tag{2.45}$$

where $\xi = re^{2i\theta}$, with r being the squeeze factor and θ the squeeze angle. To calculate the expectation values and variances of a squeezed state, it is helpful to use the following relations [Bac+19], p. 314:

$$\hat{S}^\dagger(\xi) = \hat{S}^{-1}(\xi) = \hat{S}(-\xi), \tag{2.46}$$

$$\hat{S}^\dagger(\xi)\hat{a}\hat{S}(\xi) = \hat{a}\cosh r - \hat{a}^\dagger e^{-2i\theta}\sinh r, \tag{2.47}$$

$$\hat{S}^\dagger(\xi)\hat{a}^\dagger\hat{S}(\xi) = \hat{a}^\dagger\cosh r - \hat{a}e^{2i\theta}\sinh r. \tag{2.48}$$

Using these, the expectation values $\langle \hat{a} \rangle$ and $\langle \hat{a}^2 \rangle$ of the annihilation operator for a state $|\psi\rangle$ can be expressed as

$$\langle \psi|\hat{a}|\psi\rangle = \langle \psi|\hat{S}^\dagger(\xi)\hat{a}\hat{S}(\xi)|\psi\rangle\,, \tag{2.49}$$

$$\langle \psi|\hat{a}^2|\psi\rangle = \langle \psi|\hat{S}^\dagger(\xi)\hat{a}\hat{S}(\xi)\hat{S}^\dagger(\xi)\hat{a}\hat{S}(\xi)|\psi\rangle\,. \tag{2.50}$$

With these properties, the expectation values $\langle \hat{X}^2 \rangle$, $\langle \hat{X} \rangle^2$ and $\langle \hat{Y}^2 \rangle$, $\langle \hat{Y} \rangle^2$ can be calculated for a vacuum state $|0\rangle$, leading to the variances

$$\Delta^2\hat{X} = \cosh^2 r + \sinh^2 r - 2\sinh r \cosh r \cos 2\theta, \tag{2.51}$$

$$\Delta^2\hat{Y} = \cosh^2 r + \sinh^2 r + 2\sinh r \cosh r \cos 2\theta. \tag{2.52}$$

For a squeezing angle of $\theta = 0$, these reduce to

$$\Delta^2\hat{X} = e^{-2r} \tag{2.53}$$

$$\Delta^2\hat{Y} = e^{2r} \tag{2.54}$$

demonstrating a squeezed vacuum state with the noise reduced in the $\hat{X}$ quadrature, while extra noise is exhibited in the $\hat{Y}$ quadrature. For $\theta = \frac{\pi}{2}$, the squeezing occurs in the $\hat{Y}$ quadrature and the anti-squeezing in the $\hat{X}$ quadrature. The product of both variances equals 1, as indicated in equation 2.44 for minimum uncertainty states.

A graphical description of the states introduced so far is shown in figure 2.1, comparing a vacuum state (left), a coherent state (middle), and a squeezed state (right) with their corresponding uncertainties in the phase space representation.

Squeezed light as described in section 2.4.2 is generated over a certain bandwidth, determined by the cavity parameters. The squeeze factor is influenced by the amount of pump power P relative to the oscillation threshold pump power P_{thr}, above which a bright field would be produced instead of squeezed states. The spectrum for squeezed and anti-squeezed states is given by [Vah+16; Sch18; Pol+92]:

$$S_{\text{sqz,asqz}}(f) = 1 \mp \frac{4\sqrt{\frac{P}{P_{\text{thr}}}}}{\left(1 \pm \sqrt{\frac{P}{P_{\text{thr}}}}\right)^2 + 4\left(\frac{f}{\gamma}\right)^2} \tag{2.55}$$

where P is the pump power, P_{thr} the pump power threshold, f the frequency and γ the cavity linewidth. In the next section, I discuss the influence of optical losses on squeezed states.

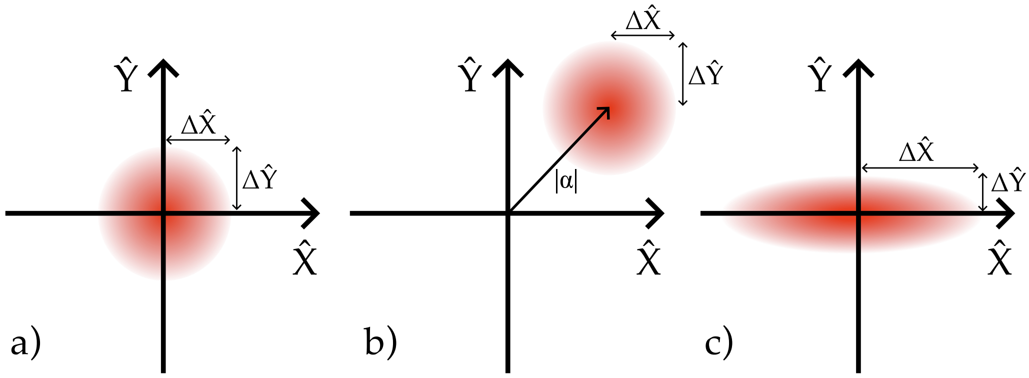

Figure 2.1: Representation of a vacuum state (a)), a displaced vacuum or coherent state (b)) and a squeezed state (c)) with the $\hat{X}$ and $\hat{Y}$ quadratures on the axes of the coordinate system. The standard deviations $\Delta\hat{X}$ and $\Delta\hat{Y}$ are the same for a) and b). In c), $\Delta\hat{Y}$ is smaller, while the variance in the orthogonal quadrature is increased. The amplitude of the coherent state is given by $|\alpha|$.

2.2.2 Losses and decoherence

The theoretical values for squeezed and anti-squeezed states from equation 2.55 do not directly apply to experimental results, as they do not consider any optical losses. In actual experiments, such losses are inevitable due to sources like imperfect optics, absorption, scattering, mode mismatch or the detection efficiency of the photo diodes.

Squeezed states are highly sensitive to optical losses. As described in section 2.4.2, the photons are created in pairs during down-conversion and every missing photon or added vacuum photon destroys the statistics. In contrast to a bright light field, missing photons reduce not only the amplitude but also the maximum achievable squeeze factor. Therefore, losses must be taken into account when working with squeezed light.

Losses can be treated as vacuum noise, that is overlapped with the signal on a beam splitter with reflectivity $R = 1 - \eta$, replacing the photons that are lost. The total detection efficiency is denoted by η, while $1 - \eta$ is lost. The variance of a squeezed state can now be described by [Bac+19], p. 327:

$$\Delta^2\hat{X}_{\theta,\eta} = \eta\Delta^2\hat{X}_\theta + (1-\eta)\Delta^2\hat{X}_{\text{vac}} \tag{2.56}$$

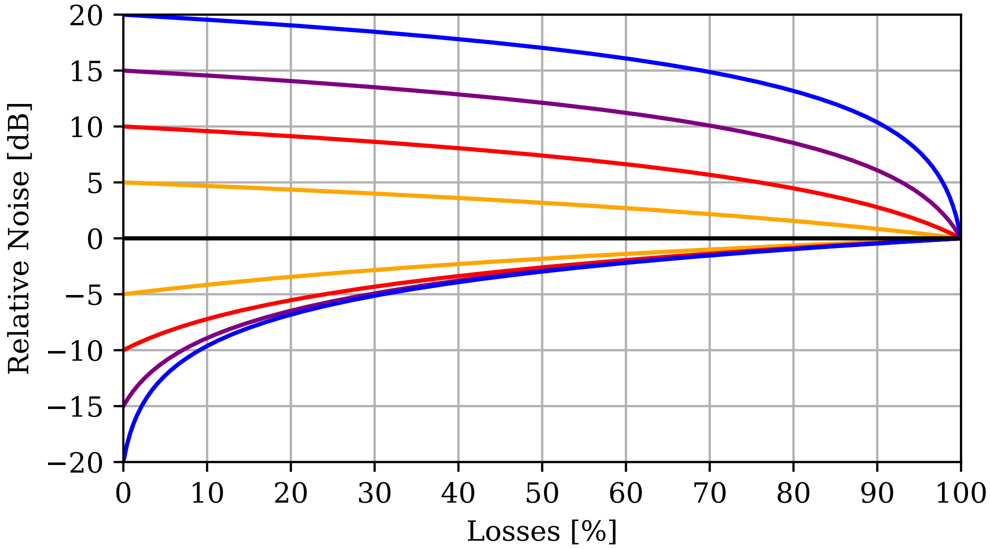

Figure 2.2: Influence of losses on squeezed and anti-squeezed states. Shown here are traces for four different initial values with 20 dB, 15 dB, 10 dB and 5 dB. With 50 % loss a maximum of 3 dB squeezing can be observed and 10 % loss set an upper limit to 10 dB, regardless of the initial squeeze value. On the other hand, 10 dB of anti-squeezing can be measured even with 90 % loss.

where the variance of the ground state is $\Delta^2 \hat{X}_{\mathrm{vac}} = 1$ due to normalization. The equation for the spectrum thus reads

$$S^{\eta}_{\mathrm{sqz,asqz}}(f) = 1 \mp \eta \frac{4\sqrt{\frac{P}{P_{\mathrm{thr}}}}}{\left(1 \pm \sqrt{\frac{P}{P_{\mathrm{thr}}}}\right)^2 + 4\left(\frac{f}{\gamma}\right)^2} \tag{2.57}$$

for squeezed and anti-squeezed states considering losses. From this equation, it becomes apparent, that the influence of losses differs for squeezed and anti-squeezed states, as visualized in figure 2.2. Different initial squeeze and anti-squeeze values are plotted against the amount of loss on the x-axis. Besides the fact, that the squeeze values decrease much faster than the anti-squeeze values, it is evident that a maximum of 10 dB of squeezing can be measured with 10 % loss and a maximum of 3 dB with 50 % loss. In squeezing measurements, the results are typically expressed in decibels (dB), often normalized to the vacuum noise (shot noise). This is related to the squeeze factor r introduced in section 2.2 by dB $= -10\log_{10}(e^{-2r}) = -10\log_{10}(\Delta^2\hat{X}_\theta/\Delta^2\hat{X}_{\text{vac}})$.

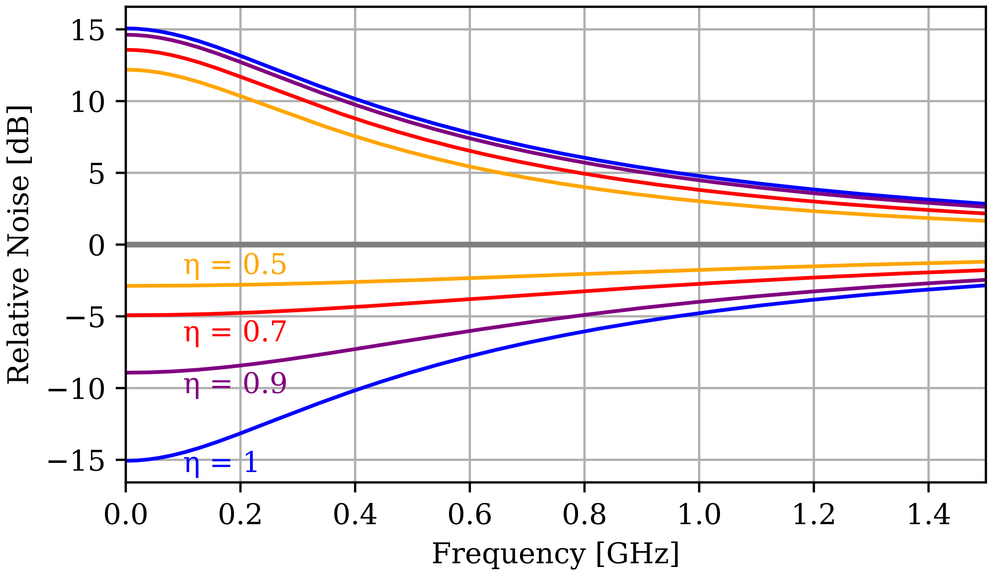

Figure 2.3: Impact of different loss scenarios on the spectrum measurement of a cavity with the parameters $\gamma = 1.75\,\text{GHz}$ and $P/P_{\text{thr}} = 0.49$. While the squeeze values drop massively especially in the lower frequency regions, the anti-squeeze values maintain a comparatively high level.

In figure 2.3, theoretical spectra of squeezing and anti-squeezing measurements with different losses are shown, based on equation 2.57. The parameters are $\gamma = 1.75\,\text{GHz}$ and $P/P_{\text{thr}} = 0.49$, which are realistic values for one of the cavities used in this work. I modeled detection efficiencies between $\eta = 1$(no losses) and $\eta = 0.5$ (50 % loss). While the first case is impossible in a real experimental setup, the case $\eta > 0.95$ has been demonstrated in [Sch+18]. The plot shows, that with the given cavity parameters, the impact of losses is greater at low frequencies.

The calculations and plots in figures 2.2 and 2.3 are a theoretical description of a setup experiencing optical losses. They do not take into account the event of excess phase noise, which is a common problem in fiber-based setups. In the next section, I provide an overview of phase noise and its impact on squeezing measurements.

2.2.3 Phase noise

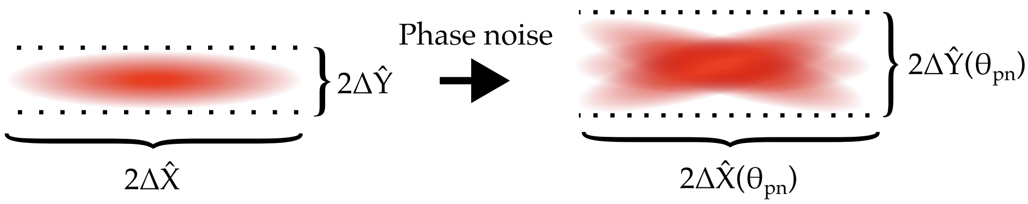

Figure 2.4: Effect of phase noise on a squeeze ellipse. The measurement of the variance of the squeezed quadrature leads to a higher result, as the squeeze factor seems to be smaller with the added noise. The anti-squeezed quadrature remains almost unaffected. It should be noted however, that this is a simplified representation.

Besides optical losses, squeezed states can experience phase noise. Sources of phase noise include, for example, the laser itself or external vibrations coupling to the light. Particularly when working with fibers deployed over some distance outside a stabilized laboratory, seismic, acoustic and mechanical noise can influence the states and the measurement outcomes. Phase noise can be understood as a small rotation of the squeezing ellipse, as visualized in figure 2.4. Since the detector and the associated measurement coordinate system typically do not experience the same phase noise, coherence is lost as the relative phase between the signal and the read-out quadrature changes. This leads to anti-squeezing coupling into the squeezing quadrature and as a result, the squeeze value appears to be lower. The effect is much more pronounced for squeezed states than for anti-squeezed states. Anti-squeezed states already have a larger noise amplitude, so adding extra noise does not have the same impact as adding it to the squeezed quadrature, which has reduced noise. Or, using a metaphor for clarification: shouting in a crowded arena during a soccer game does not have the same effect as shouting in a quiet church, although the voice adds the same amount of noise in both cases.

Consequently, the theoretical description of the measurement spectrum including phase noise has one term for the squeezed and one for the anti-squeezed values. It is given by [Oel+16; Vah+16]

$$S^{\eta}_{\mathrm{sqz}}(\theta_{\mathrm{pn}}) = S^{\eta}_{\mathrm{sqz}}(f)\cos^2(\theta_{\mathrm{pn}}) + S^{\eta}_{\mathrm{asqz}}(f)\sin^2(\theta_{\mathrm{pn}}) \tag{2.58}$$

$$S^{\eta}_{\mathrm{asqz}}(\theta_{\mathrm{pn}}) = S^{\eta}_{\mathrm{asqz}}(f)\cos^2(\theta_{\mathrm{pn}}) + S^{\eta}_{\mathrm{sqz}}(f)\sin^2(\theta_{\mathrm{pn}}) \tag{2.59}$$

where the phase noise is described by a characteristic average value θ_{pn}, assuming a normal distribution and a small standard deviation. This equation shows that parts of the orthogonal quadrature contaminate the outcome of the measured quadrature, where the contribution from anti-squeezing is naturally higher since anti-squeezing contains more noise. In figure 2.5, shows three spectra for a cavity with the same parameters as in figure 2.3 and a detection efficiency of 90 %. Phase noise is shown for $\theta_{\mathrm{pn}} = 0$, $\theta_{\mathrm{pn}} = 60\,\mathrm{mrad}$ and $\theta_{\mathrm{pn}} = 150\,\mathrm{mrad}$. It becomes apparent that phase noise hardly affects the anti-squeeze level at all, while it decreases the squeeze level especially at lower frequencies.

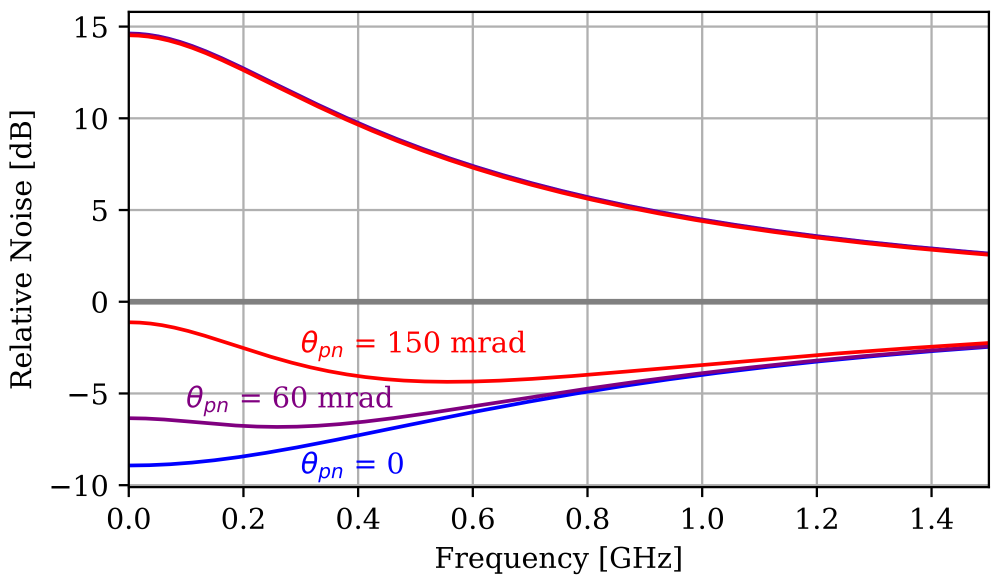

Figure 2.5: Spectra for the cavity parameters specified above and 90 % detection efficiency with different amounts of phase noise. The anti-squeezing experiences no noticeable losses. For the squeezed states, the effect is higher in the lower frequency region.

2.2.4 Detection of squeezed states: Balanced homodyne detection

Balanced homodyne detection is the primary method used for the detection of squeezed light. In this technique, a bright coherent light beam, the local oscillator (LO), is overlapped on a balanced beam splitter with the signal beam and amplifies the signal. "Homodyne" refers to the fact, that the local oscillator and the signal beam are of the same wavelength. Two photo diodes are used, one at each output port of the beam splitter. The detected intensities of both are subtracted from each other. Figure 2.6 shows the schematic setup of a balanced homodyne detector. For the calculations, I mainly follow [Bac+19]. To look at the theoretical description of a balanced

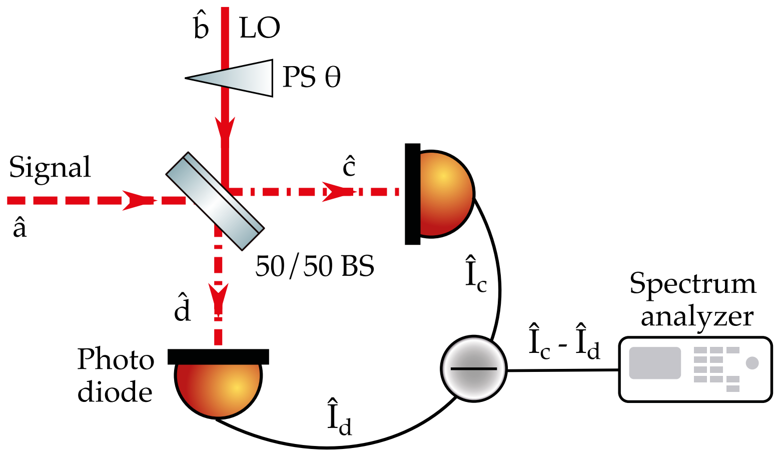

Figure 2.6: The incoming beams from signal and local oscillator are overlapped on a 50/50 beam splitter and each output port is detected by a photo diode. The photo currents are subtracted from each other and can be analyzed for example with a spectrum analyzer.

homodyne detector, it is useful to describe a field operator $\hat{O}$ in terms of its classical part with amplitude $O = \langle \hat{O} \rangle = \alpha_O$ and the quantum noise part $\delta\hat{O}$. The two incoming beams can then be expressed by

$$\hat{a} = \alpha_a + \delta\hat{a} \tag{2.60}$$

$$\hat{b} = \left(\alpha_b + \delta\hat{b}\right) e^{i\theta} \tag{2.61}$$

with the corresponding amplitudes α and the phase relation $e^{i\theta}$ between the two fields. The output of the beam splitter is given with

$$\hat{c} = \frac{1}{\sqrt{2}}(\hat{b}e^{i\theta} + \hat{a}) \tag{2.62}$$

$$\hat{d} = \frac{1}{\sqrt{2}}(\hat{b}e^{i\theta} - \hat{a}), \tag{2.63}$$

including the phase flip of 180° for one of the output beams. The photo currents $\hat{I}_c$ and $\hat{I}_d$ are directly proportional to the amount of photons in the corresponding beams and can therefore be expressed with

$$\hat{I}_c \sim \hat{n}_c = \hat{c}^\dagger\hat{c} = \frac{1}{2}\left(\hat{b}^\dagger\hat{b} + \hat{a}^\dagger\hat{a} + \hat{b}^\dagger e^{-i\theta}\hat{a} + \hat{a}^\dagger\hat{b}e^{i\theta}\right) \tag{2.64}$$

$$\hat{I}_d \sim \hat{n}_d = \hat{d}^\dagger\hat{d} = \frac{1}{2}\left(\hat{b}^\dagger\hat{b} + \hat{a}^\dagger\hat{a} - \hat{b}^\dagger e^{-i\theta}\hat{a} - \hat{a}^\dagger\hat{b}e^{i\theta}\right). \tag{2.65}$$

The difference of the photo currents are given by

$$\hat{I}_c - \hat{I}_d \sim \hat{n}_c - \hat{n}_d \tag{2.66}$$

$$= \hat{b}^\dagger e^{-i\theta}\hat{a} + \hat{a}^\dagger\hat{b}e^{i\theta} \tag{2.67}$$

$$= 2\cos\theta\ \alpha_b\alpha_a + \alpha_b\delta\hat{X}^a_\theta + \alpha_a\delta\hat{X}^b_\theta + \delta\hat{b}^\dagger\delta\hat{a}e^{-i\theta} + \delta\hat{a}^\dagger\delta\hat{b}e^{i\theta}. \tag{2.68}$$

To obtain the last result, we used the fact that $\alpha^* = \alpha$ and equation 2.31 for the quadrature operator. The amplitude of the local oscillator is usually several magnitudes higher than the one from the signal beam, in particular when detecting squeezed vacuum states. We can therefore assume $\alpha_b \gg \alpha_a$ and also consider the noise contributions to be small compared to the amplitude contributions. With that, the result above can be simplified: the first term only contains DC parts that do not influence the noise level and $|\alpha_b\delta\hat{X}^a_\theta| \gg |\alpha_a\delta\hat{X}^b_\theta|, |\delta\hat{b}^\dagger\delta\hat{a}|, |\delta\hat{a}^\dagger\delta\hat{b}|$. This simplification is known as the homodyne approximation and leads to the relation

$$\hat{I}_c - \hat{I}_d \sim \alpha_b\hat{X}^a_\theta. \tag{2.69}$$

With this equation it becomes apparent, that the noise of the signal beam is amplified with the amplitude of the local oscillator, while other terms do not contribute to the result significantly. The read-out angle can be chosen by tuning the angle θ to maximize or minimize the result, e.g. measuring the squeezed or anti-squeezed quadrature. The variance of the subtracted current is given by

$$\Delta^2(\hat{I}_c - \hat{I}_d) \sim \alpha_b^2 \delta^2 \hat{X}_\theta^a \tag{2.70}$$

which gives us a directly proportional relation to the variance of the squeezed vacuum state.

The quality of the mode overlap is described by the fringe visibility given by

$$V = \frac{I_{\max} - I_{\min}}{I_{\max} + I_{\min}}, \tag{2.71}$$

presuming equal power in the input ports. $I_{\min}$ and $I_{\max}$ are then the minimum and maximum intensities while scanning the phase of the local oscillator. To achieve a good detection efficiency, the spatial mode overlap between the local oscillator and the signal beam has to be optimized. This is done using a reference cavity as described in chapter 4.The quantum efficiency η_{PD} of the photo diodes also contributes to the detection efficiency of the homodyne detector, which is given in total by

$$\eta_{\mathrm{hom}} = \eta_{\mathrm{PD}} V^2. \tag{2.72}$$

A value of $V = 1$ would mean, that the detector records the full information of the signal, which can usually not be achieved in experiments.

2.3 Entangled states of light

Squeezed states of light as described in the previous section can serve as a resource for entanglement. By overlapping two squeezed vacuum states on a beam splitter, two-mode squeezing can be generated. The term "two-mode squeezed" is treated differently in literature. In some cases, it is used to describe the two frequency sidebands of a squeezed state that are generated in the nondegenerate parametric down-conversion process [Ger+05] p. 187. In other cases, it describes the two output modes of a beam splitter with two squeezed states at the input ports. Some sources with that definition require a difference in the squeeze factor for the two input squeezed states [Ebe13; Sam12]. For this work "two-mode squeezed states" refers to two single-mode squeezed states, overlapped on a balanced beam splitter. In the next two sections, I give a theoretical description and a measure for the strength of entanglement by introducing the inseparability (Duan) as well as the EPR-Reid criterion.

2.3.1 Two-mode squeezed states

In analogy with the operator for squeezed states, the operator for two-mode squeezed states can be defined, following [Ger+05; Wal+08]:

$$\hat{S}_2(\zeta) = \exp\left(\zeta^* \hat{a}\hat{b} - \zeta \hat{a}^\dagger \hat{b}^\dagger\right) \tag{2.73}$$

with $\zeta = re^{i\theta}$ and the operators for the two modes $\hat{a}$ and $\hat{b}$. It contains pairs of annihilation and creation operators. As I used squeezed vacuum states in this thesis, I concentrate on the interaction of the two-mode squeeze operator with a two-mode vacuum $|0\rangle_a |0\rangle_b = |00\rangle$

$$|\zeta\rangle_2 = \hat{S}_2(\zeta) |00\rangle . \tag{2.74}$$

The two-mode squeeze operator is not a product of two single-mode squeeze operators and the two-mode squeezed vacuum accordingly does not factor into two single-mode squeezed states. Instead, it is a superposition state with strong correlations between the two modes. To reveal the correlations, two modes must be measured and combined in a superposition quadrature. The corresponding operators are given by

$$\hat{X}_{ab} = \frac{1}{\sqrt{2}} \left(\hat{a} + \hat{a}^\dagger + \hat{b} + \hat{b}^\dagger\right) \tag{2.75}$$

$$\hat{Y}_{ab} = \frac{1}{\sqrt{2}i} \left(\hat{a} - \hat{a}^\dagger + \hat{b} - \hat{b}^\dagger\right) . \tag{2.76}$$

They satisfy the commutation relation $[\hat{X}_{ab}, \hat{Y}_{ab}] = \frac{i}{2}$ as well as equation 2.32, with which it becomes apparent, that two-mode vacuum states also belong to the minimum uncertainty states. Similar to the single-mode squeezing operator, we can investigate the expectation values and variances. For that it is helpful to use the transformations

$$\hat{S}_2^\dagger(\zeta)\hat{a}\hat{S}_2(\zeta) = \hat{a} \cosh r - e^{i\theta}\hat{b}^\dagger \sinh r \tag{2.77}$$

$$\hat{S}_2^\dagger(\zeta)\hat{b}\hat{S}_2(\zeta) = \hat{b} \cosh r - e^{i\theta}\hat{a}^\dagger \sinh r. \tag{2.78}$$

We then obtain

$$\langle \hat{X}_{ab} \rangle = 0 = \langle \hat{Y}_{ab} \rangle \tag{2.79}$$

and

$$\Delta^2 \hat{X}_{ab} = \cosh^2 r + \sinh^2 r - 2 \sin r \cosh r \cos\theta \tag{2.80}$$

$$\Delta^2 \hat{Y}_{ab} = \cosh^2 r + \sinh^2 r + 2 \sin r \cosh r \cos\theta. \tag{2.81}$$

For $\theta = 0$ this simplifies to

$$\Delta^2 \hat{X}_{ab} = e^{-2r} \tag{2.82}$$

$$\Delta^2 \hat{Y}_{ab} = e^{2r} \tag{2.83}$$

which is identical to the results of a single-mode squeezed vacuum but analyzed here in terms of the superposition quadrature operators. Squeezing can therefore only be measured by considering the superposition (e.g sum or difference) of both modes via the superimposed quadrature operator. Measuring one of the superimposed modes would lead to a variance $\Delta^2 \hat{X}_a \left|\zeta\right\rangle_2 \geq 1$ equal or greater than the shot noise.

In the next section, I will introduce two criteria to characterize the strength of correlations.

2.3.2 Gaussian entanglement criteria

The correlations described in section 2.3.1 can be quantified regarding their strength. I will provide an overview of two criteria here, the Duan criterion [Dua+00] and the EPR-Reid criterion [Rei89]. The latter is closely related to the famous Gedankenexperiment, formulated by Einstein, Podolsky and Rosen in 1935 [Ein+35]. The three authors raised the question of whether the quantum mechanical description of reality can be considered complete. Their argumentation was based on spatially separated particles with entangled position and momentum properties. By performing a measurement on either one of the particles, the measurement outcome of the other particle can be predicted without disturbing it, due to the nature of entanglement and regardless of which property is measured. The authors argued that if a physical quantity can be predicted with certainty without disturbing the system, it must correspond to an element of physical reality. Since both position and momentum can be assigned such elements of reality, while quantum mechanics does not allow them to possess simultaneous definite values, they concluded that the theory of quantum mechanics is incomplete. Based on that work, different measures for the strength of entanglement were developed in the following decades. Although EPR did not mention hidden variables in their paper explicitly, they were introduced later by other physicists and led to Bell's inequality and Bell test experiments to exclude local hidden variables [Bel64], indicating strong correlations. The Duan and EPR-Reid criteria introduced in the following, provide conditions for inseparability and a quantitative measure for correlations of Gaussian states respectively.

Duan criterion: In 2000, Duan et al proposed a criterion for the inseparability of Gaussian states and a sufficient condition for entanglement of any two-party continuous-variable system [Dua+00]. The criterion is based on the variance of a pair of states, which in total has a lower bound if the states are separable, i.e. can be expressed by the product of the two individual modes. It is expressed in terms of quadrature operators and introduces EPR type operators such as $\hat{X}_A + \hat{X}_B$ and $\hat{Y}_A - \hat{Y}_B$ for which the total variances vanish in the theoretical case of maximal entanglement. For the realistic case of experimentally generated two-mode squeezed states, it decreases with increasing squeeze factor r. For a shot noise normalization equal to unity, the criterion reads

$$\Delta^2\left(|a|\hat{X}_A + \frac{1}{a}\hat{X}_B\right) + \Delta^2\left(|a|\hat{Y}_A - \frac{1}{a}\hat{Y}_B\right) \geq 2\left(a^2 + \frac{1}{a^2}\right) \qquad (2.84)$$

with the two subsystems A and B and an arbitrary nonzero real number a. It can be shown [Ebe13], that $a = \pm 1$ is the optimal parameter for symmetric states, which leads to the simplification

$$\Delta^2\left(\hat{X}_A \pm \hat{X}_B\right) + \Delta^2\left(\hat{Y}_A \mp \hat{Y}_B\right) \geq 4. \qquad (2.85)$$

For any value below four, the two subsystems are inseparable, entangled states. Note, that the condition for symmetric states is a balanced 50/50 beam splitter for the entanglement generation and the same amount of optical loss in the output ports to the homodyne detectors. As this thesis distributes one output to via optical fibers to another laboratory, the latter condition can be assumed to be not fulfilled. However, this merely leads to other values in the criterion while the underlying concept remains unchanged.

EPR-Reid criterion: While the Duan criterion gives a sufficient and necessary condition for inseparability, a condition for EPR entanglement was formulated by Reid in 1989 [Rei89]. It is formulated for the quadrature operators $\hat{X}$ and $\hat{Y}$ and considers the output fields of a nondegenerate parametric amplifier. The author introduces the inferred variance for the amplitude and phase quadratures given by

$$\Delta^2_{\text{inf}}\hat{X}_B = \Delta^2\left(\hat{X}_B - g\hat{X}_A\right) \tag{2.86}$$

$$\Delta^2_{\text{inf}}\hat{Y}_B = \Delta^2\left(\hat{Y}_B - h\hat{Y}_A\right). \tag{2.87}$$

It describes the uncertainty with which the measurement outcome at subsystem B can be predicted after a measurement at subsystem A with the scaling factors g and h. If the condition

$$\Delta^2_{\text{inf}}\hat{X}\Delta^2_{\text{inf}}\hat{Y} \geq 1 \tag{2.88}$$

is violated, the EPR-Reid criterion for entanglement is fulfilled. Starting with A being an amplitude squeezed state and B a phase squeezed state with the squeeze factors r and q, it can be shown [Zan21] that with optimal scaling factors the variance of the correlated quadrature operators reads

$$\Delta^2_{\text{inf}}\hat{X} = \Delta^2\hat{X}^- = e^{-2r} \tag{2.89}$$

$$\Delta^2_{\text{inf}}\hat{Y} = \Delta^2\hat{Y}^+ = e^{-2q} \tag{2.90}$$

where $\hat{X}^- = \hat{X}_A - \hat{X}_B$ and $\hat{Y}^+ = \hat{Y}_A + \hat{Y}_B$. The product of both therefore reads

$$\Delta^2_{\text{inf}}\hat{X}\Delta^2_{\text{inf}}\hat{Y} = e^{-2r}e^{-2q} < 1 \tag{2.91}$$

which is fulfilled for sufficient $r, q > 0$. A two-mode squeezed state as discussed in 2.3.1 can therefore violate the EPR-Reid criterion and show entanglement in measurements. Note that each individual output state of the beam splitter has the variance of a thermal state:

$$\Delta^2\hat{X}_A = \Delta^2\hat{X}_B = \frac{e^{-2q} + e^{+2r}}{2} > 1 \tag{2.92}$$

$$\Delta^2\hat{Y}_A = \Delta^2\hat{Y}_B = \frac{e^{+2q} + e^{-2r}}{2} > 1 \tag{2.93}$$

Only by considering the correlated quadrature operators does the entanglement property becomes apparent. The EPR-Reid criterion differs from a Bell test, as it introduces the scaling factors g and h. The requirement of EPR to "predict with certainty [...] the value of a physical quantity[...]" [Ein+35] is impossible to achieve as no infinitely strong entanglement can exist. Reid allows for errors like optical losses and estimates the uncertainty with the scaling factors and introduces a quantitative criterion for EPR entanglement.

In the previous two sections I introduced the theoretical descriptions for (two-mode) squeezed states. In the next section, I go into nonlinear effects in a medium for the generation of squeezed light.

2.4 Nonlinear optical effects in a cavity

For the results of this thesis, I used two processes occurring in a crystal of nonlinear material, second harmonic generation (SHG) and parametric down-conversion (PDC). The time dependent polarization $P(t)$ of a material when applying an electro-magnetic field $E(t)$ is given by the Taylor series [Boy08]

$$P(t) = \epsilon_0[\chi^{(1)}E(t) + \chi^{(2)}E^2(t) + \chi^{(3)}E^3(t) + ...] \tag{2.94}$$

with the n-th order susceptibility $\chi^{(n)}$ of the material and permittivity ϵ_0 of free space. While it is sufficient to refer to the first term for the description of linear optics, the effects described in this section are based on the term with the second-order susceptibility $P^{(2)} = \epsilon_0\chi^{(2)}E^2(t)$. If nonlinear terms play a relevant role, new frequencies are generated within the crystal. In the second harmonic generation process, the pump light with frequency ω is up-converted to the signal with twice the frequency 2ω. The inverted process is the parametric down-conversion, where the input signal converts to light with half the frequency. Both effects conserve energy and will be described in more detail in the following sections. A schematic diagram of both processes can be found in figure 2.7.

2.4.1 Second harmonic generation

For this work, second harmonic generation was used to convert the 1550 nm light from the main laser into 775 nm light to pump the squeeze lasers. Typically, $\chi^{(1)}$ from equation (2.94) is several orders of magnitude higher than $\chi^{(i)}, i > 1$. In the materials used here, the second order susceptibility becomes large enough ($\approx 10^{-12}\frac{m}{V}$) to have a significant impact on the

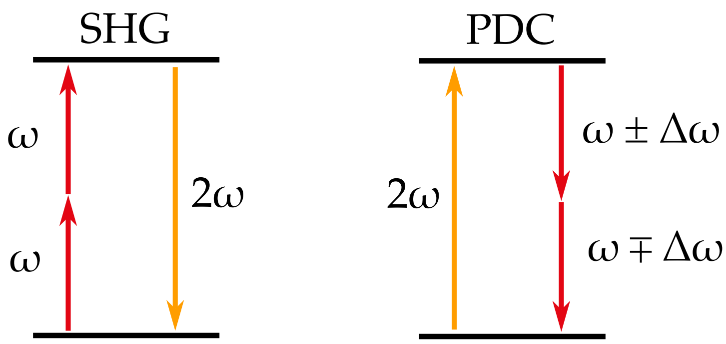

Figure 2.7: Ground level and virtual level of the SHG and PDC processes, happening in a nonlinear material. In the SHG process, two photons with frequency ω are combined to one photon of 2ω and vice versa in the PDC. Without a cavity, the $\Delta\omega$ in the PDC process depends on the phase matching conditions.

incident light field. For the theoretical description ([Boy08] p. 96), a lossless single pass interaction between the nonlinear medium and an electric field is assumed, given by

$$E(z,t) = E_1(z,t) + E_2(z,t). \tag{2.95}$$

E_1 and E_2 correspond to the pump field and the second harmonic field. Each term is expressed by

$$E_j(z,t) = A_j(z)e^{izk_j}e^{-i\omega_j t} + c.c. \tag{2.96}$$

with the propagation constant k_j and the amplitude $A_j(z)$. The nonlinear polarization for the first two terms reads

$$P(z,t) = P_1(z,t) + P_2(z,t) \tag{2.97}$$

with

$$P_j(z,t) = P_j(z)e^{-i\omega_j t} + c.c., \qquad j = 1,2. \tag{2.98}$$

Combining the relations given above, we can obtain for the second order polarization with the second order nonlinearity $d_{\text{eff}} \equiv \frac{1}{2}\chi^{(2)}$ and $\omega_2 = 2\omega_1$:

$$P_2(z,t) = 2\epsilon_0 d_{\text{eff}} E_1^2 e^{-i\omega_2 t}. \tag{2.99}$$

This demonstrates that frequencies at the second harmonic frequency of the fundamental field are generated. As depicted in 2.7, two photons of frequency ω are combined to one photon of frequency 2ω, which is equivalent to a conversion to half of the initial wavelength.

2.4.2 Cavity-enhanced parametric down-conversion

The described process of second harmonic generation can also be performed the other way around to generate two photons of frequency $\omega_+ = \omega_s + \Omega$ and $\omega_- = \omega_i - \Omega$ from one photon with frequency 2ω, where ω_s corresponds to the signal and ω_i to the idler photon. Due to energy conservation $2\omega = \omega_i + \omega_s$. Besides other methods, this effect can be used to generate continuous squeezed states as done in this thesis. For that purpose, we look at the degenerate case in a cavity, where $\Omega = 0$ and $\omega_i = \omega_s = \omega$. For an efficient process, the phases of the pump light and generated squeezed light have to be matched to each other. Experimentally, this is a very important detail and is described in the following.

Phase matching: If the harmonic and fundamental waves have a fixed phase relation and interfere constructively with each other in the nonlinear medium of the crystal, they are considered to have a perfect phase matching. For plane waves, this can be expressed by

$$\Delta k = 2k_1 - k_2 = 0. \tag{2.100}$$

The refractive index of the material determines the speed of light of each wave and due to dispersion, is a decreasing function of wavelength. The expression above for perfect phase matching can be written as

$$\frac{n_2\omega_2}{c_2} = \frac{2n_1\omega_1}{c_1} \tag{2.101}$$

and leads to the condition $n_1 = n_2$ because $2\omega_1 = \omega_2$. This can experimentally be achieved by one of two ways: either using anomalous dispersion effects or materials that show birefringence [Boy08] p. 79. In the latter case, the refractive index is different for the polarization directions of the optical beam. It is a complex task to implement this technique experimentally and involves angle and temperature tuning.

An alternative to these approaches is quasi-phase matching to avoid a rapidly decreasing efficiency of the nonlinear process. In this approach, the crystal is divided into domain segments with inverted polarizations along one crystalline axis. This leads to a changing sign of the effective nonlinearity d_{eff} in every domain and the field amplitude of the generated signal builds up despite the dispersion for the different wavelengths $(n(\omega_2) \neq n(\omega_1))$.

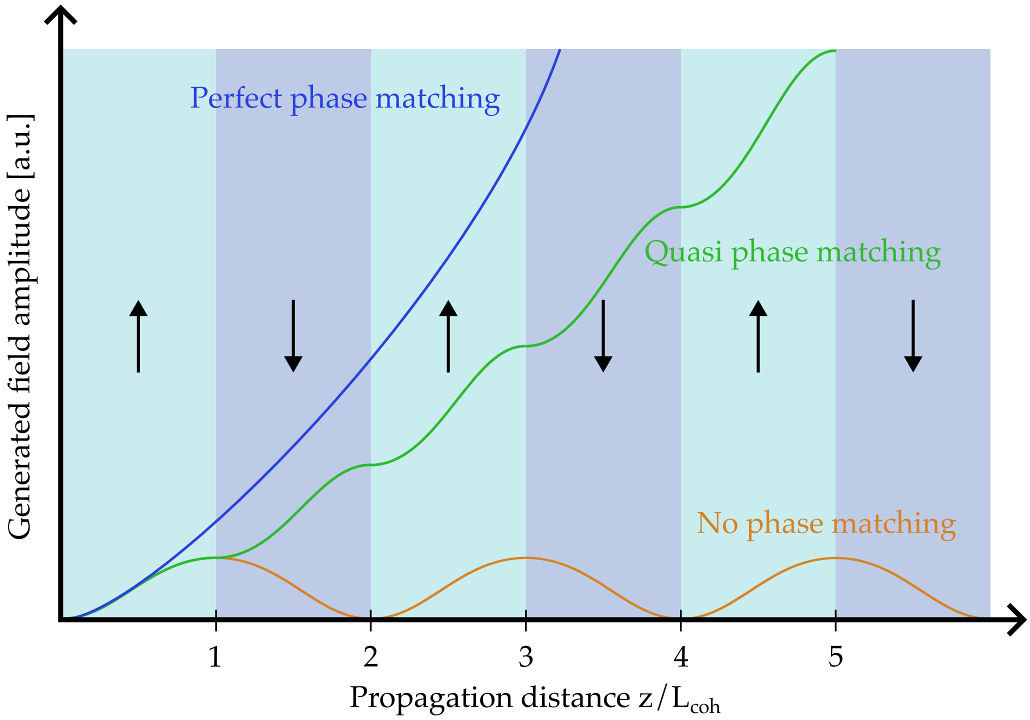

Figure 2.8: Different phase matching types and the resulting amplitude of the generated signal. With no phase matching, the amplitude oscillates due to the velocity difference of the wave fronts and the destructive interference. By changing the sign of the effective nonlinearity d_{eff} (indicated by the arrows and colors) the signal is generated with a 180° phase flip and interferes constructively with the existing fields over the whole length of the crystal.

A qualitative comparison between perfect phase matching, quasi-phase matching and no phase matching is shown in figure 2.8. The domain structure with domain length L_{coh} is indicated by the arrows and colors. With quasi-phase matching an amplitude reduced by a factor of $\frac{2}{\pi}$ compared to the perfect phase matching curve [Fej+92] can be achieved, while no phase matching at all leads to destructive interference and a vanishing generated signal. The optimal length of L_{coh} can be fine tuned by temperature pads as was done in this thesis for both, the second harmonic process and the parametric down-conversion for the generation of squeezed light.

When driving a resonant cavity with a coherent light field, the process of parametric down-conversion can either lead to a bright output field or to parametric amplification, depending on the pump threshold and pump power. The pump threshold for a linear cavity with the reflectivities $R_1 = R_2 \equiv R$ and $(1 - R \ll 1)$ can be expressed as [Boy08] p. 111:

$$e^{2gL} = 2(1 - R) \tag{2.102}$$

with the cavity length L and the gain factor $g \sim d_{\text{eff}} A_p$ where A_p is the amplitude of the pump light. Assuming a single pass gain with $2gL \ll 1$, it can be simplified to

$$gL = 1 - R. \tag{2.103}$$

This holds in the case of perfect phase matching $\Delta k = 0$ for the wave vectors of the fundamental and harmonic light fields.

2.5 Quantum Key Distribution

The aim of Quantum Key Distribution (QKD) is the implementation of a secure key exchange between two parties, Alice and Bob. Any information about the key leaked to an unauthorized third party (Eve) will be detected. In contrast to classical encryption methods, which rely on mathematical complexity, QKD leverages properties of quantum mechanics to achieve a maximum level of security. Theoretically, neither infinite computational power nor time can lead to knowledge about the key or the encrypted message. In this section, I first introduce the earliest QKD protocol, proposed by Bennett and Brassard in 1984 [Ben+14], called BB84. They used polarization entangled single photons and with that choice, discrete-variable (DV) QKD. Second, I briefly explain the protocol known as Ekert91 [Eke91], developed by A. Ekert in 1991. He used spin particles emitted by a sender station between Alice and Bob and applies Bell's theorem to test for eavesdroppers.

BB84

The BB84 protocol is a prepare-and-measure protocol, where Alice prepares photons and sends them to Bob who performs measurements on them. Alice and Bob both use quantum random number generators (QRNGs), Alice for deciding in which basis and direction her photons are polarized and Bob for deciding which basis he wants to use for the measurements of the photons. After a sufficient number of photons have been sent from Alice to Bob, they communicate via a public channel about the bases they used and discard all results for which they used different ones. Inherently, a data loss of 50 % occurs simply due to the protocol. From each measurement performed with consistent bases, one bit for the secret key can be generated. Alice and Bob agree beforehand on which result corresponds to a 1 and which to a 0. In table 2.1, I show an example illustrating the protocol. From the measurements with the correct bases, a few bits are publicly shared to confirm the correctness and increase the security. These bits can no

Alice random bits	0	1	1	0	1	1	0	0	1	1
Random sending bases	D	R	D	R	R	R	R	R	D	D
Photons Alice sends	/	$\vert$	$\backslash$	–	$\vert$	$\vert$	–	–	$\backslash$	$\backslash$
Random receiving bases	R	D	D	R	R	D	D	R	D	D
Bits as received by Bob	1		1		1	0	0	0		1
Bobs reported bases	R		D		R	D	D	R		D
Alice compares her bases			OK		OK			OK		OK
Common bits			1		1			0		1
Randomly shared bits					1					
Alice conforms them					OK					
Remaining secret bits			1					0		1

Table 2.1: Example for a BB84 protocol. In the upper section, the preparation at Alice' station and measurement at Bob's station is shown. Alice randomly choose in which basis her photons are, either diagonal (D) or rectilinear (R) and obtains one bit per photon. In this example, / and - lead to a binary 0 while \and |give a binary 1. Bob measures in a random basis. If he choose the same as Alice (e.g. column 3), he obtains the correct result and one bit, unless the photon is lost (column 4, 9). If the bases do not match, the photon can either be absorbed (column 2) or be transmitted, leading to a wrong result (column 1). The middle section shows post processing steps, which are performed after the measurements. Bob and Alice compare their bases and all measurement results with different bases are discarded, leaving them with the common bits that can be used further (column 3, 5, 8, 10). From these, a few are shared publicly to make sure that the protocol worked (column 5). Those bits cannot be used anymore for the generation of a secret key. The lower section shows the remaining secret bits. Source: [Ben+14]

longer be used for the secret key. Additionally, the transmission channel suffers from losses, which lead to missing photons at Bob's station. Overall, these effects lead to a limited data rate. The security of the BB84 protocol relies on the quantum mechanical effects of true randomness (Alice and Bob choosing their bases) and the no-cloning theorem [Woo+82], which makes it impossible for an eavesdropper to intercept a photon and sends an identical copy to Bob to remain undetected. Entanglement however, is not part of this protocol but will be introduced in the next section with the Ekert91 protocol.

Ekert91

The protocol proposed by A. Ekert in 1991 is the first entanglement-based discrete-variables QKD protocol based on spin particles and can be understood as an extension of the ideas from Bennett and Brassard. In his setup, a source that emits pairs of spin-1/2 particles is located between Alice and Bob. The particles 1 and 2 belonging to a pair are entangled, i. e. show correlated or anti-correlated measurement results, depending on the orientation of the measurement devices. Unlike the BB84 protocol, Alice and Bob both perform measurements, each on one particle of a pair. The orientation of the measurement devices is chosen randomly and shared via a public channel afterwards. Other than in the previously presented protocol, also the results from the measurements with different detector orientations can be used. With Bell's inequality, it is possible to get an upper limit of the particles intercepted or manipulated and to check whether an eavesdropper was present or not. The results from measurements with the same orientation can be further processed to generate a secret key. Only the measurements in which Alice or Bob did not receive a particle at all have to be discarded. It becomes immediately clear, that the data rate for a secret key is usually higher with this protocol.

2.6 Feedback control theory

The development of control loops was an essential part of this work. Besides the feedback control loops for optical cavities, which are a standard tool in our group, I had to compensate a high phase noise level in the remote laboratory of Bob and synchronize the read-out quadratures of both measurement stations.

System description

Before introducing the control elements of a system, it is useful to describe the system and its dynamics itself. A comprehensible guide is given in [Bec05] and [Fra+22], which I mainly follow in this section.

In the time domain, linear dynamic systems can be described by their differential equations

$$\dot{\vec{x}} = \vec{F}\vec{x} + \vec{G}\vec{u} \tag{2.104}$$

$$\vec{y} = \vec{H}\vec{x} + \vec{J}\vec{u} \tag{2.105}$$

where $\vec{x}$ is the state of the system and contains n elements, $\vec{u}$ is the input vector to the system, containing m elements, $\vec{F}$ is the system matrix and $\vec{G}$ the input matrix. $\vec{y}$ is the output vector with the output matrix $\vec{H}$ and direct feed of disturbances $\vec{J}$, which is considered to be a scalar for most use cases. In complex systems, the matrices are usually unknown and have to be determined by the systems response to a known input signal like a step function. This leads us to the transfer functions, which can be obtained by the Laplace transformation:

$$\mathcal{L}\left(\dot{f}(t)\right) = sF(s) \tag{2.106}$$

for zero initial conditions and with the complex frequency variable $s = \sigma + i\omega$. The transfer function $G(s)$ of a linear system can therefore be calculated if the differential equations are known. As a simple example, the first-order system of a low-pass

$$\dot{y}(t) = -\omega_0 y(t) + \omega_0 u(t) \tag{2.107}$$

would turn into

$$sY(s) = \omega_0[-Y(s) + U(s)] \tag{2.108}$$

which leads to the transfer function

$$G(s) = \frac{Y(s)}{U(s)} = \frac{1}{1 + s/\omega_0}. \tag{2.109}$$

The transfer function $G(s)$ is the ratio of the transformed output to transformed input of a system, dependent of the frequency and therefore also called frequency response. In the example above, $\omega_0 = 2\pi f_0$ with the corner frequency f_0 of the low-pass. Analyzing this system with $s = i\omega$, we obtain

$$|G(i\omega)| = \frac{1}{\sqrt{1 + \omega^2/\omega_0^2}} \tag{2.110}$$

for the magnitude and

$$\arg G(i\omega) = -\tan^{-1}\frac{\omega}{\omega_0} \tag{2.111}$$

for the phase, which can be used to generate a Bode plot. With a given transfer function, the output $Y(s)$ can be expressed by

$$Y(s) = G(s)U(s), \tag{2.112}$$

the product of the transformed input $U(s)$ with the systems response $G(s)$.

It is helpful for the understanding of feedback loops to depict them with block diagrams. In figure 2.9, I show a block diagram for a system with transfer function $G(s)$, input u and output y, a sensor with $H(s)$ and a control element with $K(s)$. I also introduce here the reference value r and error e. Since the output is fed back to the input, such a control loop is called feedback control system or closed-loop control system. The error signal is the difference between the reference value r and the system output measured and processed by the sensor: $e(t) = r(t) - y(t)$. For the closed-loop system in 2.9 the output is given by

$$Y(s) = \frac{K(s)G(s)}{1 + K(s)G(s)}R(s) = \frac{L(s)}{1 + L(s)}R(s) \tag{2.113}$$

when assuming $H(s) = 1$ and the open loop gain $L(s) = K(s)G(s)$. This notion as block diagrams will become very useful in the next subsections, where the requirements for a stable system and options for controllers are analyzed.

Stability

The aim of a feedback control loop is the achievement of a better overall performance than the uncontrolled system. In our applications, this can be the suppression of noise or keeping a cavity on resonance, i.e. having a

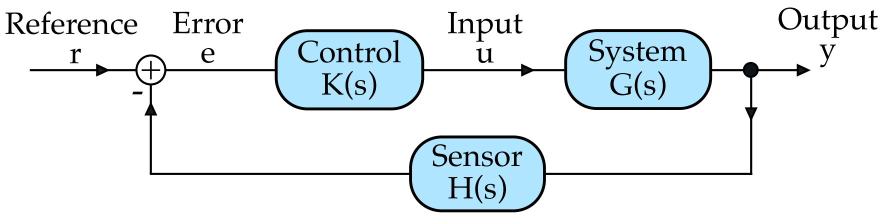

Figure 2.9: Block diagram of a feedback system with one controller, one sensor, reference r, error e, input u and output y.

system stabilized to a certain set point. A system is considered unstable if the control loop leads to oscillations, actuator or amplifier saturation. To analyze the stability and performance of a system, I follow [Abr+00]. A very common way to formulate stability and robustness is given by Bode plots. In figure 2.10, I show a Bode plot for a stable system, plotting the frequency response of the open loop gain $L(i\omega)$.

Typically, two plots are shown: A log-log plot of $|L(i\omega)|$ versus the frequency and the phase of the frequency response $\phi(L(i\omega))$ on a linear scale. The point where $|L(i\omega)| = 1$ (which is the zero crossing due to the log scale) is called unity gain and marks the bandwidth of the feedback control. The terms of gain and phase margin can now be defined as follows: The gain margin in dB is $g_m = -20\log_{10}|L(i\omega_1)|$ with $\omega_1 = 2\pi f_1$ and f_1 marks the frequency at which $\phi = -180°$. The phase margin in degrees is $\phi_m = 180 + \phi(f_0)$, with f_0 being the frequency at which $|L(i\omega)| = 1$.

A system is stable if the phase lag $\phi(L) > -180°$ at frequencies where $|L(i\omega)| = 1$, i.e. the gain margin must be positive $g_m > 0$. In general, higher margins lead to a more robust system, at the expense of performance. A high phase margin, for example, leads to a good response but may limit the maximum achievable gain at lower frequencies. The task for the designer of a feedback control is to find the optimal frequency-dependent gain for noise suppression and stabilization, without creating too much phase lag, which leads to an unstable system. In the next subsection, the PID controller is introduced, a very well tuneable tool for feedback control.

PID controller

Controller types can range from simple passive frequency filters to very complex tools. The most common type of controller is the PID controller.

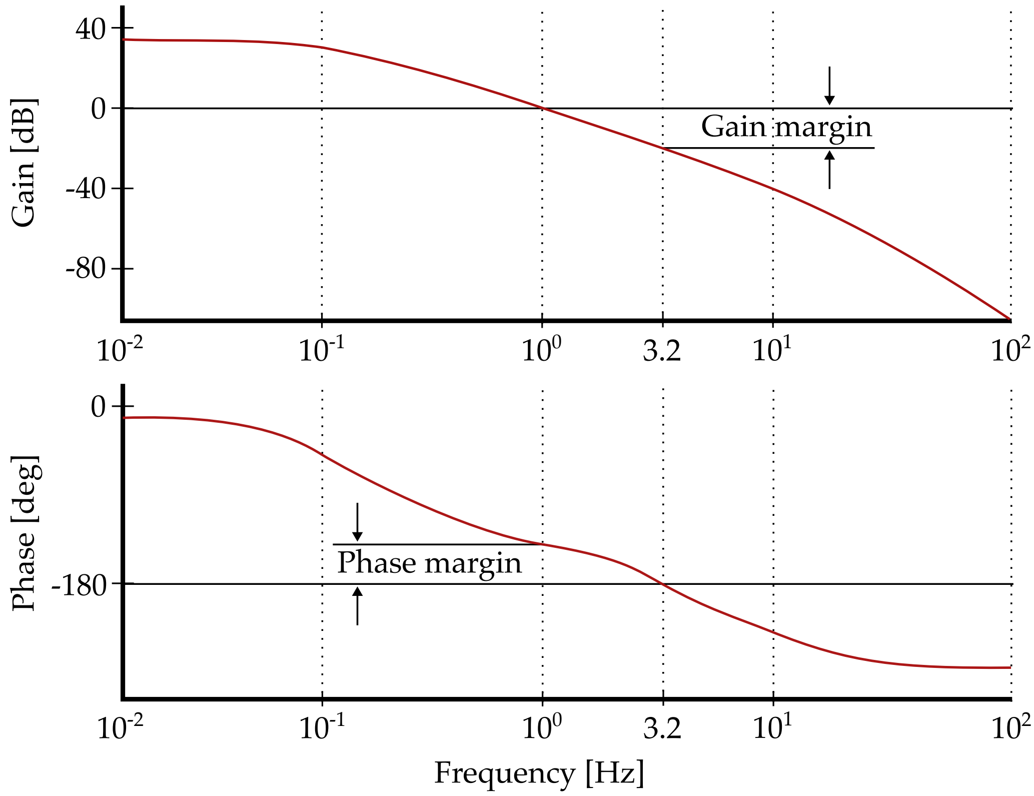

Figure 2.10: Example of a Bode plot with unity gain of 1 Hz and the -180° phase crossing at 3.2 Hz.

It has three parallel control paths: a proportional gain (P), an integral filter (I) and a differential filter (D). The general ideal transfer function for a PID controller is

$$G_{PID} = \frac{\alpha}{s} + \beta + \gamma s, \tag{2.114}$$

where β, α, and γ denote the proportional, integral, and derivative gains of the PID controller, respectively. Since the frequency range of any filter element is finite in a real-world application, the transfer function must be adapted to the filter frequencies, resulting in

$$G_{PID} = \frac{\alpha}{s + 2\pi f_1} + \beta + \gamma \frac{s + 2\pi f_2}{s + 2\pi f_3} \tag{2.115}$$

with the cut-off frequencies of the integrator f_1 and two cut-off frequencies of the derivative f_2 and f_3. It is very flexible in its applications as the three parameters α, β and γ can be easily tuned as well as the corner frequencies of the integrator and differential filter. Therefore, a huge variety of transfer functions can be built and tuned precisely to the system's needs. In my setup, I used only the integral filter of the PID controller.

Loop design

For some complex applications with a wide frequency range and the need for a large actuator range, it can be necessary to use multiple controllers and actuators. They can be arranged in parallel, cascaded or in series, it is possible to build low frequency gain boosts [Abr+00] and nested designs. In this work, a cascaded design of two (see chapter 7) or three (see chapter 6) controllers with corresponding actuators was chosen, arranged from fast to slow. The error signal for the slower controllers was therefore filtered and identical to the output of the preceding controller. This lead to an overall robustness of the system as the actuators hardly interfered with each other in their frequency ranges and a high gain in the low frequencies.

2.7 Fiber theory

The evolution of glass fibers as waveguides for optical purposes is strongly correlated with the development of the first lasers. In the 1960s the first experimental implementations of optical fibers were made [Kao+66] and were transitioned to mass production in 1970 with the founding of the company Corning Inc. Fibers quickly evolved to popular instruments among the telecommunication companies worldwide. In 1987, the company Heraeus lowered the losses in the fibers even further by using high-purity silica material, made possible by a new production method [Kan21]. Today, optical fibers are the heart of worldwide communications and connect small towns and continents with each other.

In this chapter, the basic working principle of optical fibers is presented, as well as the properties of the fibers used in the experiment.

Solid-core and hollow-core fibers: The standard optical fibers consist of a solid core, surrounded by a cladding with a smaller refractive index, so that $n_{\text{core}} > n_{\text{cladding}}$. In modern fibers, the difference in the refractive indices can be around 1 %. The light is confined within the core by total internal reflection, which occurs if light hits the boundary between a denser medium and a less dense medium at an angle less than the critical angle θ_c. According to Snell's law, the relation between the angles and the refractive indices can be described by

$$n_1 \sin\theta_1 = n_2 \sin\theta_2 \tag{2.116}$$

from which the critical angle θ_c can be derived depending on the refractive indices:

$$\theta_c = \arcsin\left(\frac{n_1}{n_2}\right). \tag{2.117}$$

Core and cladding are silica-based. The difference in the refractive indices is realized by doping either one or both with different elements. While it was possible to reduce losses by two orders of magnitude within ten years at 1550 nm, the progress has almost stopped during the last 40 years. Fundamental boundaries due to absorption, scattering and manufacturing imperfections are reached and limit the minimal losses per kilometer to $\sim$ 0.154 dB or more at wavelength other than 1550 nm.

For that reason, a different approach has evolved over the past 27 years: in 1999, the first transmission of light through a new fiber with an air-filled core was reported by [Cre+99]. Since then, hollow-core fibers have shown not only promising results for new wavelengths, but also revealed lower losses at established wavelengths like 1550 nm [Num+23] than solid-core fibers. Two different operation principles exist for hollow-core fibers: on one hand, the Photonic Band Gap Fibers (PBGF) and on the other, the more recent development of Anti-Resonant Fibers (ARF). While the first uses band gaps in the cladding material where no photonic state is allowed and the light is therefore guided in the core material, ARFs work with structural patterns of glass membranes inside the fibers. They are resonant and therefore effectively transparent for all wavelengths with

$$\lambda_m = \frac{2t}{m}\sqrt{n^2 - 1} \tag{2.118}$$

with thickness t of the membranes, the refractive index n and $m = 1, 2, 3, ...$ [Num+23]. However, they are anti-resonant for wavelengths in between and the light can be guided inside the structural patterns of the membranes with very low losses. The demand for ultra low losses at various wavelengths is high and a lot of research has been done over the past years, bringing

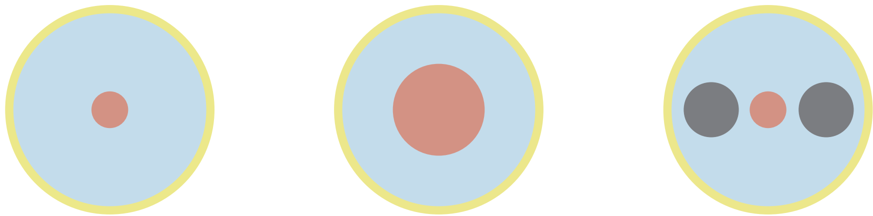

Figure 2.11: Different types of solid-core optical fibers. Red is the fiber core, blue the cladding and yellow a coating for protection. Left is a single mode non-pm fiber, in the middle a multi mode non-pm fiber and on the right a single mode pm fiber.

hollow-core fibers into real-world applications. However, the manufacturing process is more complicated, and handling or splicing the fibers is not easy. Therefore, I concentrate on solid-core fibers for the following sections.

Properties of solid-core optical fibers: In general, optical fibers are either single-mode or multi-mode, with the respective ability to support either one or multiple optical modes. Both are available as polarization-maintaining (PM fiber) or non-polarization maintaining (non-PM fiber). They either maintain the input polarization (if it is well defined) or not, which leads to a random polarization at the output due to drifts within the core material. In figure 2.11, a schematic of the different fiber types can be seen.

The last and perhaps most important property of a fiber is the optical loss per kilometer. The losses are dependent on the wavelength and therefore the choice of the operating wavelength already predetermined the range of losses. The wavelength-dependent losses are shown in figure 2.12 for silica-based fibers.

For our experiment, low losses in the fiber channel are a crucial requirement, since the squeezed states sent through the fiber are very sensitive to optical losses (see section 2.2.2). The lowest losses in silica fibers are achieved at 1550 nm, which is why we chose that wavelength. This offers two additional advantages. First, our scheme could be used by accessing the existing telecommunication network, whose fibers and wavelengths were chosen for the same reasons. Second, 1550 nm is a very common wavelength for research and applications. Equipment is widely available, and standard optics such as mirrors or lenses do not require custom-made products. We

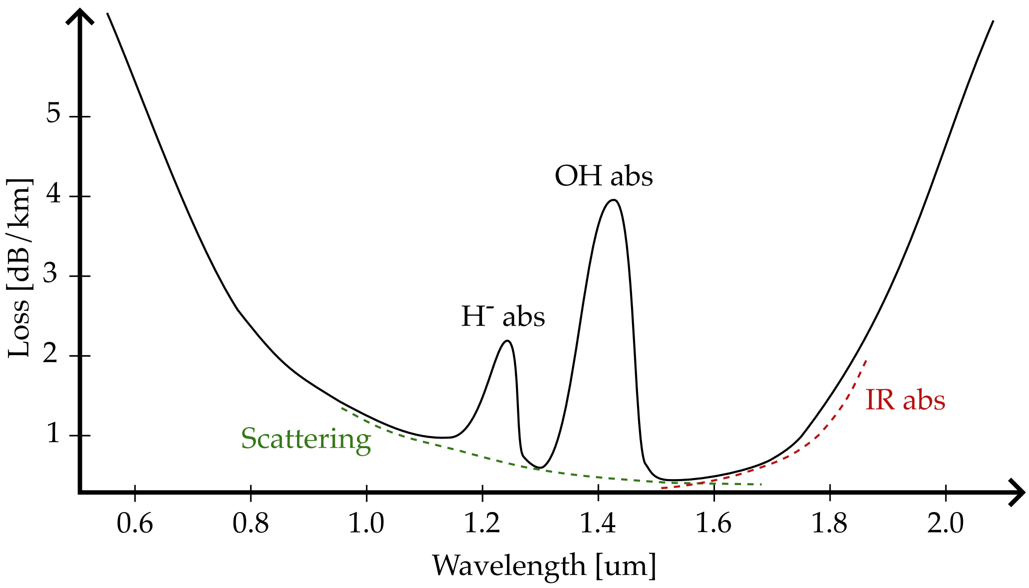

Figure 2.12: Model of losses in a silica-based single mode fiber at different wavelength and the fundamental limitations. The lower frequencies are limited by scattering effects, while the upper suffer from IR absorption. In the middle of the spectrum are two absorption peaks from OH and H^- groups. Source: [Har+00]

also decided to use single-mode and non-PM fibers for cost reasons. PM fibers are more complicated to produce and therefore several orders of magnitude more expensive than non-PM fibers. Even though a stable polarization provided directly by the fibers would have been a desirable feature in our setup, the cost of two kilometers of PM fiber was not justifiable. The polarization tuning and stabilization were realized using passive control elements (see section 4). The fibers we used are two SMF-28 ultra low loss fibers for 1550 nm which exhibit losses below 0.2 dB/km. They can be seen in section 4, figure 4.6.

CHAPTER 3

Experimental methods

In this chapter, I present important methods and techniques I used for my work. The experimental generation of squeezed and two-mode squeezed states as well as details about the quantum noise lock are described here. In the last section I present the QKD protocol used for entanglement-based CV-QKD.

3.1 Generation of squeezed states

Squeezed vacuum states of light can be generated in various ways, including four-wave-mixing in atomic vapor [Slu+85], a fiber-based approach using the third-order Kerr effect [And+16] and down-conversion in a nonlinear crystal [Wu+86]. The squeezed states used in this thesis are generated using cavity-enhanced parametric down-conversion as described in section 2.4.2. The squeeze lasers in my experiment are monolithic cavities, i.e. the coatings of the cavity are directly on the crystal itself. This is in contrast to hemilithic cavities as used for example in [Sch+18], where the cavity is defined by a crystal and an end mirror, separated by an air gap. The design of the squeeze lasers and entanglement source is described in the following sections.

3.1.1 Monolithic squeeze lasers with GHz bandwidth

For a QKD link, a high bandwidth is desirable to achieve a high resulting secret key rate. For this purpose, we used doubly resonant, monolithic squeeze lasers made out of periodically poled KTP (PPKTP) crystals. The design was optimized by Benedict Tohermes [Toh25], developing the work described in [Ast+13]. Monolithic cavities have the coatings applied directly to the end faces of the crystals, whereby the cavity length is defined by the length of the crystal. The decision to use them follows directly from the inversely proportional relation between the cavity length L and the linewidth of a cavity. The shorter the cavity, the higher the linewidth and the resulting bandwidth of the squeezed states. Mathematically, for the cavity linewidth $\Delta\nu$, the free spectral range (FSR) ν_{FSR}, the finesse F and the cavity length L, the following relations are given:

$$\Delta\nu = \frac{\nu_{FSR}}{F} \tag{3.1}$$

$$\nu_{FSR} = \frac{c}{2L} \tag{3.2}$$

and

$$F = \frac{\pi\sqrt[4]{R_1 R_2}}{1-\sqrt{R_1 R_2}}. \tag{3.3}$$

This can be summarized by

$$\Delta\nu = \frac{\nu_{FSR}}{F} \sim \frac{1-\sqrt{R_1 R_2}}{L}. \tag{3.4}$$

From this, the property of double resonance can also be motivated: Besides the cavity length, also the reflectivities of the mirror coatings have an influence on the linewidth. The lower the reflectivities, the lower the finesse and the higher the linewidth. However, lower reflectivities also introduce more loss per roundtrip and thus lead to an increasing pump threshold. Especially when operating two squeeze lasers at the same time, the requirements for the output power of the SHG become very demanding. This can be overcome by using a double resonant design with a cavity not only for the fundamental wavelength of 1550 nm but also for 775 nm, leading to an internal power build-up of the pump wavelength. Combining all considerations led to the cavity design shown in figure 3.1.

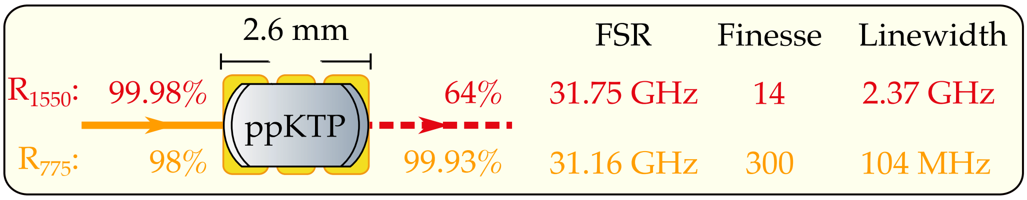

Figure 3.1: Dimensions and designed properties of the monolithic crystals that were used for the GHz-bandwidth squeezed light generation.

The reflectivities of the coated end faces were 99.98 % and 64 % for 1550 nm and 98 % and 99.93 % for 775 nm. As depicted, the crystals had curved end faces with the radii of curvature being $\mathrm{RoC}_1 = \mathrm{RoC}_2 = 12\,\mathrm{mm}$.

The crystal is placed on three temperature pads on a PCB board with one peltier element below each pad. The outer temperature zones are for the fine tuning of the cavity length for the resonance condition and the middle one for the phase matching temperature. While this concept was originally proposed for a much larger crystal, it revealed problems in our setup. The crystal was too short to form three distinct temperature zones and the outer temperature zones were too close to the beam focus in the middle of the crystal and therefore also impacted the phase matching when tuning the length. The two parameters cavity length and phase matching temperature could not be adjusted independently of each other, which led to squeeze factors lower than possible in general and a higher pump power to compensate for that. Experimentally, only the two outer temperature zones were used to drive the cavity to the resonance peak.

3.1.2 Generation of two-mode squeezed states

For the implementation of the QKD protocol described in section 3.3, the generation of two-mode squeezed states is required. This is done by overlapping two single-mode squeezed vacuum states on a 50/50 beam splitter. I stabilized them at a 90° angle to each other, using a control loop implemented by Benedict Tohermes. In figure 3.2 the conceptual process is shown. Two identical single-mode squeezed states are the two inputs of a balanced beam splitter. According to the beam splitter matrix, one output experiences a phase flip of 180°. The symmetry of the resulting entangled states is marked with the colored x and o.

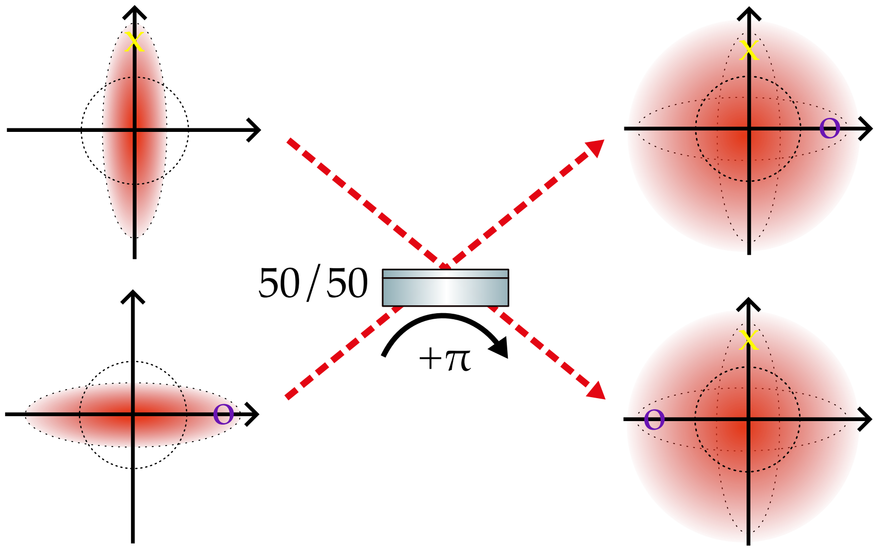

Figure 3.2: Input and output of the entanglement beam splitter. Two single-mode squeezed states are combined to two entangled states. The effect of the phase flip caused by the beam splitter is indicated with the yellow x and purple o.

To get spherically symmetric output states with a 90° angle between the two initial squeezed states, a feedback loop is used to stabilize this angle and counteract any occurring drifts. The schematic setup is shown in figure 3.3. The basic idea involves the 775 nm pump light that gets transmitted through the squeezing cavities and has a fixed phase relation to the corresponding squeezed light. By measuring the 775 nm light power leaving the cavities and one output of the entanglement beam splitter and combining those information, an error signal could be generated. Since the calculations had to be done in real time, a micro-controller (Arduino) was used to process the inputs from the photodiodes. A piezo mounted mirror in front of one of the squeeze lasers acted on the phase of the pump light to adjust the relative phase between the two squeezed states. The details of this locking scheme can be found in [Toh25].

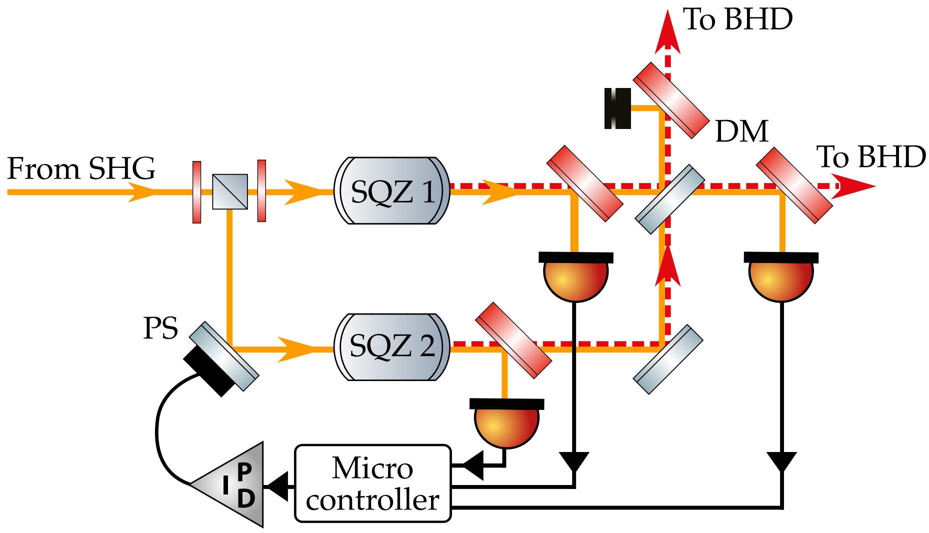

Figure 3.3: Design of the control loop for the relative phase between the two squeezed vacuum states. The design of the cavities allows for 775 nm light to pass through the crystal. This is used to generate an error signal, which steers the phase shifter in front of one of the squeeze lasers.

3.2 Optical phase control: The quantum noise lock

In laser optics experiments, it is essential to build feedback control loops as described in section 2.6 for stabilization purposes. Examples include phase locks to synchronize two phases or a cavity lock to stabilize the length of a cavity, as can be done by a Pound-Drever-Hall stabilization [Bla01]. In this section, I present the quantum noise lock, also called dither lock, which I used to stabilize the phases of the light traveling through our fiber link.
The quantum noise lock is an extremum-seeking control scheme, based on a signal which has well defined minima and maxima, in the present case squeezing and anti-squeezing. The aim is the stabilization of the read-out quadrature to either one of the extrema. The theoretical description follows mainly [McK+05] from McKenzie et al., who proposed it for squeezed light in 2005.

The basic idea is using a perturbation of the system to obtain knowledge about the gradient of the signal and drive the output to an extremum. For

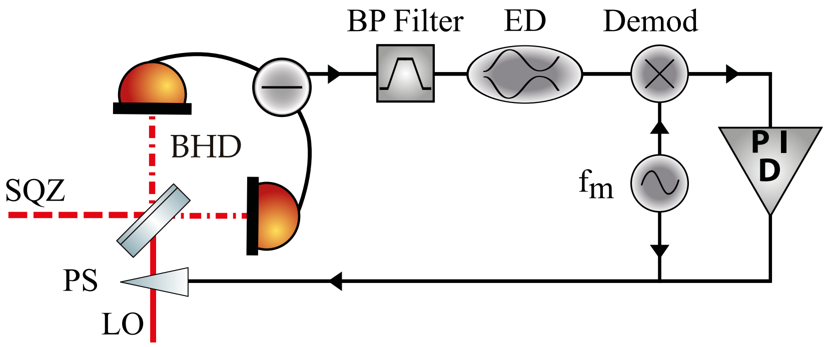

Figure 3.4: Schematic illustration of a quantum noise lock. A modulation frequency f_m is imprinted on the light with a phase shifter (PS). The modulated light gets band pass filtered (BP filter), is processed by an envelope detector (ED) and followed by a demodulation stage where the signal gets demodulated with f_m. The resulting error signal is guided to a PID controller for the control loop.

that, an extra frequency modulation, f_m, is imprinted on the light. This is realized by using a frequency generator driving any element acting on the phase of a light beam, for example a piezo mirror or an electro-optical modulator (EOM). The modulated light is detected by a homodyne detector. The AC signal gets band-pass filtered and is directed to an envelope detector (see figure 3.4 for the schematics). Mathematically, we can describe this in the following: the measured noise variance at an angle θ behind the band-pass filter is given by (see equation (2.56))

$$\Delta^2\hat{X}(\theta) = \eta\left(\Delta^2\hat{X}\,\cos^2(\theta) + \Delta^2\hat{Y}\,\sin^2(\theta)\right)\delta\omega \tag{3.5}$$

containing the detection efficiency η, the contributions of both quadrature operators and the bandwidth limit introduced by the band-pass filter $\delta\omega$.

The envelope detector tracks the slowly varying amplitude (envelope) of an oscillating signal while suppressing the rapid carrier oscillations and returns a corresponding DC level. In the context of squeezed light, the envelope detector is important to turn the varying noise level of detected squeezed and anti-squeezed states into a well-shaped sine-like wave. The exact output form depends on the amplifier chip used in the envelope detector. For this work a logarithmic amplifier was chosen, producing a large dynamic signal from a small initial amplitude. This signal enters the demodulation stage (also called mixer), where it is multiplied with the same frequency f_m as the modulation frequency. To achieve maximum phase synchronization, the modulation and demodulation frequencies should originate from the same frequency generator. If the phase between modulation and demodulation is tuned correctly, the output of the demodulation stage is the error signal ϵ, proportional to the derivative of the output of the envelope detector, described by

$$\epsilon_{\text{lin}} \sim \frac{d}{d\theta}\left(\Delta^2\hat{X}(\theta)\right) = \eta\left(\Delta^2\hat{Y} - \Delta^2\hat{X}\right)\sin(2\theta)\delta\omega \tag{3.6}$$

for the case of a linear amplifier in the envelope detector. In contrast to McKenzie et al. [McK+05], we used a logarithmic one, which changes the error signal to

$$\epsilon_{\text{log}} \sim \frac{d}{d\theta}\left(ln\left(\Delta^2\hat{X}(\theta)\right)\right) = \frac{\epsilon_{\text{lin}}}{\Delta^2\hat{X}(\theta)}. \tag{3.7}$$

This led to the advantage that the error signal became asymmetric and more sensitive to phase changes at the squeezed quadrature. However, the range that can be assumed to be linear got much smaller, which reduced the robustness of the feedback control loop when stabilizing on squeezed states.

The error signal has zero crossings at $\theta = 0, \pi/2$ and an amplitude depending on the asymmetry of the quadrature variances. It vanishes for symmetric states and becomes larger for high squeeze and anti-squeeze values. The evolution of the signal is illustrated in figure 3.5. The zero crossings of the error signal correspond to the minima and maxima of the initial signal, e.g. to squeezed and anti-squeezed states. They are used as a reference to stabilize the phase of the read-out quadrature. This is done by the PID controller which turns the error signal into the steering signal for the actuators.

While the basic idea of modulating and demodulating the light to get a feedback signal is the same as in a Pound-Drever-Hall locking scheme [Bla01], the quantum noise lock does not require a cavity as a reference. It would be possible to also lock cavities using the quantum noise lock by directly dithering the length of the cavity. As discussed in chapter 6, the quantum noise lock can have the downside of inducing extra phase noise to the signal.

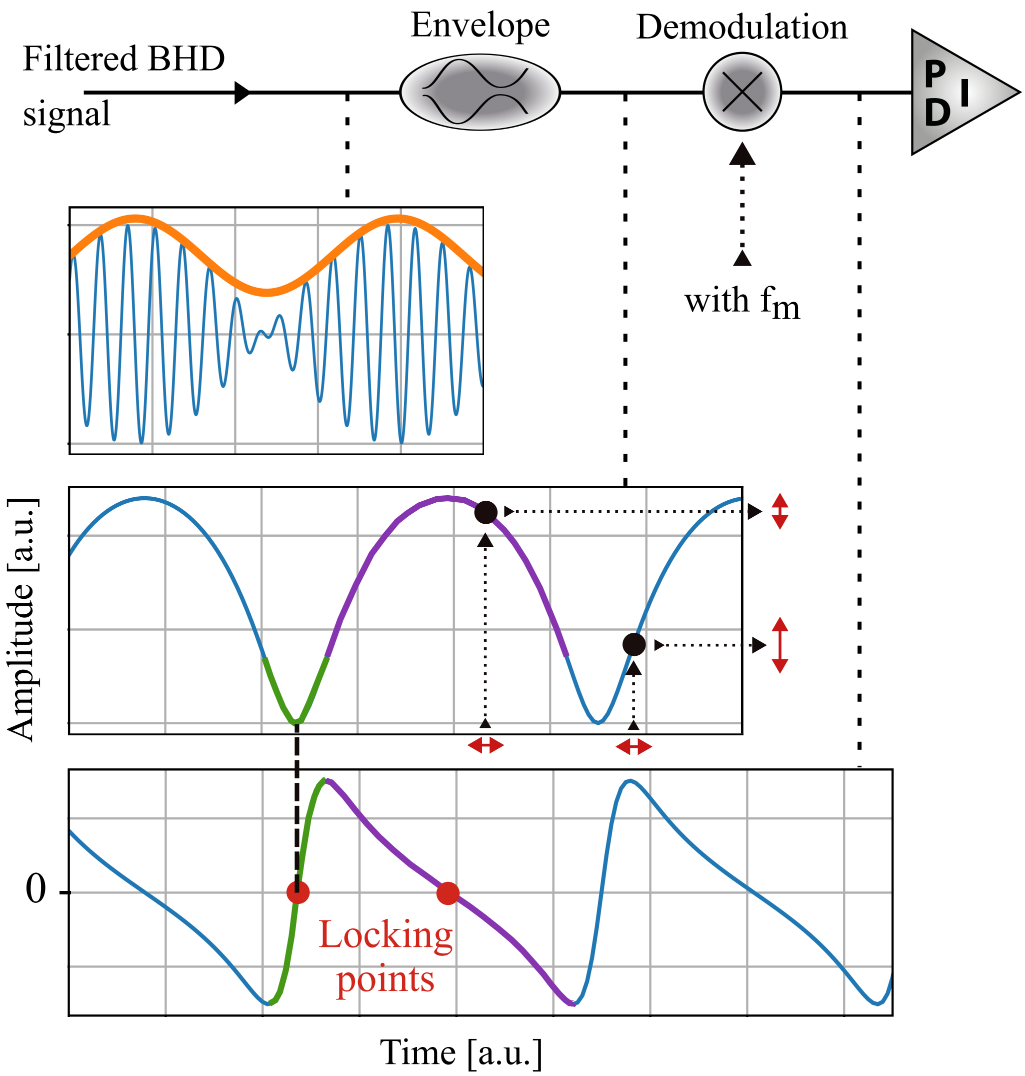

Figure 3.5: Signals at different stages of a quantum noise lock. Top plot: the AC signal from the homodyne detector of a scanned squeezed state shows minima (squeezed noise) and maxima (anti-squeezed noise). In orange is the envelope of this signal. Middle plot: output of an envelope detector with a logarithmic amplifier. The feedback of a modulation is depicted with the black dots and red arrows. Bottom plot: the output of the demodulation stage, which is the error signal and originates from the multiplication with the modulation frequency. The zero crossings (red dots) are the working points for the PID controller.

3.3 The QKD protocol

In this section, the various steps of the protocol used for one-sided-device-independent CV-QKD based on two-mode squeezed vacuum states are described, based on the work of [Fur+12; Wal+16].

Generic QKD protocols start with the preparation and distribution of N quantum states between the two parties, Alice and Bob via a quantum channel. A fraction k of the measurement results is used for the estimation of Eve's knowledge about the remaining data points, which would be $n = N - k$. From n, a secret key with length l is generated, using methods of postprocessing and privacy amplification.

Prerequisites: Besides the quantum channel that connects the laboratories of Alice and Bob, they need an authenticated classical channel for further communication. It is assumed that such a channel exists. Moreover, their measurement stations have to be secure, such that no information leaves the station unintentionally. Both stations are also equipped with a quantum random number generator (QRNG) and a balanced homodyne detector. At Alice's station, EPR entangled states are generated, meaning states that beat the EPR-Reid criterion as described in 2.3.2.

Generation, distribution and measurement of quantum states: Alice generates two-mode squeezed EPR-entangled states and keeps one subset for her own measurement. The other one is sent via the quantum channel to Bob's measurement station. They both use balanced homodyne detectors to perform measurements on their subsets, either in the X or Y quadrature, which is chosen by the QRNG at random. They repeat the measurement process on $2N$ quantum states until they both have generated a data set with $2N$ samples.

Abort conditions and sifting: After the measurement is done, abort conditions (i.e. the quality of their correlations) are checked and the protocol is aborted if necessary. Otherwise, Alice and Bob use the classical channel to compare their chosen measurement quadratures with each other. They discard all samples with different bases, which makes up approximately 50 % of the whole measurement outcome, leaving a sample length of N for the key generation. The discarded data points can be used in the next step.

Parameter estimation: In this step, Alice and Bob use samples discarded during sifting and a randomly chosen common subset of length k of the sifted data points and share them via the classical public channel. From the result, they can estimate the quality of their correlation, i.e. the amount of information leaked to Eve and the error rate for the error correction. All shared data points are discarded.

Binning: Before the start of the protocol, Alice and Bob determine the bins in which they will divide their measurement spectrum. All unrevealed data points are now mapped to the corresponding bins, resulting in two raw key bit strings. The binning process involves the trade-off between more bins and the bit error rate. In a realistic scenario, some of Alice's bits that are close to the edge of a bin, will not end up in the same bin as Bob's bit although the measurement basis was the same, due to uncertainties and imperfections. This causes an error in the raw key bit string. The bit error rate is the amount of errors in relation to the total amount of samples. More bins lead to more bin edges and more bits that are close to those edges and thus to a potentially higher bit error rate.

Error correction: The bit strings generated in the previous step are supposed to be identical but due to the finite strength of the squeeze values that lead to a finite strength of the correlations, they are not. Errors have to be corrected for by using error correction algorithms. There are two options to perform error correction: either Bob's errors are corrected and matched to Alice's data. This is called *direct reconciliation*. Or vice versa, Alice's data is corrected to match Bob's values, which is called *reverse reconciliation*. Applying an error correction algorithm reduces the key length even further, depending on the results from the parameter estimation step and the bit error rate.

Privacy amplification: In this final step, any correlations of the key to Eve are eliminated. This is done by Alice and Bob calculating a secure key length l and reducing their bit strings to that length, using two-universal hash functions. The secure key length depends on the amount of information leaked to an eavesdropper. Only a positive l leads to a secret key shared by Alice and Bob.

CHAPTER 4

Experimental setup

The setup on which my work and results are based is located in two different laboratories in different buildings, connected by the fibers described in section 4.3. The two buildings are the Institut für Quantenphysik (IQP) and the Zentrum für optische Quantentechnologien (ZOQ). Both are located on the campus of the Universität Hamburg in Bahrenfeld. In this chapter, I describe both experimental setups on the corresponding optical tables and provide schemes, drawings and pictures.

4.1 Building A: IQP

The squeezed and entangled states are generated in the IQP. Here, the main laser and amplifier are located, they provide up to 2 W of 1550 nm light which is divided into several optical paths. The amount of light used in each path can be adjusted using halfwave plates in combination with polarizing beam splitters. Most of the optical power is used to pump the SHG (path A) to generate 775 nm light, which is then used to pump the two squeeze lasers (blue box in figure 4.1). the squeeze lasers require different pump powers and the ratio can be adjusted with polarizing beam splitter F. Furthermore, a phase-shifting mirror is placed in front of each squeeze laser to tune the phase of the generated squeezed light. With both squeeze lasers operating,

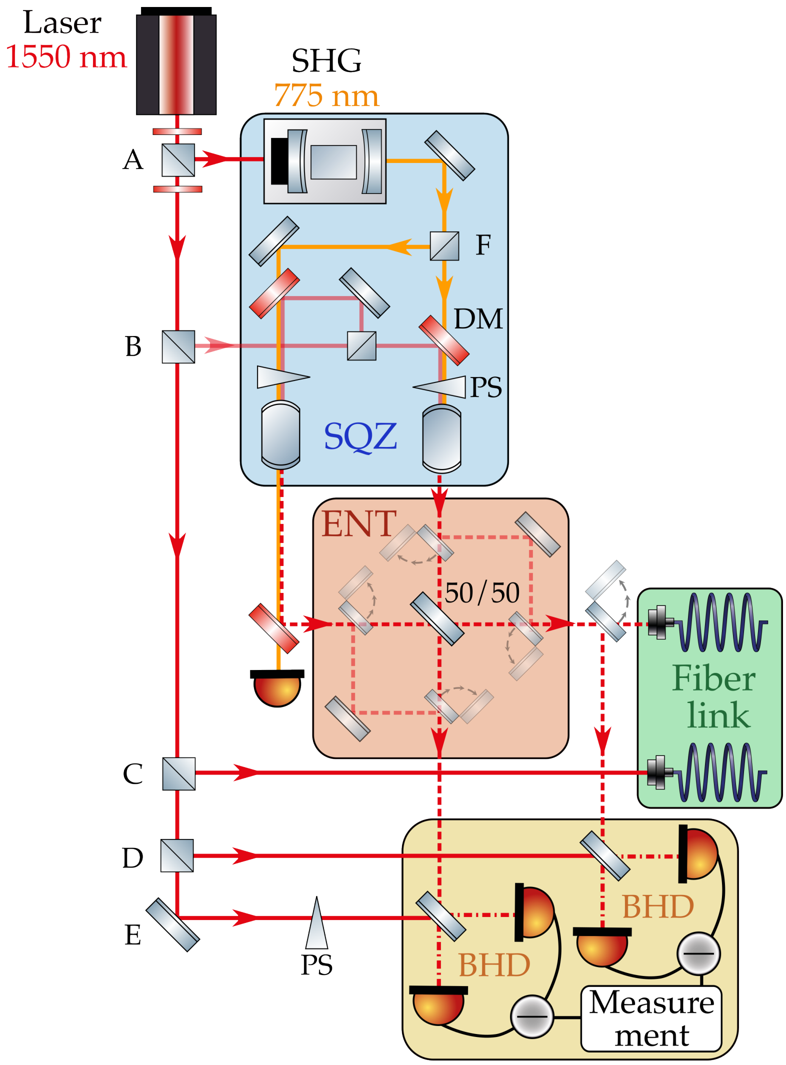

Figure 4.1: Schematic setup of the optical table in Alice's lab (IQP). The 1550 nm light is split into different beam paths (A-E). The power in each path can be adjusted using a combination of half-wave plates and polarizing beam splitters (PBS). PBS A is for the SHG path where the squeezed light is generated (blue box), B for the control beam, C, D and E to adjust the power in the LOs of the different BHDs, and F for the pump power of each squeeze laser. The entanglement beam splitter (red box) can be bypassed with flip mirrors to measure squeezed light from each squeeze laser separately.

the squeezed vacuum states can be overlapped on a beam splitter to generate two-mode squeezed states, as described in section 3.1.2 (red box in figure 4.1). The entangled states are either measured directly with two homodyne detectors in the IQP or half of them are transmitted via fiber to the ZOQ and measured in the ZOQ and IQP with one homodyne detector respectively. The entanglement beam splitter can also be bypassed using flip mirrors to measure the output of each squeeze laser separately without introducing 50 % loss. The setup for that is indicated by the semi-transparent dashed lines and flip mirrors.

The remaining 1550 nm light not used in path A serves as the optical local oscillator for the homodyne detection (paths C, D and E) as well as for locking and alignment purposes. For alignment, light can be shifted to beam path B to send a bright 1550 nm field through the squeeze lasers. This field allows the mode overlap on the balanced beam splitters to be optimized, using diagnostic mode cleaners. For clarity, they are not shown here, the principle is explained in section 4.2.

Many components in the setup require power supply and/or control electronics. An electronic rack in the IQP laboratory provides the necessary power for small devices on the optical table. Furthermore, it contains a high-voltage supply as well as space for PID controllers, temperature controllers and high-voltage amplifiers.

Several measurement devices are located in this laboratory: spectrum analyzers from *Rohde & Schwarz* are used for small data sets (e.g., single squeezing traces with a short measurement duration or low sampling rate). Oscilloscopes from *Keysight* and *Gwinstek* are used to display time traces from photo diodes, PID controllers and other devices. A PC containing a data acquisition card (DAQ), as described in chapter 7, is used for the measurements of entangled states.

4.2 Building B: ZOQ

The setup in the ZOQ (figure 4.2) is, compared to the IQP, a less complex remote measurement station, set up on a breadboard to have it transportable and flexible. Since the fibers are not polarization-maintaining and require polarization control and adjustment, each fiber first passes through a manual fiber polarization controller. Those consist of three paddles that contain loops of the fiber and can be tilted by 180° for stress-induced birefringence

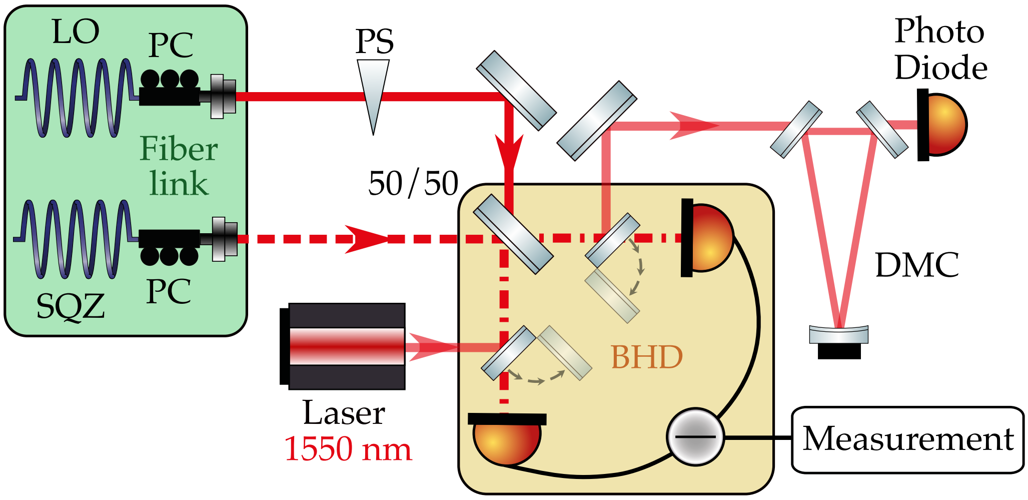

Figure 4.2: Setup in Bob's remote laboratory in the ZOQ. The fibers coming from the IQP first pass through polarization control (PC) to adjust the incoming light to s-pol. Multiple phase-shifting (PS) elements are implemented in the LO path. The LO is overlapped with the squeezed light on a 50/50 beam splitter for the balanced homodyne detection (BHD). With a flip mirror, a diagnostic mode cleaner (DMC) can be accessed to optimize the mode overlap at the beam splitter. A small seed laser (max. 60 mW) can be coupled into the fibers from the ZOQ side to send a coherent light field through the fibers to the IQP for alignment.

to change the polarization. Depending on the number of loops spooled up in one paddle, either a quarter or a half-wave plate can be created. The light of the local oscillator passes through multiple phase-shifting elements, before it is overlapped on a 50/50 beam splitter with the squeezed light from the second fiber. I used a diagnostic mode cleaner (DMC) to optimize the mode overlap at the beam splitter. For this technique, both beams from the LO and the signal path are matched to a ring cavity one after the other. As the beam splitter is a common point in both paths, a high spatial overlap can be achieved with a good mode matching of both beams to the same cavity. The light is then detected by a balanced homodyne detector.

An extra seed laser is used for the mode matching from free space to the optical fiber in the IQP. Using a flip mirror, the light can be coupled to the fibers from the ZOQ side and serve as a reference in the IQP.

The electronics (e.g. power supply, high-voltage power supply) are provided via a small electronic rack which was designed and built for this purpose by Dieter Haupt. Since this laboratory is not a cleanroom, I built a housing that surrounds the entire optical setup (see picture 4.3). The same measurement devices as in the IQP are used here: a spectrum analyzer, an oscilloscope from *Keysight* and a PC with a DAQ of the same kind as the one in the IQP.

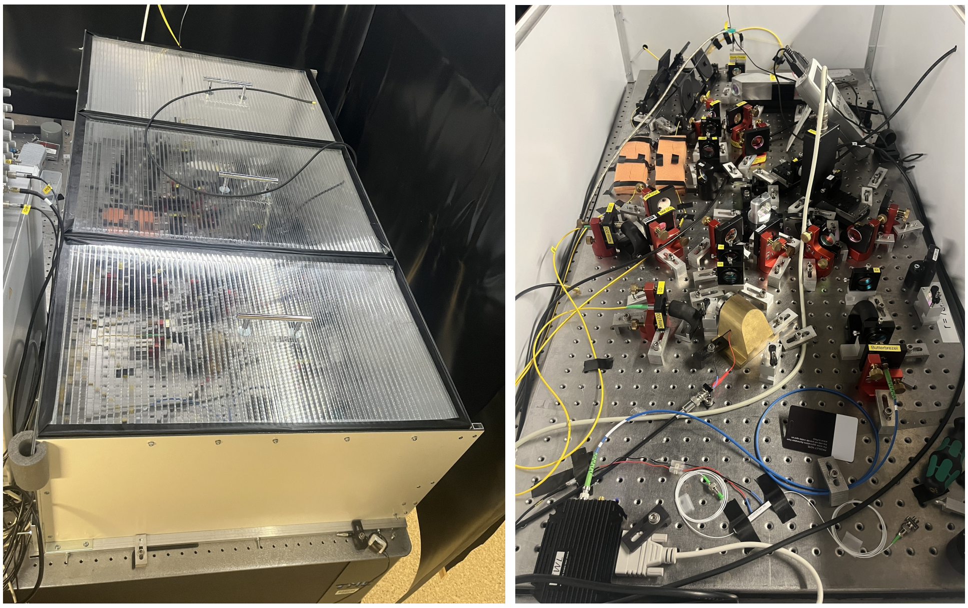

Figure 4.3: The setup in the ZOQ with the self-built housing. Left side with covers closed, right side with covers open. In the upper left corner, the polarization control is visible.

4.3 Quantum channel: The 1 km fiber link

We use two fibers in the experiment, one for the transmission of the local oscillator and one for the transmission of the quantum states. Both fibers are 1 km long and of the type smf28. These are ultra low loss non-PM single-mode fibers with a silica core as described in section 2.7. They are surrounded by a cladding and a jacket for maximum protection. Most of the fiber is spooled up and located under the optical table of Alice in the IQP (figure 4.6 d). About 180 m of each fiber leave the IQP laboratory and cross the basement of the building, entering a tube that connects this basement with the one in the ZOQ (see figure 4.4). The fibers go through the tube, along with other electrical cables (figure 4.6 c), including the cable that is used for the entanglement lock (see chapter 7). In the basement of the ZOQ, the fibers are guided on cable trays and along electrical conduits to the hole that connects the basement with Bob's laboratory (figure 4.6 e).

The fibers are taped together every two meters and are deployed as close as possible to each other in order to maximize common mode noise for a better rejection during detection. Wherever possible, they are surrounded by tube insulation (figure 4.6 b) and electrical conduit for further protection from outer disturbances. All four fiber ends in the two laboratories have FC/APC connectors and are coated with anti-reflection coatings. They are connected with a splice to the rest of the fiber. The splice can be seen in figure 4.5 in the background.

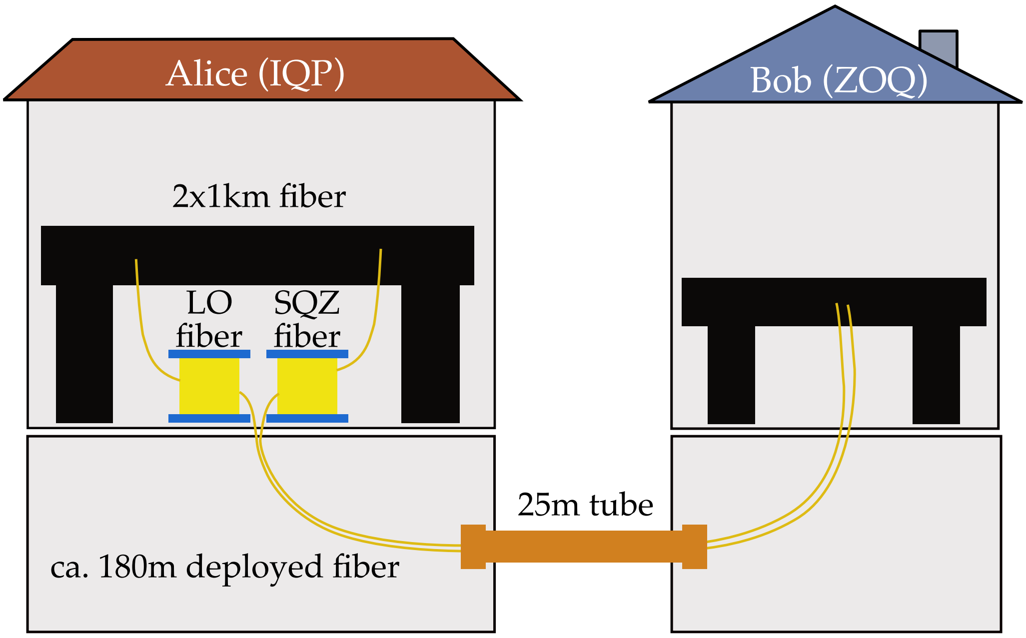

Figure 4.4: The fiber spools are located in Alice's laboratory. They are guided down into the basement through holes in the floor (figure 4.6 a), cross the basement and a 25 m tube to the basement below the ZOQ. Here, they follow cable trays with other electrical cables to the hole that leads to the lab of Bob.

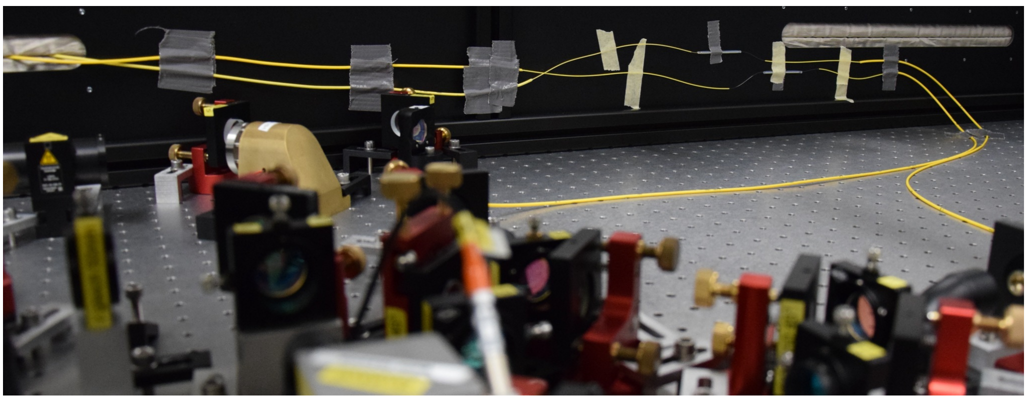

Figure 4.5: The fibers on the optical table in the lab of Alice. The gray parts in the upper right corner are the splices. The transitions from bare fiber to jacket to cladding (both yellow) are visible.

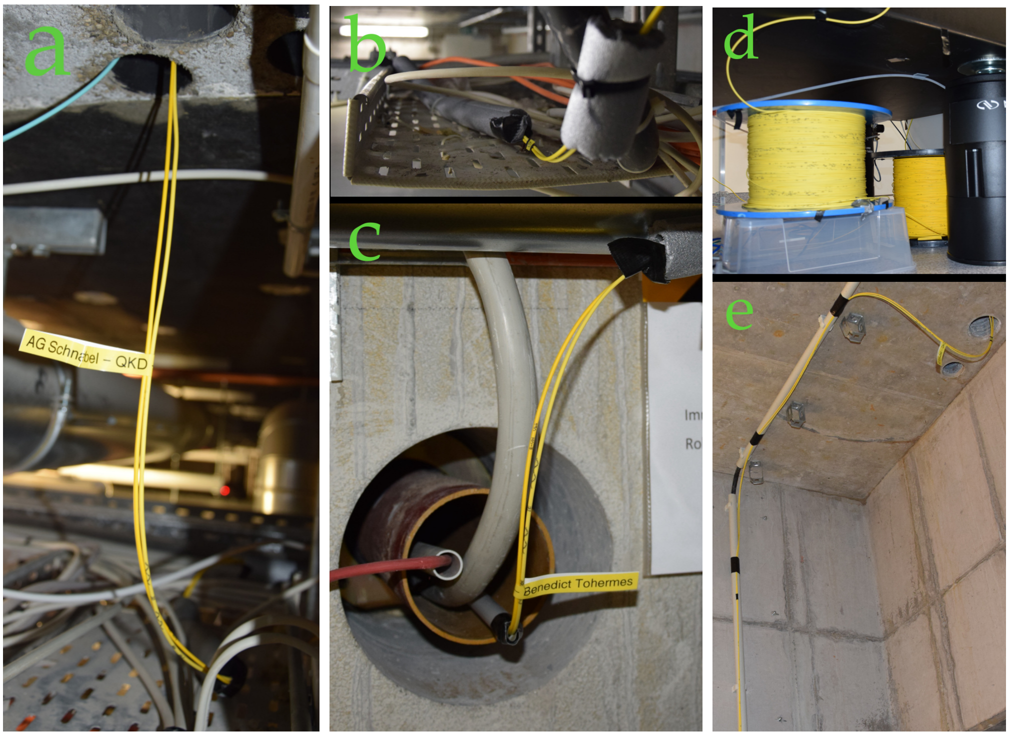

Figure 4.6: Impressions from the fiber link between the two laboratories. a: the fibers coming from the lab of Alice into the basement underneath the IQP. b: They are taped together and shielded in tube insulation if possible. c: The tube that connects the two basements of IQP and ZOQ with each other. d: Both fiber spools with most of the fiber below the optical table in the lab of Alice. e: The fiber in the ZOQ basement, fixed to another tube for electrical purposes. The hole in the ceiling leads to the lab of Bob.

CHAPTER 5

Long term evaluation of monolithic squeezing resonators with GHz bandwidth

I worked with Benedict Tohermes on the setup, alignment and characterization of two monolithic cavities with GHz bandwidth, as described in section 3.1.1. They are the essential elements in our QKD setup, however, they showed huge differences in their individual characteristics. While the details of the development and design are discussed in [Toh25], I want to focus in this chapter on the long-term evaluation and performance of the squeeze lasers. For this purpose, I tried to reproduce the spectrum measurements we did in 2023 for the publication [Toh+25]. The results are shown in section 5.1 in a direct comparison between the results of 2023 and 2025. During operation and use of the squeeze lasers, we noticed two unwanted effects which led to the assumption that the crystals may degrade over time. In sections 5.2 and 5.3, I describe the generation of 387.5 nm light by our crystals and the occurrence of liquid drops on the crystal surfaces.

The setup for the measurements can be seen in figure 5.1. Both squeeze lasers are located on the same table, with one homodyne detector for each squeeze laser. The light from the pump laser is split between the path for the SHG and the local oscillator path. Additionally, 1550 nm light can be coupled into the squeezing cavity to produce a coherent control spot at the output for mode matching purposes on a diagnostic mode cleaner (see

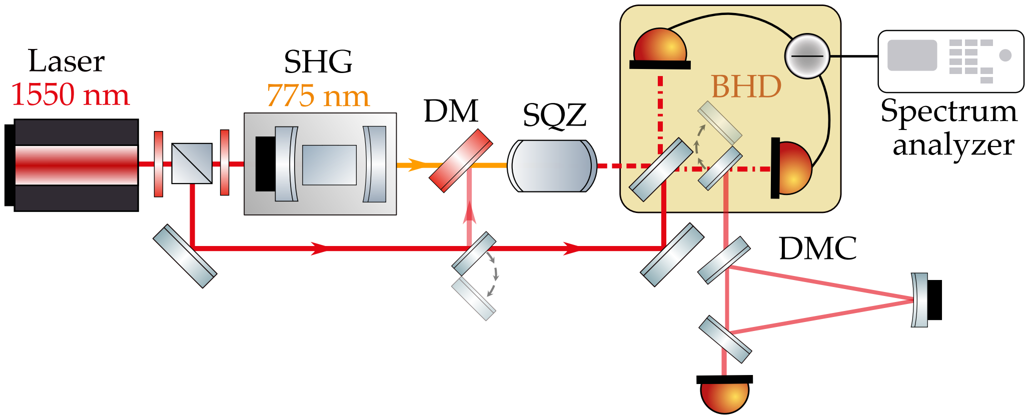

Figure 5.1: Setup for all measurements shown in this chapter. The light is emitted by a 1550 nm laser, mostly converted to 775 nm in the SHG and guided to the squeezing crystal. Another part of the 1550 nm light serves as the LO. A diagnostic mode cleaner (DMC) can be accessed with a flip mirror for the LO and the control beam (light red) to optimize the mode overlap at the beam splitter. The AC output of the homodyne detector is captured using a spectrum analyzer. The setup is identical for both squeeze lasers.

section 4.2 for a detailed description). To generate squeezed states, 775 nm light is used to pump the squeezing cavity. The resulting squeezed vacuum is overlapped at the 50/50 beam splitter in front of the homodyne detector. The data is recorded with a spectrum analyzer that acquires the AC signal from the homodyne detector.

5.1 Measurement results

The first results were measured in November 2023 by Benedict Tohermes and published in [Toh+25]. Although both crystals are from the same manufacturing batch, they show different behaviors concerning the non-linearity and therefore the required pump power and (anti-) squeeze values. In 2023, we pumped squeeze laser 1 with 0.6 W and squeeze laser 2 with 0.3 W, both from the same second harmonic generator. This resulted in 5 dB noise suppression for squeezer 1 and 8.5 dB for squeezer 2 at a Fourier frequency of 30 MHz. The anti-squeeze values are about 7 dB for squeeze laser 1 and 20 dB for squeeze laser 2. Above 1 GHz squeeze laser 1 (2) showed 2.5 dB (4 dB) squeezing and 3 dB (4.8 dB) anti-squeezing. The values are dark noise corrected and were taken without a phase stabilization for the readout phase.

For comparison, I repeated the spectrum measurements with both squeeze lasers two years later (November 2025) and show the results in figures 5.4 and 5.3 next to the previous ones. Given the observed generation of UV light in both crystals and the occasional change in performance, these measurements can show the long-term development of our squeeze lasers and any degradation effects if they occur.

In figure 5.2, the linearity measurements of homodyne detector 1 and 3 can be seen, which I used for the measurements in 2025. They were assembled by me (detector 1) and Benedict Tohermes (detector 3). Note that detector 1 and 2 were used in the measurements of 2023. All three existing detectors show a linear behavior, i.e. a 3 dB increase in noise power when doubling the local oscillator power. However, they show electronic features at differing frequencies. For a better overview, table 5.1 assigns the squeeze lasers and used homodyne detectors for both years.

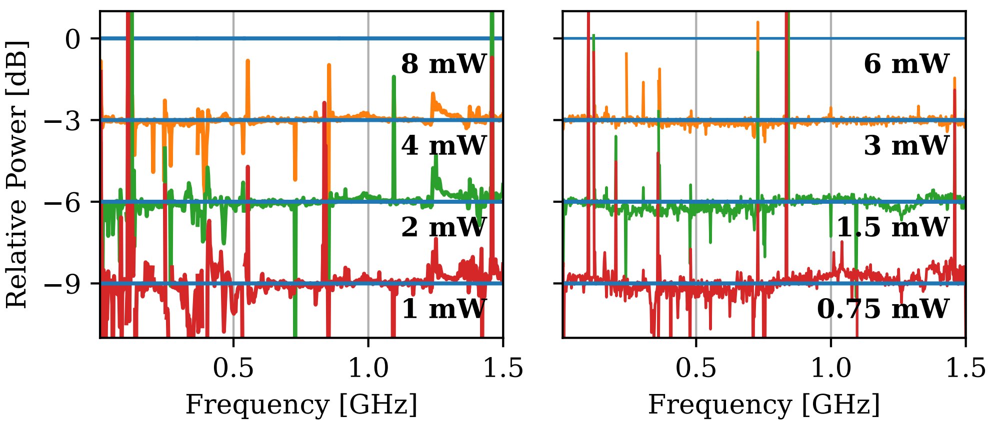

Figure 5.2: Linearity measurements of homodyne detector 1 (left) and homodyne detector 3 (right). They show a linear behavior over the whole measurement range but especially at lower frequencies, some noise peaks are visible. For the spectrum measurements shown in this chapter, I used 6 mW and 5 mW LO power respectively.

year	Squeeze laser	Balanced homodyne detector
2023	Squeezer 1	BHD 1
	Squeezer 2	BHD 2
2025	Squeezer 1	BHD 3
	Squeezer 2	BHD 1

Table 5.1: Overview of the used homodyne detectors with the corresponding measurements in 2023 and 2025. In total three detectors and two squeeze lasers exist.

In figures 5.3 and 5.4 the two spectrum measurements are compared to each other. The red dotted lines are the theoretical fits for squeezing and anti-squeezing, based on the equation derived from section 2.2.2:

$$S^{\eta}_{\text{sqz,asqz}} = 1 \mp \eta \frac{4\sqrt{\frac{P}{P_{\text{thr}}}}}{\left(1 \pm \sqrt{\frac{P}{P_{\text{thr}}}}\right)^2 + 4\left(\frac{f}{\gamma}\right)^2} \tag{5.1}$$

Comparing the spectra of the two cavities after two years of intensive use with UV light production as a side effect reveals that no strong signs of degradation are visible.

Squeeze laser 1 hardly changed at all, the numbers for the cavity linewidth remained the same. The pump power was a bit lower in 2025, which explains the tiny deviation in the maximum anti-squeeze levels. It was not possible to pump with 600 mW as we did in 2023 since the performance of the SHG decreased and produced a maximum of about 550 mW in 2025 instead of about 900 mW in 2023. It is also not possible to know the exact pump power that is coupled into the crystals. We can measure the value in front of each squeezer, but the amount that enters the cavity depends on two parameters: the mode matching of the pump light to the cavity and the operation point with respect to the resonance peak. Due to stability reasons, the squeeze lasers could not be operated exactly at resonance, but at a value lower than the maximum. We used the temperature controllers (see 3.1.1) to tune the temperature for resonance and phase matching and approached the correct peak by cooling the peltier elements down. Close to the maximum, the cavities are highly unstable and small fluctuations cause them to jump over

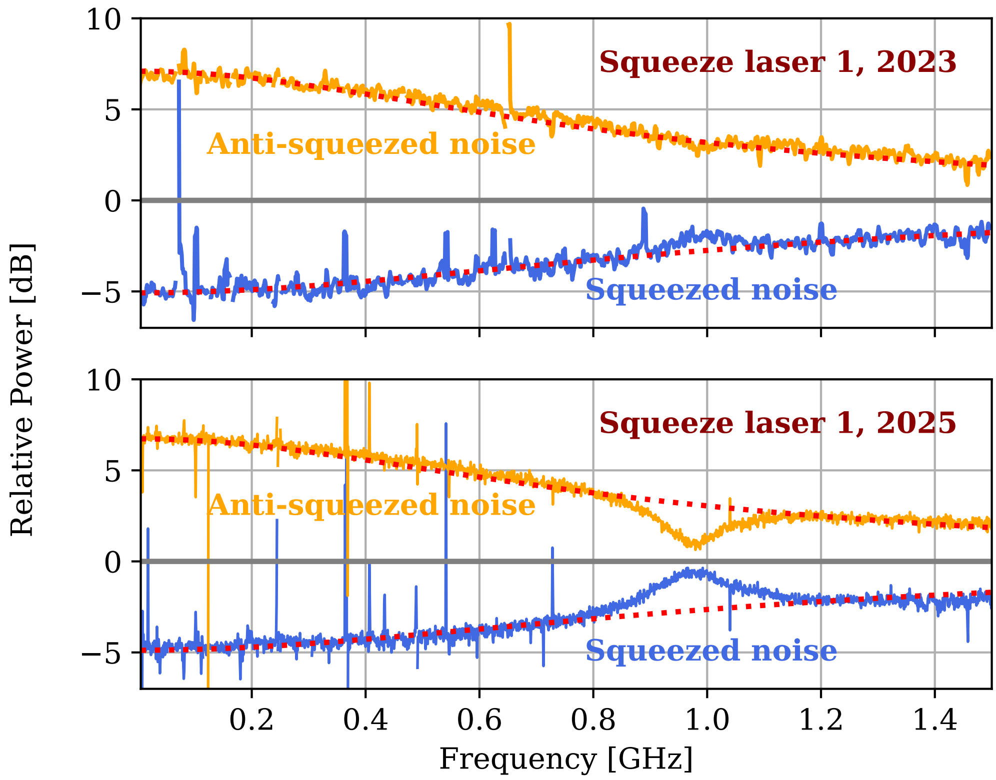

Figure 5.3: Spectrum measurement and theoretical fit (dotted red line) from squeeze laser 1 in comparison with the spectrum from 2023. For the recent measurement, I used 5 mW local oscillator power and 530 mW pump power, compared to 600 mW pump power in 2023. The dip at around 1 GHz is caused by homodyne detector 3 (in 2023 detector 1 was used) and is not a property of the squeezing cavity. The spectra look very similar, no signs of degradation are visible.

the resonance peak. For measurements, we therefore used 70-80 % of the peak height to have a stable generation of squeezed light.

Squeezer 2 shows a lower maximum anti-squeezing in the more recent measurement. This can be explained by a lower pump power. Although I tried to use the same conditions as in 2023 and measured 300 mW in front of the cavity, it is possible that less of it got coupled into the cavity as explained above. Additionally, the losses are higher, which can be inferred from the decreased maximum squeeze value. Since this crystal showed liquid drops on the coating as described in section 5.3, I would assume that the

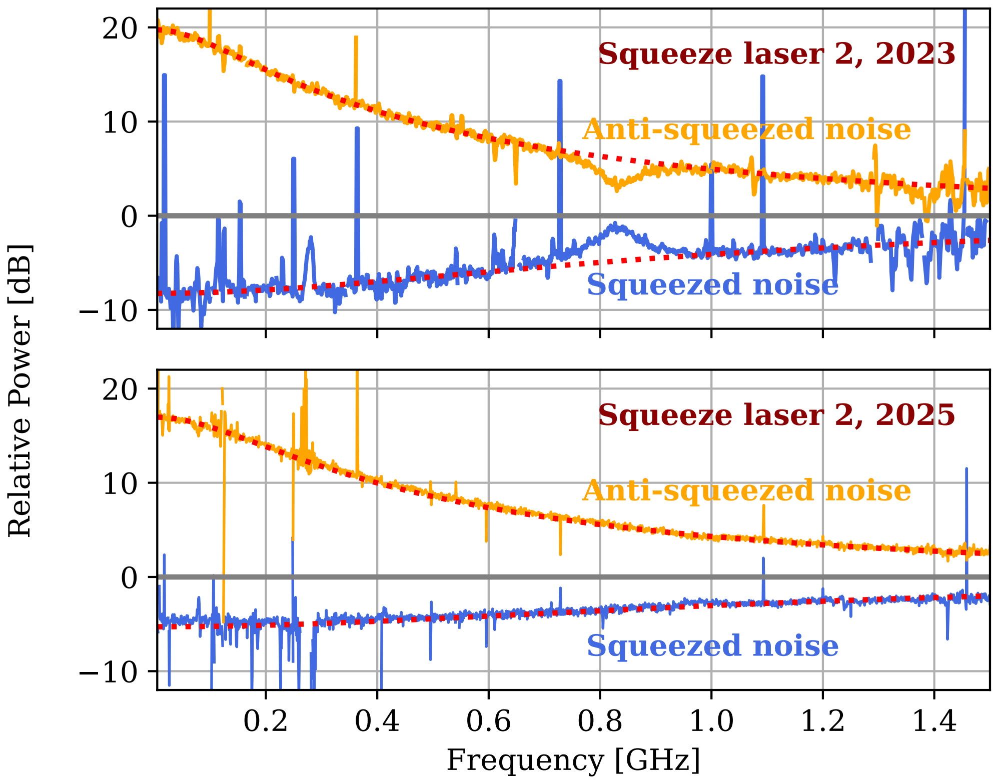

Figure 5.4: Spectrum measurement and theoretical fit (dotted red line) from squeezer 2 in comparison with the spectrum from 2023. For the recent measurement, I used 6 mW local oscillator power and 300 mW pump power, the same as in 2023. The new data was recorded using homodyne detector 1. In 2023, detector 2 was used, which caused the dip about 0.83 GHz. It is visible in the plot that both well the anti-squeeze and squeeze values are lower in the new data. The former points to a lower effective pump power, as described above. The latter is a strong indication for increased losses, confirmed by the numbers for η in table 5.2. The cavity linewidth however, is still comparable to the one fitted in 2023.

	Squeezer 1		Squeezer 2	
	2023	2025	2023	2025
η [%]	(82.8 ± 1.6)	(82.5 ± 2.7)	(85.8 ± 1.1)	(71.4 ± 0.8)
$\frac{P}{P_{thr}}$ [%]	(17.77 ± 0.79)	(16.18 ± 2.29)	(68.19 ± 0.1)	(61.7 ± 0.67)
γ [GHz]	(2.053 ± .064)	(2.053 ± .036)	(1.750 ± .013)	(1.769 ± .033)

Table 5.2: Fit parameters calculated for the two cavities with data from 2023 and 2025. The numbers for 2023 were taken from [Toh+25]. The numbers for 2025 were calculated using a SciPy fit algorithm. The dips caused by the homodyne detectors were excluded from the fitting data in both years.

extra amount of losses is rather caused by residues of the drops than by internal cavity defects.

Lastly, the fit parameters displayed in table 5.2 show that the linewidth of squeeze laser 2 is slightly higher than in 2023. This would be the only hint for internal cavity destruction since defective parts lead to higher absorption and therefore internal losses. This would be equivalent to a change in the reflectivities of the coatings which define the linewidth of the crystal (see section 3.1.1). However, the difference is within the error bar of the fit parameters, hence I would not assume a significant degradation of the crystal. The fit parameters for the measurement from 2023 are the ones calculated back then and published in [Toh+25]. For the recent spectra, I calculated new fit parameters based on the new data measured.

In the next two sections I briefly describe the problems that occurred during the operation of the squeeze lasers and pointed to the possibility of crystal degradation.

5.2 UV light generation

While operating the squeeze lasers and pumping them with 775 nm light, we observed 387.5 nm light being emitted from the squeezing cavities. This occurred most likely as an SHG process from the 775 nm pump light in the squeezing resonator and has been reported before in [Ast15], who worked with a similar setup. It was not possible to quantify the exact amount of produced and emitted UV light, since we had no way to separate it from the other emitted wavelengths. From measurements with a 775 nm HR mirror and estimations based on the brightness of the 387.5 nm light spot on a piece of paper, we assume the power to be approximately 1 mW at one of the squeeze lasers.

Besides the potential danger of UV light to the eyes and skin, it has the potential to damage a crystal, especially with a small beam waist and high intensities, as is the case here. Gray tracking can be a direct effect as described by [Bou+99; Loi+92; Hir+07], leading to higher absorption and losses at 1550 nm as a consequence. Internal losses have a negative impact on the maximum achievable squeeze value. It is highly desirable to avoid any internal damage to squeezing crystals to circumvent extra thermal effects and maintain optimum performance.

5.3 Unknown liquid on the crystal surfaces

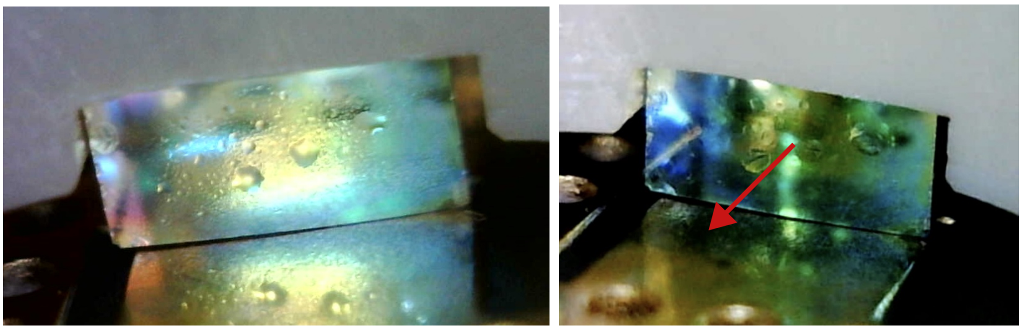

Figure 5.5: Crystal from squeeze laser 2 at the out-coupling side. Drops of unknown origin and their position in the beam axis (red arrow) are clearly visible.

During measurements with the squeeze lasers, we noticed increasing losses after some months of operation. Investigating this further, we found the spot behind the crystals to be very divergent and blurry. When looking with a USB microscope at the crystal surfaces we found drops of a liquid on the coatings (pictures are shown in figure 5.5). As we didn't have the opportunity to analyze the liquid, we could not tell what they are made of or where they came from. The assumption that it might have outgassed from the thermal paste we used to get a good contact between the peltier elements and the PCB board, turned out to be wrong. The problem occurred again after removing the paste completely and cleaning all parts that were in contact with it. Condensation of water from the air is very unlikely, since the temperature and humidity in the laboratory are controlled and stabilized and the temperature gradient to the crystals is not high enough for water to condense on the surfaces. Heating the crystals for a day with the peltier elements to about 60° C to evaporate the drops did no show any effect. We cleaned the surfaces with clean room Q-tips and isopropanol, and although it was not possible to remove the drops completely, we could move them out of the beam axis and recover the previous squeeze values. The liquid appeared on both crystals and returned some months after the cleaning. The origin of those drops is unknown.

5.4 Conclusion

Despite two different problems with the monolithic cavities, a two-year long-term investigation revealed no definite signs of permanent crystal damage or degradation of squeeze factors. Neither the spectrum measurements nor the calculated cavity parameters could support the assumption of irreparable internal damage. That allows for two different conclusions: Either the damaged spots vanished over time as described in [Hir+07] or the observed temporary setbacks in the performance are caused by other sources, such as mode matching, power fluctuations of the SHG or the wrong temperature at the peltier elements.

CHAPTER 6

Phase-stabilized distribution of squeezed vacuum states over 1 km optical fiber

The distribution of squeezed or entangled states over an optical fiber outside of a temperature stabilized laboratory adds extra phase noise to the states. The fibers pick up all kinds of noise, seismic, acoustic, and temperature drifts. This leads to very noisy squeezing measurements in the lab of Bob, shown in the zero span measurement in figure 6.1. The traces were recorded without phase stabilization after the squeezed states passed through a 1 km optical fiber from the IQP.

With states like that, it is not possible to implement a QKD protocol. It was therefore my task to develop a phase lock to suppress the noise and stabilize the read-out phase. The setup and measurement results with squeezed vacuum states are presented in this chapter.

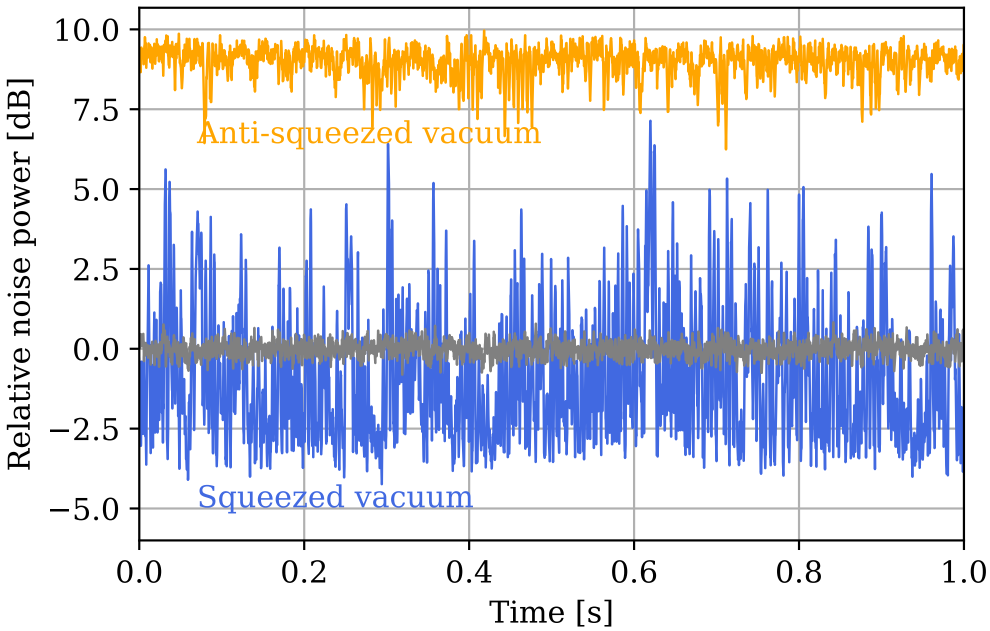

Figure 6.1: An unstabilized zero span measurement in the lab of Bob after 1 km optical fiber transmission. It is clearly visible that the impact of phase noise is higher on the squeezed states than on the anti-squeezed states, as explained in section 2.2.3. The shot noise trace is shown in gray.

6.1 Configuration of the quantum noise lock

The control loop I built for the phase stabilization of distributed squeezed vacuum states is a quantum noise lock, as described in section 3.2. Since a squeezed vacuum state is asymmetric with squeezed and anti-squeezed quadratures (see section 2.2), it shows noise minima and maxima when the phase gets rotated. This behavior can be used to generate the error signal for the feedback loop. Most parts of the feedback control loop were realized using a Moku:Pro from *Liquid Instruments*, an FPGA-based device, that combines several useful tools.

Figure 6.2 shows the details of the different elements of the control loop. The local oscillator and the squeezed states are transmitted in two separated fibers. An external frequency generator modulates the light from the local oscillator with a frequency of 1 MHz, using a fiber-based electro-optical

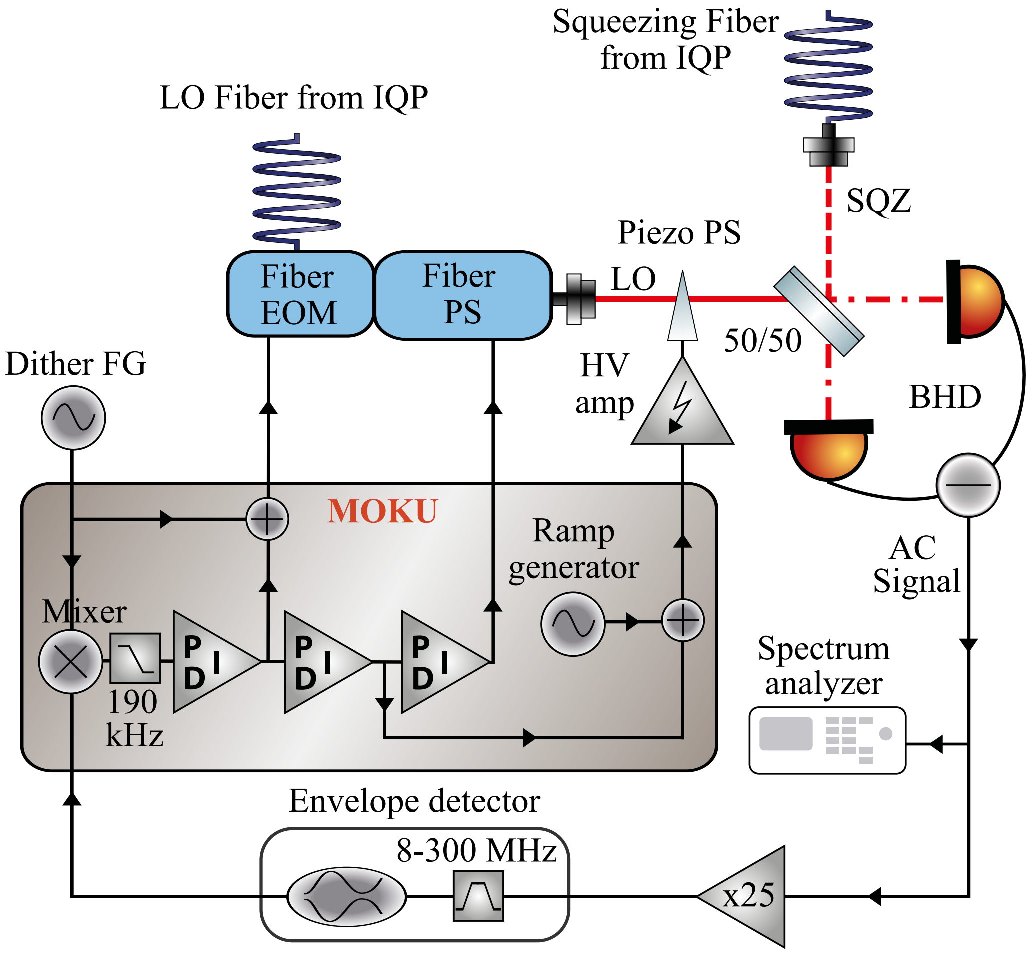

Figure 6.2: Detailed setup of the control loop for the phase between read-out quadrature and squeezing quadrature. Using a frequency generator (FG), a modulation is imprinted on the light of the local oscillator (LO), which is overlapped with the signal beam and detected by a homodyne detector. The AC signal from the detector is divided between the spectrum analyzer and the control loop. Before the signal is guided into the Moku:Pro, it passes through a gain box and an envelope detector, which consists of an 8 - 300 MHz low-pass filter and a logarithmic amplifier. Inside the Moku:Pro, the demodulation stage and three PID controllers are realized. They steer three phase actuators: A fiber EOM, a fiber phase shifter and a piezo mounted mirror. The EOM is also used to imprint the modulation frequency onto the light.

modulator (EOM). In total, there are three phase actuators: the fiber EOM, a fiber phase shifter and a piezo mounted mirror in the free space path.

The modulated light is detected by a self-built balanced homodyne detector and transmitted through its AC port to a signal splitter. Here, the signal is divided 50/50 for measurement and control loop. The light for the lock is first amplified by a self-built analog gain box with a gain factor of 25, using the operational amplifier THS3201. As the output of the homodyne detector is on the order of some mV, it must be amplified to achieve a signal level suitable for the analog-digital converter (ADC) of the Moku:Pro. Afterwards, the signal is processed by an analog envelope detector. This device detects the envelope of a wave and puts out the corresponding DC level. The chip used is the AD8310, which is a logarithmic amplifier and the output is therefore on a logarithmic scale. To meet the input requirements of the AD8310, a band-pass filter from 8 to 300 MHz is implemented before the envelope detector. Besides the gain box, the envelope detector and the frequency generator, all electronic devices were realized digitally in the Moku:Pro to which the output of the envelope detector is guided to.

The next step is the demodulation stage, also called mixer. Here, the signal is demodulated at 1 MHz using the same frequency generator that also modulates the light of the local oscillator. Following the mixer, a digital low-pass filter at 190 kHz and a gain of 60 dB are used to maximize the error signal and obtain a high signal-to-noise ratio. The resulting output signal is the error signal for the PID controller. In this lock, three PID controllers are used, one for each phase actuator. The fiber EOM works best for high frequencies, with an integrator frequency of 237.5 kHz, the mirror-mounted piezo is used for the intermediate region, with the integrator frequency of 419 Hz and the fiber phase shifter is responsible for slow drifts around 1 or 2 Hz and below, with an integrator frequency of 6.6 Hz. All integrators had different gain values: 0 dB (piezo), 3.5 dB (fiber phase shifter) and 34 dB (fiber EOM). The differential filter of the PID controller was not used.

In figure 6.3, a Bode plot of the transfer function of the control loop is shown with the original measurement data in orange and a filtered and averaged trace in blue. The phase shows atypical characteristics, probably due to the large number of filters in the setup. Despite this, positive gain and phase margins are visible. The unity gain bandwidth is at 1 kHz and the 180° phase flip occurs at 14 kHz. The plot confirms the experimentally observed stability of the lock, at the same time, it reveals potential for improvements.

The rising part of the phase plot starting at 1 kHz indicates, that the gain of the controllers was not optimally utilized in the frequency range below 3 kHz. Trying to increase the gain, however, led to oscillations of individual actuators. The drop in the amplitude plot at 1 kHz supports the assumption that the fine tuning between the three controllers and their actuators could be optimized to achieve a smooth transition, most likely leading to a higher unity gain bandwidth. Although parts of the feedback control were driven at their limits, especially the fiber phase shifter, the lock worked for my application and could be further improved for more bandwidth and stability.

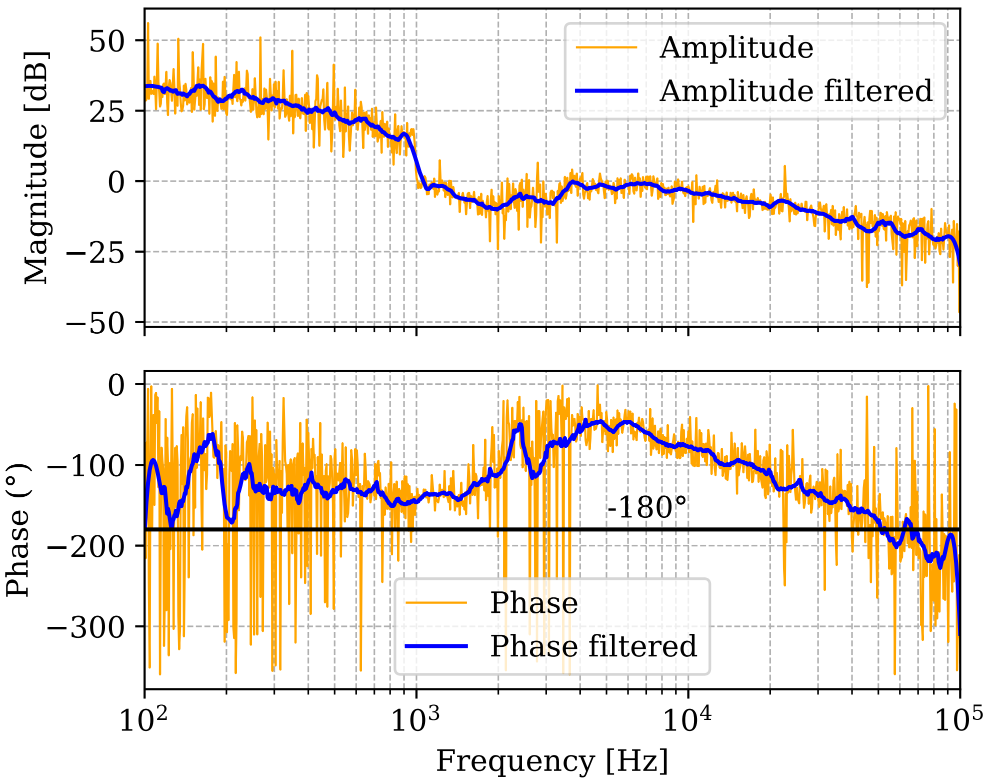

Figure 6.3: Transfer function of the control loop for distributed squeezing. Original measurement data in orange, filtered and averaged data in blue. It shows a unity gain bandwidth (UGB) of 1 kHz. The sharp drop at this frequency originates probably from the transition between the different PID controllers.

6.2 Remote squeezing measurement results

Figure 6.4 shows the schematic setup for the measurements. While the laboratory in the IQP provides the main laser and the squeezed light generation, the stabilization control and measurement take place in the remote laboratory in the ZOQ. The latter has neither a clean room environment nor seismic isolation. The two laboratories are connected by the fiber link described in section 4.3.

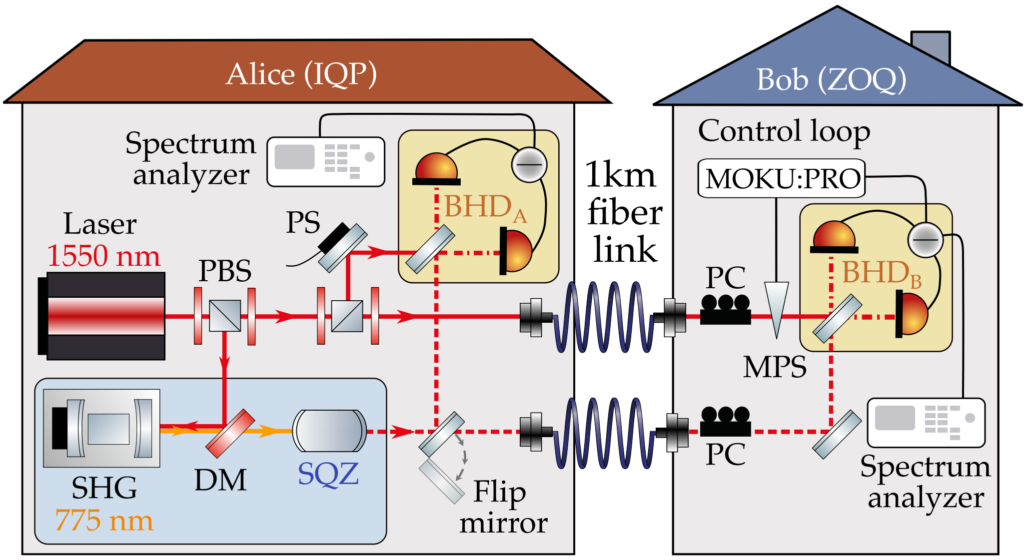

Figure 6.4: The squeezed light is produced in the IQP and is transmitted via optical fiber to the ZOQ. The quantum states and the local oscillator are transmitted in two separate fibers. Balanced homodyne detectors (BHD) are located in both buildings for the measurement of squeezed light. With a flip mirror, I chose at which site the squeezed light is measured. In the ZOQ is a polarization control (PC) for both fibers and the setup for the phase control loop. Multiple phase shifter (MPS) act on the phase for noise compensation.

Before taking a measurement, I sent a coherent field through both fibers from the IQP to the ZOQ and adjusted the polarization of each beam using the polarization paddles (described in section 4.2) to be in s-polarization. The coherent light fields were also used to realign the mode overlap on the balanced homodyne beam splitter in the ZOQ and to made sure that both photodiodes were illuminated properly. Afterwards, I returned to the IQP, tuned the squeeze laser on resonance and monitored the squeeze factor with the homodyne detector located in the IQP. I removed the flip mirror, changed the laboratory again and started the Moku:Pro in the ZOQ. With the provided options of gain, filters and offset tuning, the error signal was optimized. The integrators were activated from fast to slow, with the result of a phase stabilized squeezing measurement. The data were recorded using a spectrum analyzer from *Rohde&Schwarz*.

The measurements shown here were all taken with the same balanced homodyne detector (detector 2). In figure 6.5 the linearity verification is shown, which can also be seen in [Toh+25].

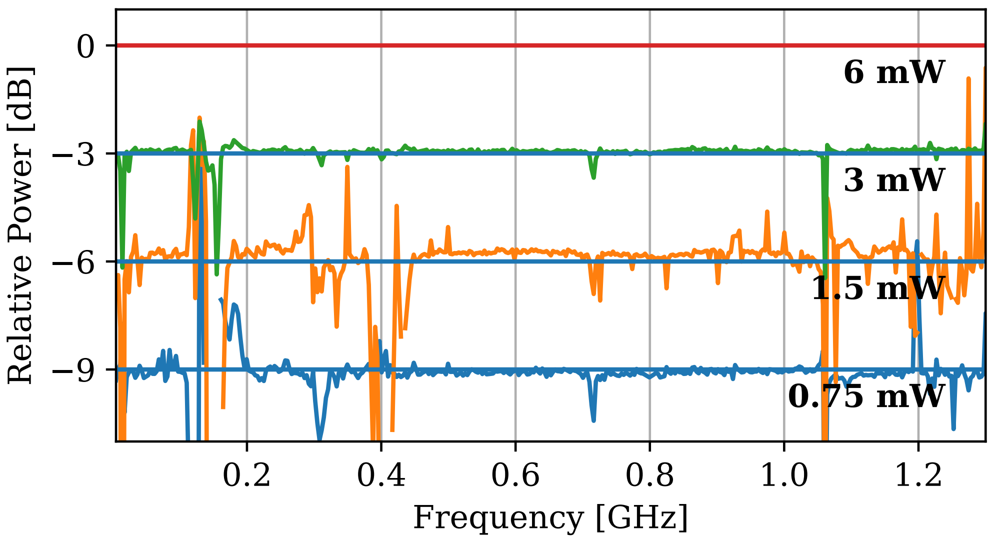

Figure 6.5: Linearity measurement of the balanced homodyne detector in Bob's lab (detector 2), normalized to 6 mW of power. It shows a 3 dB distance for doubling the local oscillator power and is therefore considered to have a linear behavior.

For each measurement, I recorded a dark noise trace containing the electronic noise from the balanced homodyne detector, a vacuum noise trace with the signal path blocked (local oscillator only), and two signal traces: one for the squeezed noise and one for the anti-squeezed noise. To switch between the two signal traces, I changed the lock point to the corresponding zero crossing of the error signal. That way, I could either lock to the minimum of my signal (squeezing) or the maximum (anti-squeezing). Subsequently, I subtracted the dark noise from the signal data and normalized the values to the shot noise level. Three different measurements were taken in order to characterize the squeezing results in the ZOQ.

The zero span measurements at four different frequencies (figure 6.6) allow for a detailed evaluation of selected sideband frequencies of the spectrum. They show up to 4.7 dB noise reduction up to 0.25 GHz and more than 2 dB above 1.2 GHz. The anti-squeezing is at 10 dB in the lower MHz region and decreases to 2.8 dB above 1.2 GHz.

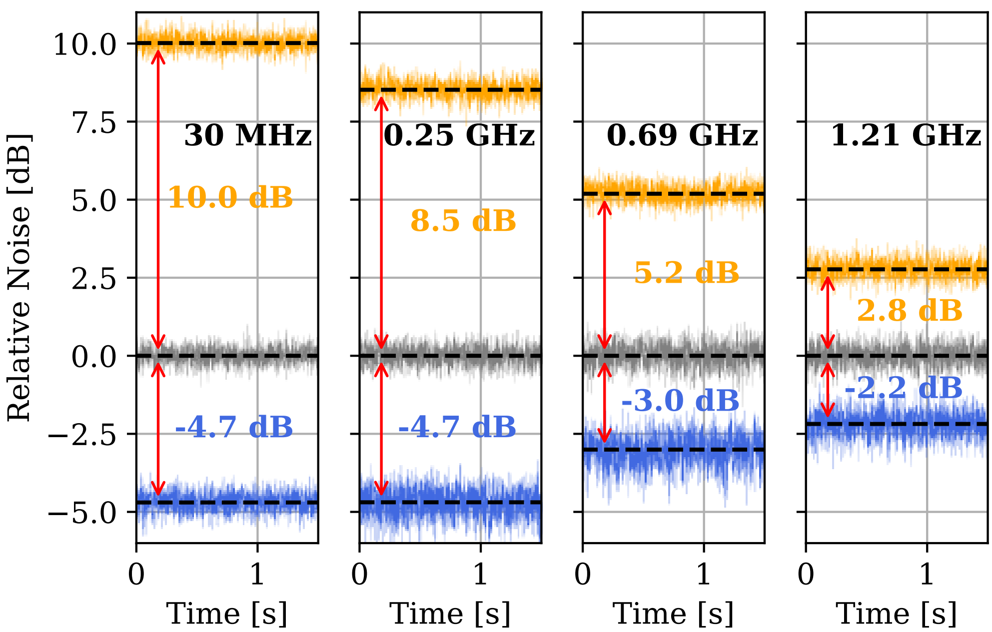

Figure 6.6: Zero span quantum noise measurements in Bob's lab at 30 MHz, 0.25 GHz, 0.69 GHz and 1.21 GHz. I measured up to 4.7 dB in the lower MHz range, up to 3 dB in the upper MHz range and more than 2 dB above 1 GHz. The anti-squeezing is at 10 dB at 30 MHz and decreases with rising frequencies. Above 1 GHz it is still at 2.8 dB. The values are dark noise corrected with a dark noise clearance to shot noise of 11 dB, 7.4 dB, 5 dB and 5.7 dB respectively.

For a QKD protocol it is necessary to have a long and stable measurement window, ideally of several minutes or even hours. I performed a five minute measurement (figure 6.7) to prove the stability of the feedback loop beyond the short duration of the usual zero span measurements, which is on the order of a few seconds. All traces were taken one after the other without interruptions. The result shows stable read-out phases with no peaks or disturbances at a squeeze level of 4.1 dB and an anti-squeeze level of 10.5 dB. A comparison with the unstabilized measurement (figure 6.1) emphasizes the effectiveness of the feedback control loop.

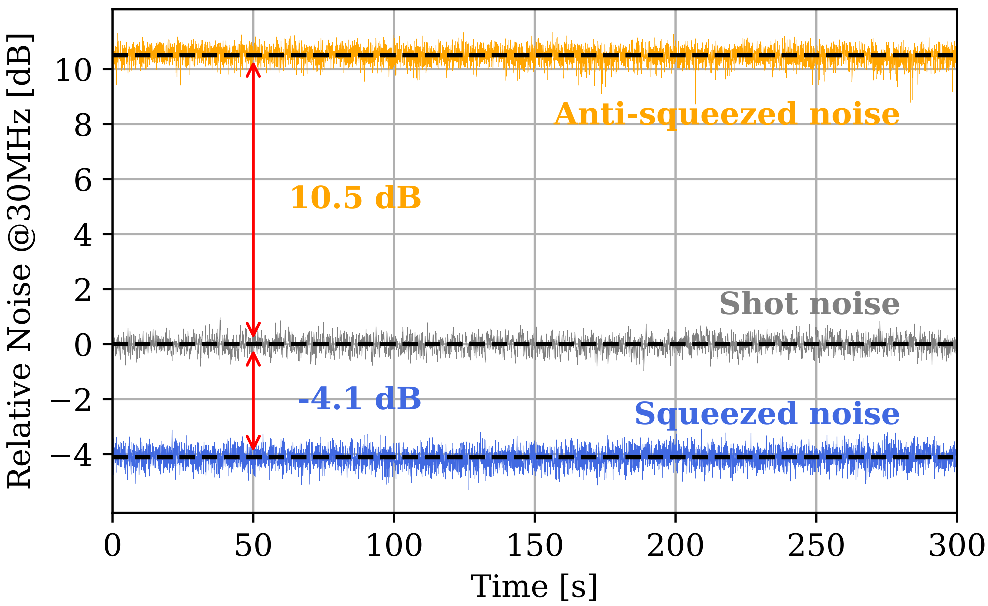

Figure 6.7: Long term measurement over five minutes to test the stability of the lock regarding slow drifts. The measurement shows that several minutes of phase-stability are possible with a noise reduction of 4.1 dB compared to shot noise and a noise amplification of 10.5 dB.

The spectrum measurement in figure 6.8 gives an overview of the bandwidth of the detected sidebands. It reveals a noise suppression over the whole measurement bandwidth from 5 MHz to 1.5 GHz. Until up to 700 MHz, I measured a squeeze level of more than 3 dB, indicated by the dark red line. At 830 MHz the electronic feature of detector 2 is visible. The squeeze level is lower than 2 dB up until a sideband frequency of 1.2 GHz, indicated by the light red line. Above 1.25 GHz the sensitivity of the homodyne detector decreases and the measurement is dominated by dark noise contribution.

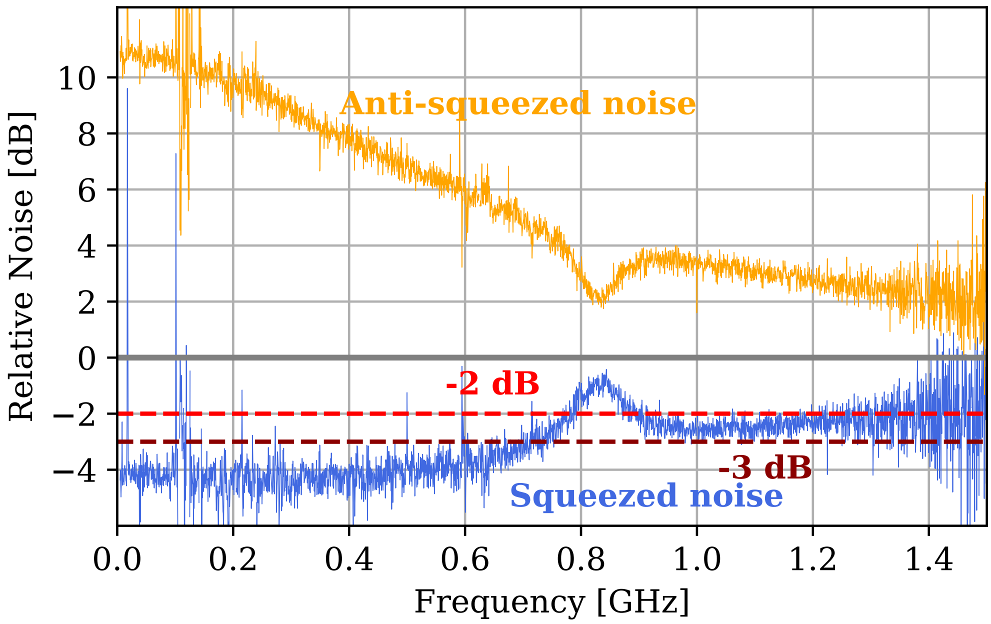

Figure 6.8: Measurement of the spectrum from 5 MHz to 1.5 GHz. I measured more than 3 dB noise reduction up to 700 MHz and more than 2 dB in the GHz range. The bump at 830 MHz is an electronic feature of the balanced homodyne detector. The noise at the end of the spectrum is due to the reduced dark noise clearance of the balanced homodyne detector at higher frequencies.

All measurement results show, that the locking setup is suitable to phase-stabilize squeezed states over a GHz bandwidth that have traveled over 1 km optical fiber, distributed outside of temperature-controlled and quiet laboratories. It is possible to compensate for seismic and acoustic disturbances picked up by the fibers in a noisy environment such as the basement of the ZOQ, where several generators, pumps and cooling devices are located. Slow drifts caused by temperature changes can be compensated for up to a certain amount before the range of the slow actuator becomes too small. In the next section, I present a loss analysis of the setup.

6.3 Phase noise analysis

The spectrum measurement (figure 6.9) of the squeezed light reveals high phase noise dependent losses in the frequencies up to 500 MHz. This cannot be explained by optical losses only but has its origin in extra phase noise as explained in section 2.2.2 and 2.2.3. In the following two sections, I investigate the contributions from different noise sources, including excess phase noise.

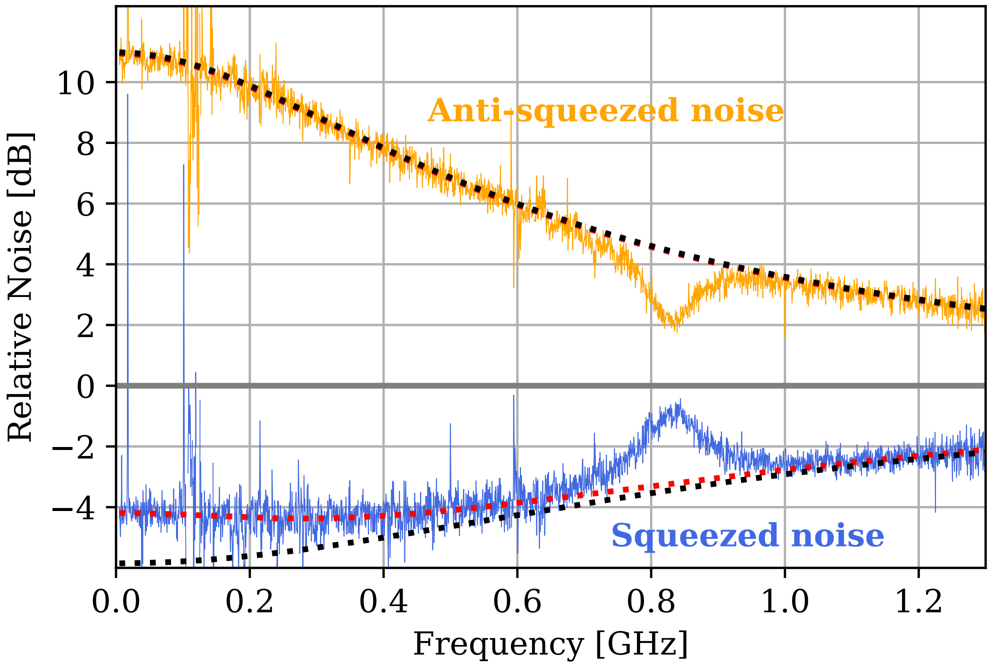

Figure 6.9: The same spectrum as in figure 6.8 but with theoretical fits for optical losses with (red dotted line) and without (black dotted line) extra phase noise. It becomes visible, that the anti-squeeze value is hardly affected, while the squeeze values experience losses up to approximately 500 MHz, most significantly in the lower frequency band.

The phase modulation for the feedback control loop was produced by a fiber EOM of the type MPZ-LN-10 from *exail* having a half-wave voltage of $U_\pi = 4\,\mathrm{V}$. Assuming a linear relation, our peak-to-peak modulation voltage of 200 mV led to $|\pm 4.5°|$ modulation amplitude. This matches well with the calculated and fitted value of $(0.099 \pm 0.012)\,\mathrm{rad} \approx 0.1\,\mathrm{rad} \approx 5.7°$, taking into account that additional sources of phase noise (e.g. acoustics and vibrations in the basement) contributed to the total amount. In figure 6.9 the spectrum can be seen with two theoretical models: the fit from formula (2.57) in black which takes into account the optical losses of the setup but does not include a phase noise term. In red is the fit from equation (2.58) with the same parameters and an additional phase noise term. It is visible, that the measurement results in the frequencies up to 500 MHz are limited mainly by phase noise which leads to a reduction of the maximum achievable squeeze value by 2 dB, compared to the fit without phase noise. The reason why the lower frequencies are more affected than the higher ones can be deduced from equation (2.58) and figure 2.5. The high anti-squeeze values lead to a stronger contribution and thus contamination of the squeezing spectrum. The measured data points are in good agreement with the theory fit, supporting the assumptions regarding the phase noise.

6.4 Optical loss analysis

The losses detected in the measurement results do not originate solely from phase jitter. Other sources such as imperfect mode matchings, quantum efficiency of photodiodes and transmission losses accumulated to $(21 \pm 1.2)\,\%$ losses in total. A large part of the losses are accounted for by coupling into/out of the fiber and the transmission through it. The fiber has a transmission loss of $0.02\,\mathrm{dB/km} \approx 4\,\%$ and the couplers can be estimated to have about 2 % each. The detection stage with high quantum efficiency photodiodes showed losses of 3 %. Typical mode matching values for the beam overlap in Bob's laboratory can be seen in figure 6.10 with a matching of 95 % for the local oscillator and 97 % for the signal path. The resulting losses can be estimated at roughly 7 %. All known loss values add up to 17 % losses. The remaining 4 % can be explained by optical losses and fringe visibility of the homodyne detector, neither of whhich was measured explicitly.

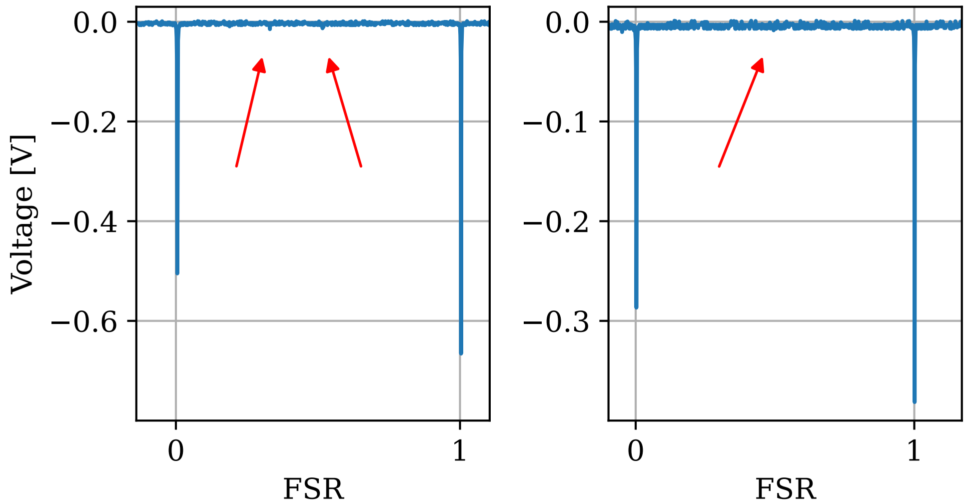

Figure 6.10: Typical mode matchings in the setup. Left: LO on diagnostic mode cleaner (DMC) in Bob's laboratory. Besides the TEM00 mode, two other tiny peaks are visible here. Right: Control beam of the squeezing fiber on the DMC in Bob's laboratory. One extra peak shows up here. The different heights of the TEM00 peaks are due to the non linearity of the piezo mirror. The technique of mode matching using a DMC is explained in section 4.2.

6.5 Discussion and conclusion

To my best knowledge, this has been the first time that phase-stabilized GHz-bandwidth squeezed states have been distributed over this length of optical fiber and measured with a remote local oscillator. I show measurements with a stable read-out quadrature over five minutes and a bandwidth of 1.3 GHz. The phase noise analysis reveals 0.1 rad of excess phase noise, partly induced by the modulation for the quantum noise lock.

However, the analysis of the transfer function in figure 6.3 reveals potential for further optimization. The sharp drop of the amplitude suggests, that the controllers and actuators are not yet perfectly coordinated to each other regarding frequency and gain. The gradient of the phase plot with the rising values above 1 kHz points to elements in the control loop that have a positive impact on the phase. With a better tuning of the PID controllers, more stability and bandwidth can probably be achieved.

The major limitations of the control loop were slow drifts, presumably caused by temperature changes along the fiber channel. The slow actuator was not able to compensate for them, which could be improved by a more capable actuator. A temperature-based actuator might work here, as well as a fiber phase shifter with more range.

Our approach with two fibers instead of one as in [Qin+19] solves the problem with scattering issues and allows for the transmission and measurement with a remote local oscillator. That circumvents the need for extra devices and synchronization at the receiver site, which is the approach in [Sul+22]. The measurement results in this chapter show a successful implementation for squeezed vacuum states. In the next step, the locking scheme is extended to two-mode squeezed states.

CHAPTER 7

Phase-stabilized distribution of two-mode squeezed states over 1 km optical fiber

7.1 Configuration of the quantum noise lock

For measuring correlated results, the read-out quadratures at Alice's and Bob's detectors have to be the same and need to be stabilized to each other. As our entangled state is circular in phase space, it is not possible to generate an error signal directly from the scanned state, because it does not show any extrema (see figure 7.1). I solved this problem through real-time synchronization and subtraction of the states. Subtracting the photo voltages of A and B while rotating one read-out quadrature results in a signal with minima and maxima, which can be used for the locking scheme. The setup for the control loop had to be extended with additional components. The analog and digital additions, as well as the measurements with the lock, are presented in this chapter.

In order to extend the quantum noise lock from squeezed vacuum states to two-mode squeezed states, the following upgrades had to be made in the setup.

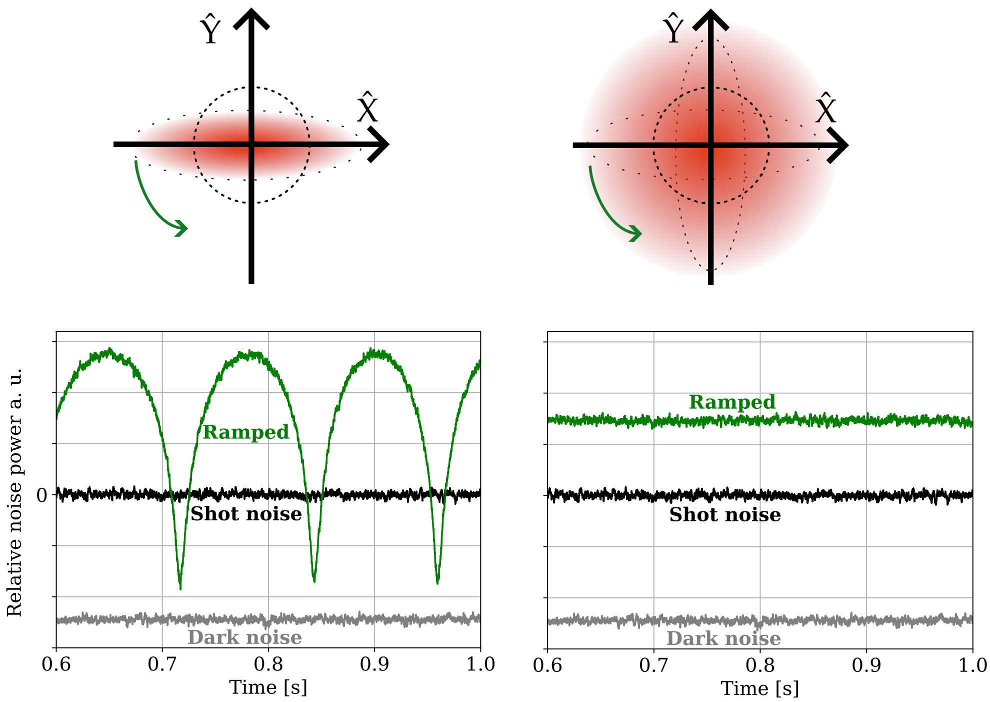

Figure 7.1: Comparison of a scanned squeezed state (left) and a scanned two-mode squeezed state (right). While the rotation of a squeezed state results in a pattern with minima and maxima that is suitable for a quantum noise lock, the entangled state is spherically symmetric. Scanning this state therefore results in a constant output with no possibility to generate an error signal from it.

Coax cables for signal transmission and DAQ synchronization: Two coax cables with a length of 80 m were deployed between the IQP and the ZOQ, one for the synchronization of the two data acquisition cards and one for the signal transmission between the detector of Alice and the detector of Bob.

Frequency splitter: The signal from the balanced homodyne detectors had to be split in the frequency domain. The analog envelope detector from the lock for squeezed vacuum states had a bandwidth of 300 MHz. Since our goal is a QKD setup with a high data rate and the signal for this lock is transmitted by a classical channel, a different solution for the entangled states was necessary. All information transmitted through a classical channel is considered insecure. It is therefore desirable to use the smallest possible bandwidth for the feedback control loop to have as much bandwidth as possible left for the generation of a secret key.

For this reason, the first analog element behind the AC output of each balanced homodyne detector is a frequency splitter with one input and two outputs. The high frequency (HF) output is for the signal that is measured with the data acquisition card and will be used for the secret key. It corresponds to the input signal. The low frequency (LF) output is the signal that is used for the phase lock. It is low-pass filtered by an active Bessel filter with a design cutoff frequency of 90 MHz. This low-pass filter ensures that not the entire bandwidth enters a public channel or the locking electronics. Similarly, the data used for the lock cannot be included in the secret key generation. Applying the transfer function of the frequency splitter to the measurement data during post-processing excludes all information that was transmitted via a classical channel.

The schematic of the frequency splitter can be seen in figure 7.2. I built two of them, one for each detection site, and characterized them by measuring their transfer functions (figure 7.3). The concept with the signal subtraction requires the signals from both homodyne detectors to be as similar as possible. Almost identical frequency splitters are a prerequisite to achieve that goal, which was successfully realized here.

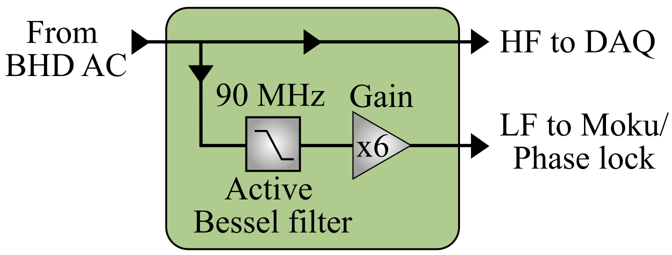

Figure 7.2: Schematic of the frequency splitter. An active Bessel filter with a cutoff frequency of 90 MHz filters the signal that gets into the locking loop. An analog gain amplifies the signal by a factor of six for the analog-digital-converter of the Moku:Pro. The signal for data recording enters the DAQ unfiltered and must be corrected during post-processing.

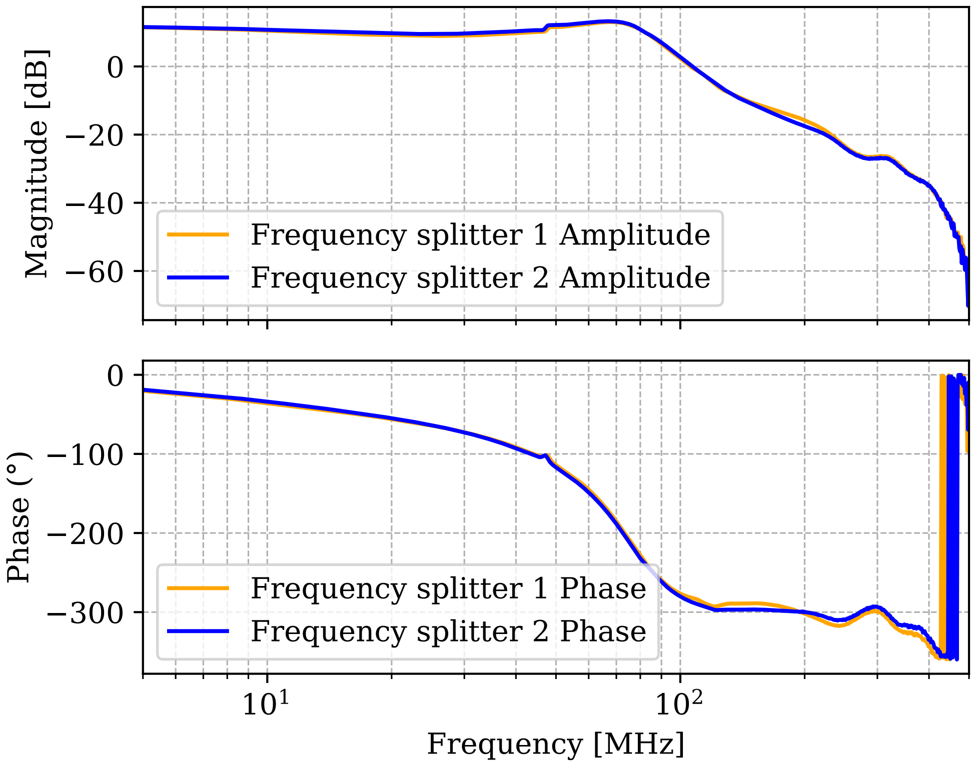

Figure 7.3: The transfer functions of the two frequency splitters from 5 MHz to 500 MHz. They were successfully built to be as identical as possible. Minor differences are due to tolerances in the components used. The cutoff frequency was designed to be at about 90 MHz.

Analog gain factor: Additionally, the amplitude of the signal used for the lock had to be increased from some mV to several tenths of mV in order to be high enough for the analog-digital-converter (ADC) of the Moku:Pro. The signal was amplified with a gain factor of six in Bob's lab and a factor of approximately 30 in Alice's lab. The amplifier OPA657 used for the gain factor of six is on the same PCB as the frequency splitter, as shown in figure 7.2. The balanced homodyne detector of Bob provided a larger amplitude, so the factor of 6 was sufficient here, while the detector of Alice needed extra amplification. After that, the signal was processed by the analog-digital-converter of the Moku:Pro and the following changes were implemented digitally.

Digital gain: Since the two balanced homodyne detectors used for measurements are slightly different, the shape and amplitude of their vacuum noise levels were different and had to be corrected for the next step, the subtraction. With a digital gain stage, the shot noise levels of the two signals were fine tuned to the same order of magnitude. A frequency dependent gain would have been optimal here, however, it is much harder to implement and it turned out that a generic gain for the whole bandwidth worked for this purpose.

Digital delay line: The signals that had to be subtracted from each other had different travel times until they both arrived at the analog-digital-converter for the lock. Although the speed of light in a fused silica fiber is approximately the same as the speed of an electronic signal in a copper wire, a difference arises because the fiber has a length of 1 km and the cable approximately 80 m. This leads to a delay of about 4.5 µs that had to be compensated for in real-time. The delay line was realized digitally which had the advantage that it could be adjusted over a large range. Analog solutions also exist, however, they do not provide sufficient delay and are not as as easily tunable as digital ones.

Digital subtraction: In order to get a signal with minima and maxima, I subtracted two correlated states while rotating the read-out quadrature in Bob's lab. This leads to a minimum when the quadratures at Alice's and Bob's detectors were identical and the subtracted values were roughly the same. In the opposite case, with the read-out quadratures being 180° apart from each other, the results were anti-correlated which gave a maximum (see figure 7.4 for a graphical description) when subtracted.

Digital envelope detector: The analog envelope detector used a bandwidth from 8 to 300 MHz, which cannot be used for the secret key as explained in section 7.1. Tests with a smaller bandwidth e.g. from 7 to 35 MHz, showed that the output signal became too noisy and locking was impossible. The envelope detector was therefore realized as a digital component on the Moku:Pro, providing more options to finetune the implementation and improve the signal-to-noise ratio.

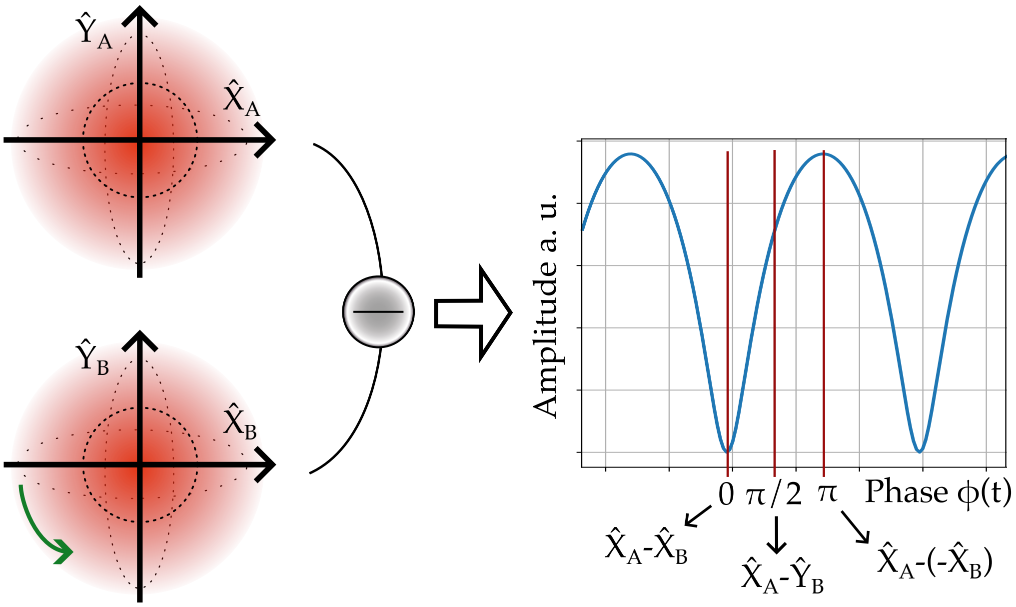

Figure 7.4: Due to the property of entanglement, a pattern with minima and maxima can be produced by rotating one read-out quadrature while leaving the other one unchanged and subtracting the results from each other. The minimum is reached at the same read-out quadratures because the measured values are almost identical. With a 180° phase shift between the read-out quadratures, we measure anti-correlated states and the maximum is reached. In between, the read-out quadratures have a 90° phase shift and the results are therefore uncorrelated.

All four digital elements described above were implemented using the Moku cloud compile service. The codes were written by Stephan Grebien and Christian Darsow-Fromm and partly modified by me.

The rest of the lock (modulation and demodulation, fast and slow controllers) contained the same components with similar settings as the setup for the single-mode squeezed vacuum states (chapter 6). The integrator cutoff frequencies were slightly different and I did not use the fiber phase shifter for the Hertz and sub-Hertz region here, because I was limited by the hardware of the Moku:Pro. It provides four multi-instrument slots and four analog inputs and outputs. With the additions made to the setup, all of them were occupied and neither the PID controller nor the fiber phase shifter itself could be implemented or connected.

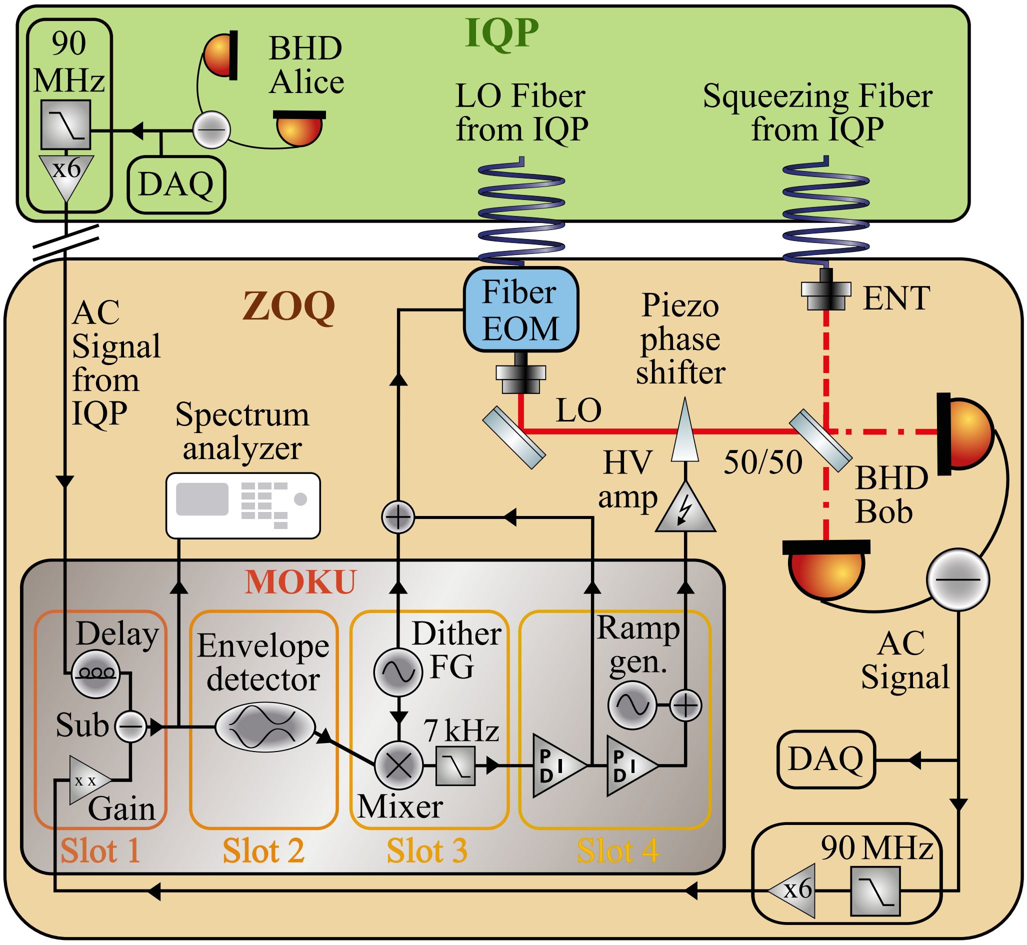

Figure 7.5: Schematics of the control loop for two-mode squeezed states. The AC signals from both balanced homodyne detectors are low-pass filtered and amplified. In the ZOQ, they are combined and subtracted from each other, before being guided into the quantum noise lock implementation as described in section 3.2. The control loop is realized with a Moku:Pro, including the digital envelope detector, modulation frequency generator and ramp signal. The only analog devices are the frequency splitter and the amplifier. The measurements are recorded by data acquisition cards, synchronized by an extra cable (not in the picture). The spectrum analyzer was used to get instant feedback from the different signals and the performance of the lock.

In contrast to the setup for squeezed states, I used the internal frequency generator of the Moku:Pro to generate the modulation and demodulation signal. The external one used in the previous chapter revealed a high noise floor and was substituted. The complete electronic setup can be seen in figure 7.5.

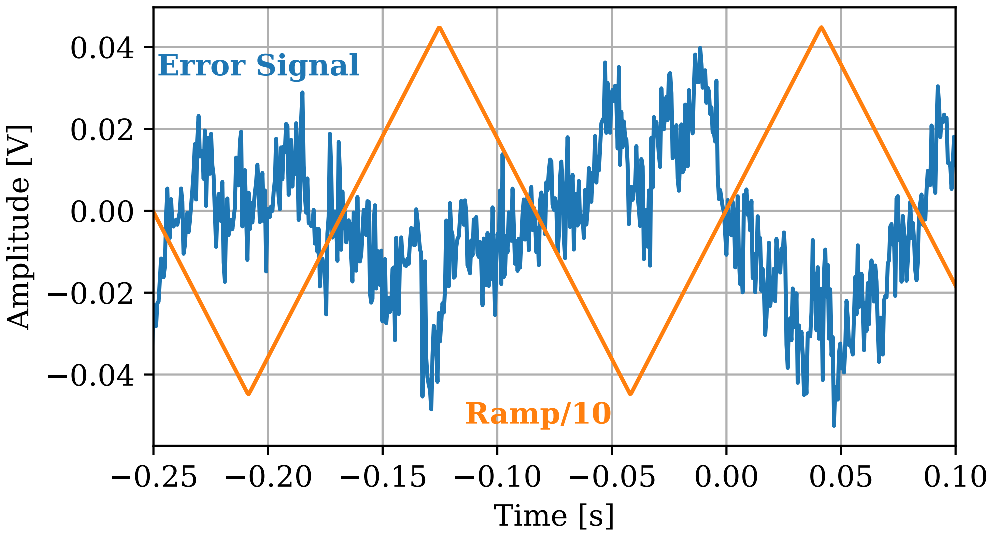

Figure 7.6: Error signal (blue) for the entanglement phase control loop, measured in Bob's laboratory. In orange, the phase scan is shown, with the amplitude divided by 10 to provide a useful scaling of the error signal. A low signal-to-noise ratio is apparent.

In figure 7.6, the error signal is shown, measured in Bob's lab, plotted together with the monitor output of the scanning signal. Although it is very noisy with a maximum peak-to-peak amplitude of 80 mV, it was sufficient for locking purposes.

The implementation of the feedback control loop enables the stabilization of the read-out quadratures from two different balanced homodyne detectors to be the same. The system can be stabilized either to correlated or anti-correlated values, depending on the chosen zero crossing. It is not possible to choose a specific quadrature or measure orthogonal quadratures with it. An absolute phase reference would be required for that, which is not part of the setup.

7.2 Measurement results

In order to show correlations between two entangled states, the measurement results from both corresponding balanced homodyne detectors have to be subtracted. In this work, I did not subtract the entire bandwidth of the entangled states in real-time, but only the bandwidth required for the feedback control loop. This reduced the bandwidth for the real-time process from 1.3 GHz to about 120 MHz and less demanding hardware could be used. The signals for the measurement data from the two balanced homodyne detectors were recorded with two high speed data acquisition cards (DAQs), one in Alice's lab and one in Bob's lab. They are of the same type and have a sampling rate of up to 5 GHz.

7.2.1 Measurement results without fiber distribution

In order to test components and instruments implemented on the Moku:Pro, I set up the entanglement lock in the IQP and measured two-mode squeezed states in Alice's lab only, with two balanced homodyne detectors (see figure 7.7). This had the advantage of fewer disturbances because no fibers were involved. The locking setup was reduced to only one PID controller and phase actuator, a piezo mounted mirror in the local oscillator beam path from $\mathrm{BHD_B}$. One data acquisition card with two inputs for both detectors was used, with a sampling rate of 2.5 GHz, which is the maximum when used in dual channel mode.

For the measurement, I tuned both squeezed light cavities to their resonances and locked the relative phase between the two squeezed states to 90° using the feedback control loop described in section 3.1.2. It was designed and set up by Benedict Tohermes (see [Toh25] for more details). I also ensured that the anti-squeeze values of both squeezers were the same to produce symmetric entangled states, which are sent to the two balanced homodyne detectors.

To generate an error signal, the read-out quadrature of one homodyne detector was scanned, while the other one was free floating (graphical description in figure 7.4). It can be assumed that the free floating read-out quadrature had no or negligible changes in phase during a measurement as discussed in [Toh25]. With the laser lock box provided by the Moku:Pro, the two read-out quadratures can either be locked to be the same (correlation) or to be 180° apart from each other (anti-correlation) by choosing the corresponding zero crossing of the error signal. I want to point out here that it is the same quadrature in both cases, which differs from single-mode squeezed states. For single-mode squeezed states, the change of the zero crossing from minimum (squeezing) to maximum (anti-squeezing) results in a change between the X and the Y quadrature, which corresponds to a 90° phase shift. By changing the lock point here, I switched between the sum and the difference of the same quadrature, which corresponds to a 180° phase shift.

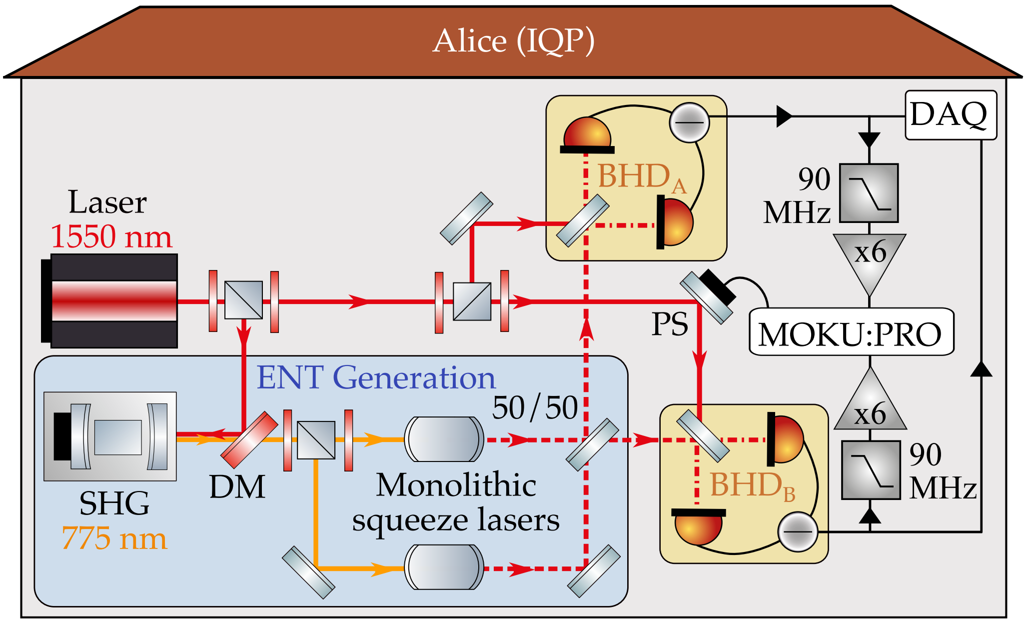

Figure 7.7: To test the locking concept the measurement was performed in Alice's laboratory only with no fiber transmission to Bob, as this reduced the complexity. Two balanced homodyne detectors were set up in the laboratory, one with a phase shifter in the LO path which was used for the phase control loop.

For each measurement run, I took three different traces with each balanced homodyne detector: the signal, the shot noise and the dark noise. The data were analyzed with Python code written by Benedict Tohermes. For the zero span measurements, the signal and shot noise data were filtered at 62 MHz with a filter bandwidth of ±2 MHz. Afterwards the filtered signal data was normalized to the corresponding filtered shot noise data. Sum and differences were calculated to get the correlated and anti-correlated values. It turned out that the path that went through the digital delay line experienced a delay of six clock cycles, even though the delay was set to be zero. I compensated for that in the post processing. The zero span measurement result (figure 7.8) proves that the lock worked and the read-out quadratures from both homodyne detectors are the same. The orange and blue traces represent the subtraction and addition of the data, remaining stable for the duration of the measurement. The two gray traces correspond to the noise powers of each detector. Their levels are identical, indicating, that the initial entangled state is spherically symmetric at the analyzed frequency. The result shows correlated noise of more than 4 dB below and anti-correlated noise of about 6.5 dB above the combined shot noise. From these values, a violation of the Duan and EPR-Reid criterion (see section 2.3.2) can be inferred.

From the same data set, I chose a subset and plotted a spectrum, which can be seen in figure 7.9. The signal traces had to be normalized again to their corresponding shot noise values, which were frequency dependent as the detectors don't show a flat noise floor. This was done by cutting the subset in different blocks, calculating the fast Fourier transform (FFT) for signal and shot noise for each block and normalizing the signal to the mean of the shot noise FFTs. Afterwards, I added and subtracted the results and plotted it in relation to the combined shot noise. I also compensated for the delay that occurred in the higher frequency range above 1 GHz due to electronic features. The results show correlation and anti-correlation over the whole bandwidth of 1.25 GHz. A higher bandwidth was not possible due to the sampling rate of 2.5 GHz. The dips and bumps from the homodyne detectors (see figure 5.3 and 5.4) at 830 MHz and roughly 1 GHz are visible here as well.

Both results prove the feasibility and suitability of the locking concept for a phase stabilization of the read-out quadratures for measuring two-mode squeezed states. Moreover, the functionality of the self-built and self-programmed parts of the setup could be tested and verified to work in a temperature stabilized laboratory. In particular the question of whether a small operating bandwidth of 90 MHz is sufficient for the digital envelope detector could be analyzed with a positive outcome. In the next step, the feedback control loop was used to stabilize the read-out phases of two-mode

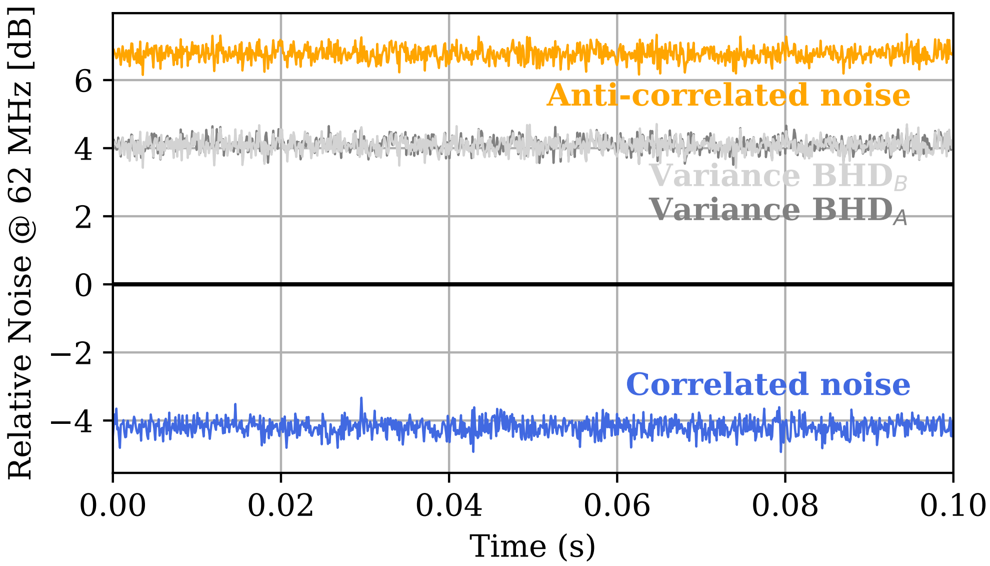

Figure 7.8: Zero span measurement at 62 MHz of the results measured without fiber transmission in the lab of Alice, filtered with ±2 MHz bandwidth. Blue are the correlated values, orange the anti-correlated values and gray/dark gray are the traces from the two balanced homodyne detectors. The measurement shows that the lock is stable over the measurement time and the read-out quadratures are the same. The identical noise level of the gray traces point to two symmetrical entangled states.

squeezed states between two buildings, with half of the states traveling through 1 km of fiber.

7.2.2 Measurement results after 1 km fiber distribution

In this subsection, I show measurement results measured in the laboratories of Alice and Bob simultaneously after 1 km of fiber transmission with the read-out quadratures stabilized to each other, so they are the same with respect to the entangled states. The setup of the control loop is shown in figure 7.5 and the schematic of the implementation is depicted in figure 7.10. Compared to the previous section, the complexity here is higher due to the separated laboratories and the environmental influences that disturb

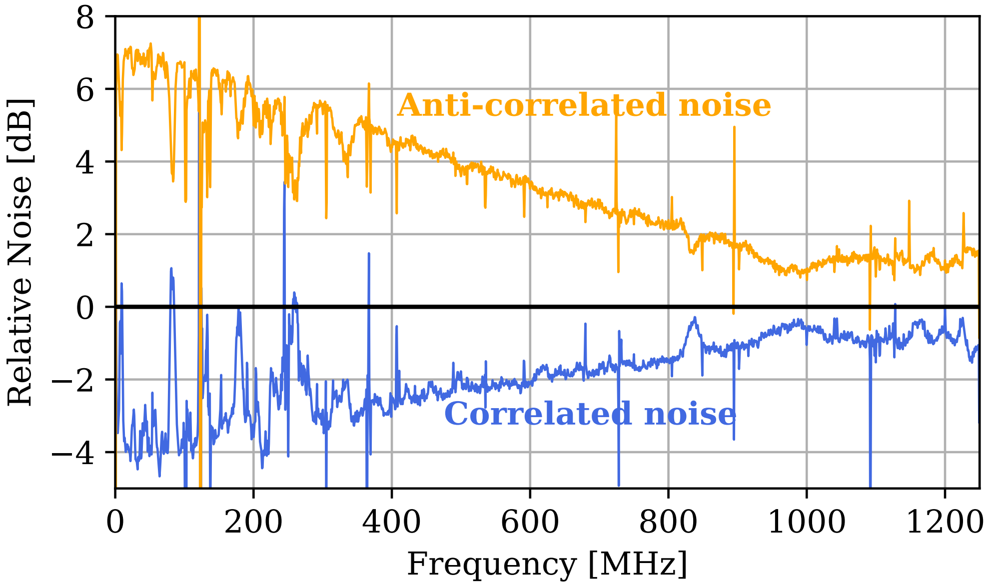

Figure 7.9: Spectrum plot of the results measured in Alice's laboratory without fiber transmission. Blue are the correlated values and orange the anti-correlated values. The measurement shows (anti-)correlation over the whole measurement bandwidth, which was limited by the sampling rate of the DAQ to 1.25 GHz.

the quantum states. The DAQs, which are connected for synchronization purposes by an 80 m long extra cable described in section 7.1, were now used in the single channel mode, using the full 5 GHz sampling rate.

Before each measurement run, both fiber outputs in Bob's lab were tuned with the polarization control to be s-polarized by sending a bright light field from Alice through the fibers. The measurement procedure then was similar to the one in the previous section. The squeeze lasers were tuned to be on resonance, producing the same anti-squeeze level and the phase of the squeezed states was locked to 90° relative to each other. In the ZOQ, both cables from both balanced homodyne detectors were connected to the Moku:Pro. I tuned the digital delay until the signals showed correlated values. This was the case for a delay of (1393 ± 2) clock cycles, corresponding to a delay of 4.45 µs. I also adjusted the digital gain to align the magnitude of the two shot noise levels. To get a feedback on these processes the signals

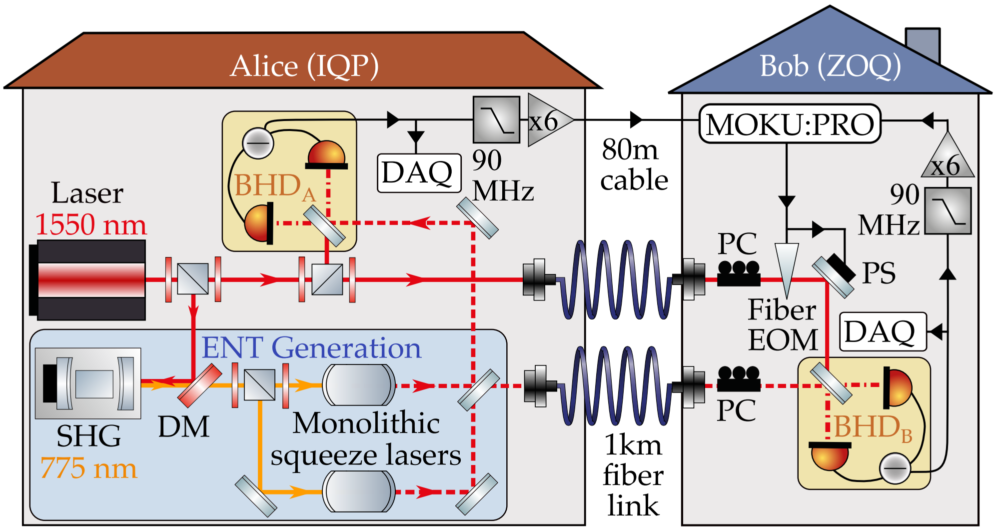

Figure 7.10: The states are generated and split in Alice's lab. Half of the states is transmitted through the fibers to the lab of Bob, where a second measurement station and the control loop for the phase lock is located. Two cables of about 80 m length transmit the AC signal from Alice and the synchronization signal for the DAQ to Bob's lab.

were monitored on a spectrum analyzer. By scanning the phase of Bob's local oscillator, an error signal was generated (see figure 7.6), which could be fine tuned with the gain and the offset buttons of the Moku:Pro until it was symmetrical enough to start the lock.

To record a measurement, a trigger had to be sent to both DAQs at once in order to start the data acquisition simultaneously in both laboratories. This was previously done using a frequency generator in Alice's lab, connected to both DAQs, which required an additional 80 m cable to Bob's lab. I switched to a software-based trigger which caused some unknown delay between the two trigger set points but as the constant delay between both DAQs had to be analyzed and compensated for anyways, this added no complexity but prevented the need for a third cable. The data analysis was done mainly with the same code described in the previous section with two additions: First, the compensation for the constant delay, consisting of the contributions from the software based-trigger and the different travel times of the light in the fiber and the signal in the cable. Second, the compensation for the effect that the DAQs were not fully synchronized and with increasing measurement time their clocks diverged, which affected the strength of the correlation of the two-mode squeezed states.

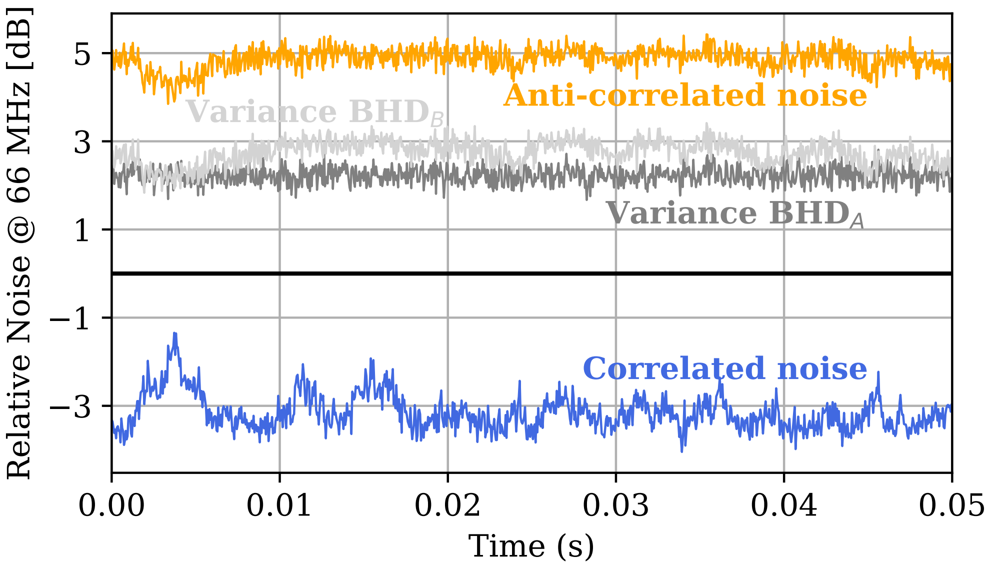

Figure 7.11: Zero span measurement at 66 MHz of phase stabilized two-mode squeezed states after 1 km fiber transmission with 5 MHz filter bandwidth. A suppression of roughly 3 dB below and an increase of 5 dB above the combined shot noise are visible and stable, albeit noisy. The gray traces are the detector traces of Alice (darkgray) and Bob (gray). Bob's trace is the one that is actuated to establish the synchronization with Alice's trace, which remains flat and not noise-free in this measurement.

The result for the zero span measurement can be seen in figure 7.11. It confirms that the lock works. The quadratures are aligned to each other and subtraction/addition of the values leads to correlations below the combined shot noise of about 3 dB and to anti-correlations above the combined shot noise of about 5 dB. The values are lower than those measured in the IQP only because the transfer to another lab induced additional losses due to fiber coupling and transmission. It is also clearly visible that the traces contain more noise than in the IQP measurement and the lock can not suppress it completely. This could be due to several reasons. On the one hand, the noisy error signal (figure 7.6) already indicates that the control loop suffered from a poor signal-to-noise ratio. It is possible, that the amplitude

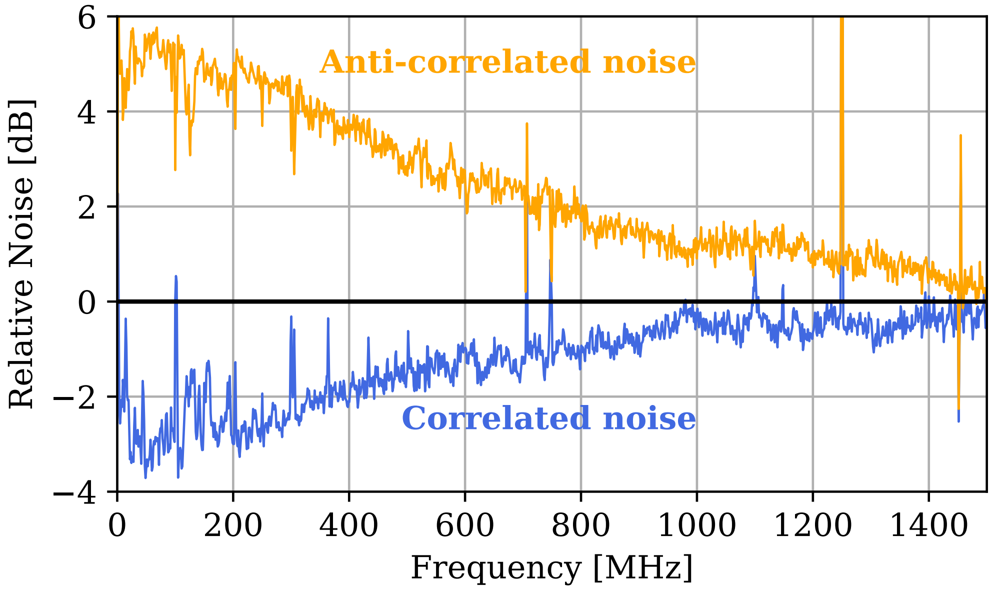

Figure 7.12: Frequency analysis of phase-stabilized two-mode squeezed states after 1 km fiber transmission. The spectrum shows correlations and anti-correlations until up to 1.5 GHz. There are less noise peaks at lower frequencies compared to the measurement in the IQP, the overall level decreases faster than expected though.

of the initial signal (the difference between the subtracted and the added states) is too low for the envelope detector to transform it into a clean signal. Also the signal transmission from Alice's lab using a standard BNC cable instead of differential signal transmission is not optimal. Differences in the ground levels of the two buildings could have led to disturbing influences. Additional filters were necessary in the lab of Bob to prevent some low frequency disturbances from coupling into the locking loop. These might have caused extra delay or phase shifts in the control loop, affecting the overall stability and response time.

The spectrum measurement in figure 7.12 shows correlations and anti-correlations up to 1.5 GHz, where the measurement is limited by the sensitivity of the balanced homodyne detectors. The values are lower than in the IQP measurement, and the slope also differs slightly, as it seems to bend slightly towards the shot noise trace. There are fewer noise peaks in the frequency band from 5-400 MHz which could be due to the fact that I used a different detector (the detector in Bob's lab instead of the second detector in Alice's lab) with a different dark noise behavior. The first 100 MHz show decreasing values, which might be due to the phase noise induced by the modulation frequency for the lock.

The results lead to the conclusion that both the general concept and the individual components are suitable to control and align the read-out phases between Alice's and Bob's measurement stations. Even with rather small initial squeeze and anti-squeeze values and a high noise floor due to the fiber link and electronic noise, it was possible to configure the control loop such that these measurement outcomes were possible.

7.2.3 Asymmetric rotation measurement

In this subsection, I present another measurement result from the IQP laboratory only. No fiber transmission was involved. I tuned the two squeezing cavities such that they produce different amounts of anti-squeezing (see figure 7.13). The resulting entangled states are therefore elliptical and not invariant under a phase rotation. The angle θ between the two squeezed states is locked to 90° using phase shifter 1 in the pump path (compare with figure 7.13).

The read-out quadratures of the two homodyne detectors are aligned and stabilized to be the same with the locking scheme described in the previous sections, using the phase shifter 3 in the local oscillator path from detector BHD_B.

With phase shifter 2 in the pump path of the second squeeze laser, the squeezed states were constantly rotated (angle Ψ). As the two squeezed states are phase-stabilized to each other, this led to a rotation of both entangled states. Also the balanced homodyne detectors were stabilized to measure in the same quadrature. Consequently, a zero span measurement of the entire state could be performed instead of measuring only one quadrature. The rotation Ψ was generated by an external frequency generator with an amplitude of 2 V for modulation depth. This was sufficient to achieve a rotation of the states without affecting the locks. For the rotation frequency, I chose 10 Hz, leading to a 180° rotation of the entanglement ellipse within the measurement time of 100 ms, which is enough to measure both, the X and the Y quadratures.

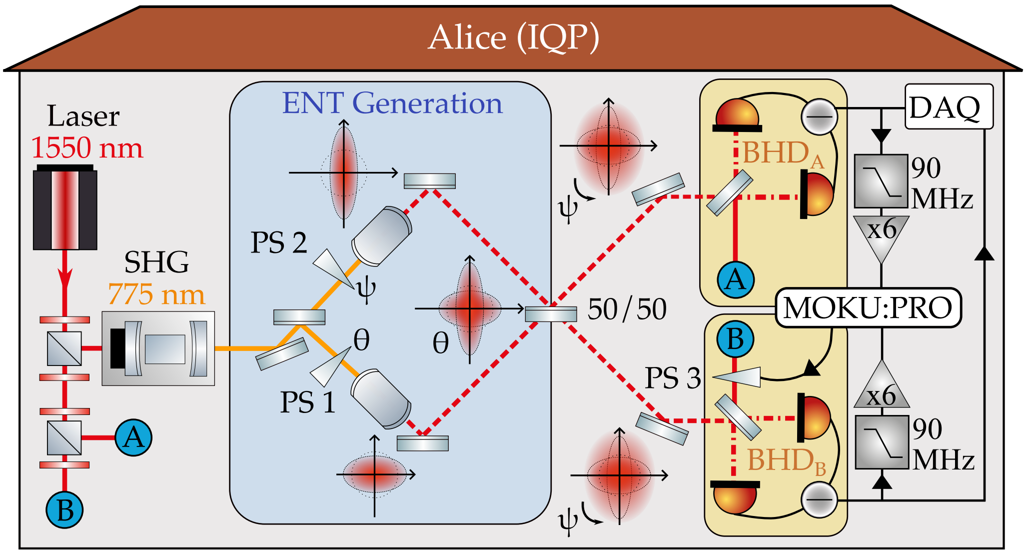

Figure 7.13: Setup to look at both quadratures in one measurement. The two squeeze lasers produce squeezed states of different strengths for an elliptical entangled state. The squeezed states were locked to 90° relative to each other (angle θ, PS 1). The read-out quadratures were locked so that they are the same, using the phase shifter 3 (PS 3). With phase shifter 2 (PS 2) in one of the pump paths, the entangled states were rotated by angle Ψ.

The measurement result is shown in figure 7.14. It is a zero span measurement, analyzed at 15 MHz. The sum and difference traces (orange and blue) show minima and maxima which is due to the fact that the initial squeeze values are not identical and the different squeeze and anti-squeeze levels are reconstructed. The two gray traces are the variances of the two detectors. As the entangled states had an elliptical shape, their minimum and maximum values represent the long and the short axis of the ellipses. However, they slightly drift apart from each other during the measurement time. This strongly suggests that the read-out phase lock is unable to follow fast enough. Two minima and one maximum are visible, proving that a 180° rotation was performed. The relatively sharp peak of the second maximum most likely originates from the turning point of the piezo mirror.

The measurement can successfully demonstrate two things. First, correlation and anti-correlation can be observed independently of the phase angle

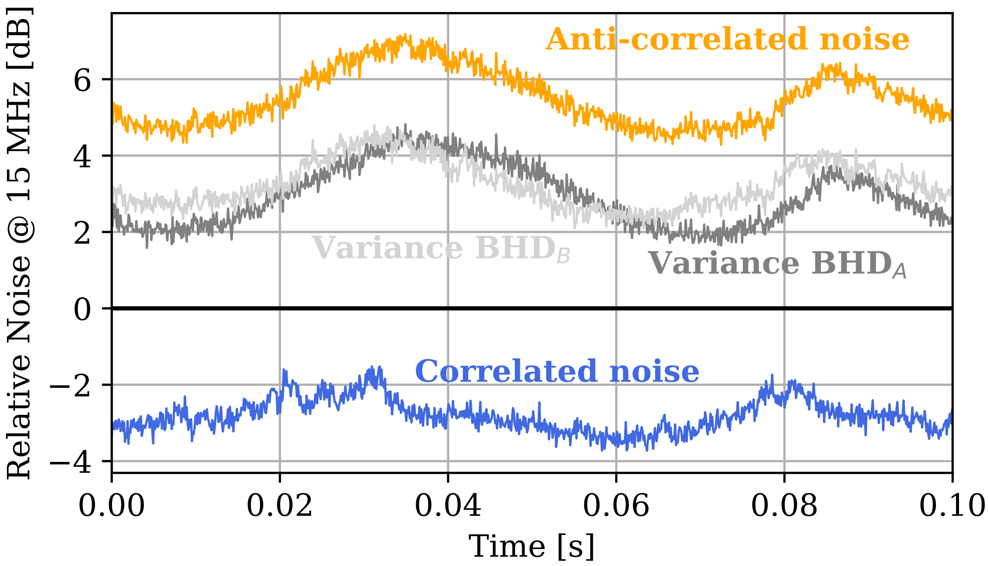

Figure 7.14: Zero span measurement at 15 MHz with elliptical entangled states that were rotated at 10 Hz during the measurement. All traces show corresponding minima and maxima. From the gray detector traces, it is visible that they are not perfectly aligned with each other. Nevertheless, correlations and anti-correlations can be observed over approximately 200° of rotation. The sharp peak of the second maximum indicates the turning point of the piezo mirror.

between the entangled states and the read-out coordinate system. Second, in this measurement, the sum and difference of both quadratures can be seen. While the previous measurements investigated the sum and difference of one quadrature only, both quadratures are measured and analyzed in this setup.

7.3 Discussion and conclusion

In this section I presented the measurement results from two locally separated balanced homodyne detectors that measured two-mode squeezed states with aligned and stabilized read-out quadratures. The results show that the general concept and method of a quantum noise lock work very well for this use case. Even in an implementation outside of a temperature- and seismic isolated laboratory and with comparably low squeeze values, it is possible to stabilize the read-out quadratures to each other.

Besides the proof of principle for the feedback control loop, the measurement results in this chapter for distributed entangled states show a possible violation of the EPR-Reid criterion (see section 2.3.2), which is a prerequisite for the one-sided device-independent QKD protocol in [Fur+12]. However, a direct proof of the violation requires measurement pairs of (X_A, X_B) and (Y_B, Y_A) as discussed in 2.3.2 which, in the absence of absolute phase information, is not possible with this setup. Previous work [Rei89; Ast+16; Geh+15] discussed, that for symmetric two-mode squeezed states, the squeeze and anti-squeeze values in the orthogonal quadrature can be assumed to be the same. This is also confirmed by the rotation measurement I presented in subsection 7.2.3, where the differing values for the correlated and anti-correlated states arise from the different initial squeeze factors. With improved squeeze lasers as discussed in the next chapter, the EPR bandwidth can be further extended.

The signal transmission with a single copper wire worked in principle, although it is questionable whether this would be the case for longer distances or buildings with higher differences in the ground potential. In general, many components could be improved for higher stability and long-term usage. Details are discussed in the next chapter. The simultaneous recording of the data with the DAQs triggered by a software-based signal introduced some extra delay between the two data sets but this could be corrected for in the post processing, which means that this was a successful approach as well. The results prove the feasibility of a fiber-based QKD scheme, based on squeezed light, as it removes the last open technical and design barriers.

CHAPTER 8

Outlook and Conclusion

8.1 Optimization ideas for the current setup

Starting at the heart of the setup, it would be advantageous to replace the squeeze lasers with squeeze lasers that are easier to handle and which produce a higher squeeze factor. Ideally, a threshold of 3 dB over the whole measurement range should be reached ideally with the next generation of squeeze lasers. For this reason, I would suggest using high-bandwidth hemilithic cavities with an anti-resonance coating for UV light. Although the monolithic cavities were very stable once they produced squeezed light, the hemilithic design with a piezo driven lock for the cavity length should be as stable and easier to operate in everyday lab work, especially when tuning the temperature for resonance. With the current design, this was time consuming and could take up to two hours. Another advantage of hemilithic cavities would be having two independent tuning parameters (piezo and temperature) for two degrees of freedom (cavity length and phase matching temperature) instead of using temperature for both. As we discovered, the reproducibility of important technical characteristics of the monolithic crystals is not very high. We tested three crystals and found that they all showed different performance regarding the phase matching temperature, threshold power and achievable squeeze factors. Only one out of three generated more than 6 dB of squeezed light. For the generation of symmetrical two-mode squeezed states, the entanglement is limited by the squeeze laser with the worst performance, and two reliable, robust sources are key to high correlations.

The second major improvement applies to the locking signal that is sent from Alice homodyne detector to Bob's laboratory for the phase lock of the read-out quadratures of entangled states. It might be that the ground potential of two buildings are slightly different from each other. A cable connecting those different ground potentials will collect disturbances which results in a decreasing signal-to-noise ratio (this can be seen in the error signal in figure 7.6). There are two possibilities to circumvent this problem: Differential signal transmission on the one hand or optocoupler on the other hand. Also a combination of both is possible. With differential signal transmission, the signal is transmitted using two signal conductors instead of one, with one being the reference. Disturbing signals act equally on both conductors and can be eliminated by taking the difference at the receiver side. To the best of my knowledge, limitations to the bandwidth or distance for using this method are not relevant for the application considered here. It is widely used for example in the telecommunication network and in acoustic applications (e.g. sound studios). Optocouplers transform an electrical signal into an optical signal and back and therefore allow for a signal transmission between two galvanically separated circuits. They are used in certain components of PCs and in some sound systems like the MIDI standard. For buildings separated even further than the ones in this thesis, this aspect becomes more relevant as the ground potentials tend to be different to each other and can fluctuate when switching on or off devices with heavy loads, like an air-conditioning system. A decoupling of the stabilization loop of a communication system is highly desirable.

To improve the phase lock used for the results presented in 6 and 7, it would be useful to digitize the setup even further. Remote control and more flexible components can save time during setup and give the opportunity to react to changing noise levels and frequencies. The feedback loop was currently limited by very slow drifts, probably caused by temperature changes along the deployed fibers. These could not be completely compensated for by the slow actuator implemented for exactly this issue as the shifting range was not large enough. A temperature based actuator would probably solve this issue, and improve the long-term stability of the lock even further.

8.2 Extension to 5 km fiber length

As estimated in [Geh+15], the protocol would allow up to 5 km fiber length before the losses dominate the setup and make osdiQKD impossible. Here, I outline the changes to the setup that need to be made to extend the optical fiber to 5 km between the EPR source and the remote measurement station.

Besides the remarks from the previous section, one of the most important changes would be the implementation of new fibers with a length of 5 km. The default option would be simply a longer fiber of the same kind as the existing ones. They have the lowest possible losses that silica fibers can have at the current state of the art. Depending on research and availability, it might be worth looking for hollow-core fibers. As described in 2.7, they have even lower losses, but at the time this thesis was written, it was not possible to buy 5 km of them. With a greater distance, active control of the polarization would be beneficial. PM-fibers are still very expensive and have the best performance in an environment with low disturbances, which is not the case with a 5 km deployed fiber length. The chance, that the polarization drifts is high, whether with PM or non-PM fibers and an active, digital control of the polarization, which can be accessed from both laboratories is indispensable for long-term measurements. Additionally, the passive suppression of noise can be improved by deploying the two fibers closer together to increase the common mode rejection.

With 5 km fiber length, it is also necessary to have two cables with a length of 5 km, one for the synchronization of the DAQs and one for the AC signal from Alice's lab (see 7 for a detailed description of the setup). While the synchronization does not require any special cable as it contains no high frequencies, the AC signal for the lock is currently designed with a bandwidth of up to 100 MHz. We used a standard RG-58 coax cable for both purposes, but the signal-to-noise ratio might be too low for the AC signal if the length is extended to 5 km. The RG-58 has an attenuation of 0.139 dB/m. This worked for the 80 m used in my work, but with 5 km it might be necessary to have a cable with a lower attenuation, for example the ecoflex 15 with an attenuation of 0.028 dB/m or the ecoflex 10 with 0.038 dB/m [Koa]. However, the price scales inversely to the attenuation.

8.3 Conclusion

The demand for secure communication is as high as it was more than 2000 years ago. The requirements have changed, however, and more sophisticated methods are needed than just shifting the alphabet by a certain amount of digits. The recent development of novel quantum technologies has opened up new possibilities for realizing secure communications with mathematically unbreakable protocols.

This thesis presents the first phase-stabilized fiber distribution of single-mode squeezed and two-mode squeezed states with GHz bandwidth over a total distance of 1 km. I measured a stabilized noise reduction of 4.7 dB at a sideband frequency of 30 MHz and more than 2 dB above 1 GHz. I demonstrated a stable operation for five minutes, limited by slow thermal drifts. Correlated values showed stabilized noise reduction of up to 4 dB when measured locally in Alice's lab and approximately 3 dB when measured in the remote laboratory of Bob. I implemented two feedback control loops, targeting the problems that arise when transitioning an experiment from a laboratory environment to the real world: outer influences and disturbances causing the measurements to become noisy. My results show, that they can be counteracted and a QKD link based on two-mode squeezed light is ready for user-based implementation, increasing the number of options for secure communication.

I also investigated the long-term performance of monolithic squeeze lasers with GHz bandwidth. Although I could not observe degradation due to gray tracking or other effects, their further use in a QKD setup is debatable. Despite their stable operation once they produced squeezed light, they had several disadvantages compared to hemilithic cavities.

107

Bibliography

[Aba+11] J. Abadie, B. P. Abbott, R. Abbott, T. D. Abbott, et al. "A Gravitational Wave Observatory Operating beyond the Quantum Shot-Noise Limit". *Nature Physics* 7.12 (2011). DOI: 10.1038/nphys2083.

[Abr+00] A. Abramovici and J. Chapsky. *Feedback Control Systems: A Fast-Track Guide for Scientists and Engineers*. Kluwer Academic Publishers, 2000.

[Ace+19] F. Acernese, M. Agathos, L. Aiello, A. Allocca, et al. "Increasing the Astrophysical Reach of the Advanced Virgo Detector via the Application of Squeezed Vacuum States of Light". *Physical Review Letters* 123.23 (2019). DOI: 10.1103/PhysRevLett.123.231108.

[And+16] U. L. Andersen, T. Gehring, C. Marquardt, and G. Leuchs. "30 Years of Squeezed Light Generation". *Physica Scripta* 91.5 (2016). DOI: 10.1088/0031-8949/91/5/053001.

[Ast+13] S. Ast, M. Mehmet, and R. Schnabel. "High-Bandwidth Squeezed Light at 1550 nm from a Compact Monolithic PPKTP Cavity". *Optics Express* 21.11 (2013). DOI: 10.1364/OE.21.013572.

[Ast+16] S. Ast, M. Ast, M. Mehmet, and R. Schnabel. "Gaussian Entanglement Distribution with Gigahertz Bandwidth". *Optics Letters* 41.21 (2016). DOI: 10.1364/OL.41.005094.

[Ast15] S. Ast. *New Approaches in Squeezed Light Generation*. Ph.D. Thesis. Universität Hamburg, 2015.

[Bac+19] H.-A. Bachor and T. C. Ralph. *A Guide to Experiments in Quantum Optics*. 3rd ed. Wiley-VCH, 2019.

[Bec05] J. Bechhoefer. "Feedback for Physicists: A Tutorial Essay on Control". *Reviews of Modern Physics* 77.3 (2005). DOI: 10.1103/RevModPhys.77.783.

[Bel64] J. S. Bell. "On the Einstein Podolsky Rosen Paradox". *Physics Physique Fizika* 1 (1964). DOI: 10.1103/PhysicsPhysiqueFizika.1.195..

[Ben+14] C. H. Bennett and G. Brassard. "Quantum Cryptography: Public Key Distribution and Coin Tossing". *Theoretical Computer Science* 560 (2014). DOI: 10.1016/j.tcs.2014.05.025.

[Bla01] E. D. Black. "An Introduction to Pound–Drever–Hall Laser Frequency Stabilization". *American Journal of Physics* 69.1 (2001). DOI: 10.1119/1.1286663.

[Bou+99] B. Boulanger, I. Rousseau, J. Feve, M. Maglione, et al. "Optical Studies of Laser-Induced Gray-Tracking in KTP". *IEEE Journal of Quantum Electronics* 35.3 (1999). DOI: 10.1109/3.748831.

[Boy08] R. W. Boyd. *Nonlinear Optics*. 3. ed. Amsterdam: Acad. Press, 2008.

[Bra+05] S. L. Braunstein and P. van Loock. "Quantum Information with Continuous Variables". *Rev. Mod. Phys.* 77.2 (2005).

[Cer+01] N. J. Cerf, M. Lévy, and G. V. Assche. "Quantum Distribution of Gaussian Keys Using Squeezed States". *Physical Review A* 63.5 (2001). DOI: 10.1103/PhysRevA.63.052311.

[Cha+23] J. C. Chapman, A. Miloshevsky, H.-H. Lu, N. Rao, et al. "Two-Mode Squeezing over Deployed Fiber Coexisting with Conventional Communications". *Optics Express* 31.16 (2023). DOI: 10.1364/OE.492539.

[Che+21] J.-P. Chen, C. Zhang, Y. Liu, C. Jiang, et al. "Twin-Field Quantum Key Distribution over a 511 km Optical Fibre Linking Two Distant Metropolitan Areas". *Nature Photonics* 15.8 (2021). DOI: 10.1038/s41566-021-00828-5.

[Cre+99] R. F. Cregan, B. J. Mangan, J. C. Knight, T. A. Birks, et al. "Single-Mode Photonic Band Gap Guidance of Light in Air". *Science* 285.5433 (1999). DOI: `10.1126/science.285.5433.1537`.

[Dua+00] L.-M. Duan, G. Giedke, J. I. Cirac, and P. Zoller. "Inseparability Criterion for Continuous Variable Systems". *Physical Review Letters* 84.12 (2000).

[Ebe13] T. Eberle. *Realization of Finite-Size Quantum Key Distribution Based on Einstein-Podolsky-Rosen Entangled Light*. Ph.D. Thesis. Gottfried Wilhelm Leibniz Universität Hannover, 2013.

[Eck+21] S. Ecker, B. Liu, J. Handsteiner, M. Fink, et al. "Strategies for Achieving High Key Rates in Satellite-Based QKD". *npj Quantum Information* 7.1 (2021). DOI: `10.1038/s41534-020-00335-5`.

[Ein+35] A. Einstein, B. Podolsky, and N. Rosen. "Can Quantum-Mechanical Description of Physical Reality Be Considered Complete?" *Physical Review* 47.10 (1935). DOI: `10.1103/PhysRev.47.777`.

[Eke91] A. K. Ekert. "Quantum Cryptography Based on Bell's Theorem". *Physical Review Letters* 67.6 (1991). DOI: `10.1103/PhysRevLett.67.661`.

[End+25] M. Endo, T. Nomura, T. Sonoyama, K. Takahashi, et al. "High-Rate Four Photon Subtraction from Squeezed Vacuum: Preparing Cat State for Optical Quantum Computation" (2025). DOI: `10.48550/arXiv.2502.08952`. arXiv: `2502.08952`.

[Fej+92] M. Fejer, G. Magel, D. Jundt, and R. Byer. "Quasi-Phase-Matched Second Harmonic Generation: Tuning and Tolerances". *IEEE Journal of Quantum Electronics* 28.11 (1992). DOI: `10.1109/3.161322`.

[Fol+22] G. Foletto, F. Picciariello, C. Agnesi, P. Villoresi, and G. Vallone. "Security Bounds for Decoy-State Quantum Key Distribution with Arbitrary Photon-Number Statistics". *Physical Review A* 105.1 (2022). DOI: `10.1103/PhysRevA.105.012603`.

[Fra+22] G. F. Franklin, J. D. Powell, and M. Workman. *Digital Control of Dynamic Systems*. Ellis-Kagle Press, 2022.

[Fur+12] F. Furrer, T. Franz, M. Berta, A. Leverrier, et al. "Continuous Variable Quantum Key Distribution: Finite-Key Analysis of Composable Security against Coherent Attacks". *Physical Review Letters* 109.10 (2012). DOI: 10.1103/PhysRevLett.109.100502.

[Geh+15] T. Gehring, V. Händchen, J. Duhme, F. Furrer, et al. "Implementation of Continuous-Variable Quantum Key Distribution with Composable and One-Sided-Device-Independent Security against Coherent Attacks". *Nature Communications* 6.1 (2015). DOI: 10.1038/ncomms9795.

[Ger+05] C. Gerry and P. Knight. *Introductory Quantum Optics*. Cambridge University Press, 2005.

[Gla63] R. J. Glauber. "The Quantum Theory of Optical Coherence". *Physical Review* 130.6 (1963). DOI: 10.1103/PhysRev.130.2529.

[Got+01] D. Gottesman and J. Preskill. "Secure Quantum Key Distribution Using Squeezed States". *Physical Review A* 63.2 (2001). DOI: 10.1103/PhysRevA.63.022309.

[Gra+20] M. R. Grace, C. N. Gagatsos, Q. Zhuang, and S. Guha. "Quantum-Enhanced Fiber-Optic Gyroscopes Using Quadrature Squeezing and Continuous-Variable Entanglement". *Physical Review Applied* 14.3 (2020). DOI: 10.1103/PhysRevApplied.14.034065.

[Gro+03] F. Grosshans, G. Van Assche, J. Wenger, R. Brouri, et al. "Quantum Key Distribution Using Gaussian-Modulated Coherent States". *Nature* 421.6920 (2003). DOI: 10.1038/nature01289.

[Gro+13] H. Grote, K. Danzmann, K. L. Dooley, R. Schnabel, et al. "First Long-Term Application of Squeezed States of Light in a Gravitational-Wave Observatory". *Physical Review Letters* 110.18 (2013). DOI: 10.1103/PhysRevLett.110.181101.

[Haj+24] A. A. E. Hajomer, I. Derkach, N. Jain, H.-M. Chin, et al. "Long-Distance Continuous-Variable Quantum Key Distribution over 100-km Fiber with Local Local Oscillator". *Science Advances* 10.1 (2024). DOI: 10.1126/sciadv.adi9474.

[Har+00] M. T. Harrison, S. V. Kershaw, M. G. Burt, A. L. Rogach, et al. "Colloidal Nanocrystals for Telecommunications. Complete Coverage of the Low-Loss Fiber Windows by Mercury Telluride Quantum Dots". *Pure Appl. Chem.* 72 (2000).

[Hir+07] J. Hirohashi, V. Pasiskevicius, S. Wang, and F. Laurell. "Picosecond Blue-Light-Induced Infrared Absorption in Single-Domain and Periodically Poled Ferroelectrics". *Journal of Applied Physics* 101.3 (2007). DOI: 10.1063/1.2434007.

[Hug+02] R. J. Hughes, J. E. Nordholt, D. Derkacs, and C. G. Peterson. "Practical Free-Space Quantum Key Distribution over 10 km in Daylight and at Night". *New Journal of Physics* 4 (2002). DOI: 10.1088/1367-2630/4/1/343.

[Kan+25] P. M. Kannath, G. S. Agarwal, and A. Kumar. "Quantum Sensing with Bright Two-Mode Squeezed Light in a Distributed Network of Gyroscopes". *Physical Review Research* 7.4 (2025). DOI: 10.1103/dtrj-whsb.

[Kan21] H. Kanamori. "Transmission Loss of Optical Fibers; Achievements in Half a Century". *IEICE Transactions on Communications* E104.B.8 (2021). DOI: 10.1587/transcom.2020EBI0002.

[Kao+66] K. C. Kao and G. A. Hockham. "Dielectric-Fibre Surface Waveguides for Optical Frequencies". *Proceedings of the Institution of Electrical Engineers (IEE)* 113.7 (1966).

[Koa] Koax24.de. www.koax24.de/uebersichten/kabelvergleich. (Visited on Jan. 8, 2026).

[Lia+17] S.-K. Liao, W.-Q. Cai, W.-Y. Liu, L. Zhang, et al. "Satellite-to-Ground Quantum Key Distribution". *Nature* 549.7670 (2017). DOI: 10.1038/nature23655.

[Loi+92] G. M. Loiacono, D. N. Loiacono, T. McGee, and M. Babb. "Laser Damage Formation in KTiOPO4 and KTiOAsO4 Crystals: Grey Tracks". *Journal of Applied Physics* 72.7 (1992). DOI: 10.1063/1.351520.

[Mad+12] L. S. Madsen, V. C. Usenko, M. Lassen, R. Filip, and U. L. Andersen. "Continuous Variable Quantum Key Distribution with Modulated Entangled States". *Nature Communications* 3.1 (2012). DOI: 10.1038/ncomms2097.

[McK+05] K. McKenzie, E. E. Mikhailov, K. Goda, P. K. Lam, et al. "Quantum Noise Locking". *Journal of Optics B: Quantum and Semiclassical Optics* 7.10 (2005). DOI: 10.1088/1464-4266/7/10/032.

[Meh+10] M. Mehmet, T. Eberle, S. Steinlechner, H. Vahlbruch, and R. Schnabel. "Demonstration of a Quantum-Enhanced Fiber Sagnac Interferometer". *Optics Letters* 35.10 (2010). DOI: 10.1364/OL.35.001665.

[Ngu+26] H. Q. Nguyen, I. Derkach, A. nag Oruganti, A. A. E. Hajomer, et al. "Practical Continuous-Variable Quantum Key Distribution with Squeezed Light" (2026). DOI: 10.48550/arXiv.2506.19438. arXiv: 2506.19438.

[Noi] Noisy Labs. www.noisy-labs.com. (Visited on May 1, 2026).

[Num+23] E. Numkam Fokoua, S. Abokhamis Mousavi, G. T. Jasion, D. J. Richardson, and F. Poletti. "Loss in Hollow-Core Optical Fibers: Mechanisms, Scaling Rules, and Limits". *Advances in Optics and Photonics* 15.1 (2023). DOI: 10.1364/AOP.470592.

[Oel+16] E. Oelker, G. Mansell, M. Tse, J. Miller, et al. "Ultra-Low Phase Noise Squeezed Vacuum Source for Gravitational Wave Detectors". *Optica* 3.7 (2016). DOI: 10.1364/OPTICA.3.000682.

[Par70] J. L. Park. "The Concept of Transition in Quantum Mechanics". *Foundations of Physics* 1.1 (1970). DOI: 10.1007/BF00708652.

[Peu+14] C. Peuntinger, B. Heim, C. R. Müller, C. Gabriel, et al. "Distribution of Squeezed States through an Atmospheric Channel". *Physical Review Letters* 113.6 (2014). DOI: 10.1103/PhysRevLett.113.060502.

[Pir+17] S. Pirandola, R. Laurenza, C. Ottaviani, and L. Banchi. "Fundamental Limits of Repeaterless Quantum Communications". *Nature Communications* 8.1 (2017). DOI: 10.1038/ncomms15043.

[Pol+92] E. S. Polzik, J. Carri, and H. J. Kimble. "Atomic Spectroscopy with Squeezed Light for Sensitivity beyond the Vacuum-State Limit". *Applied Physics B Photophysics and Laser Chemistry* 55.3 (1992). DOI: 10.1007/BF00325016.

[Qin+19] J. Qin, J. Cheng, S. Liang, Z. Yan, et al. "Transferring of Continuous Variable Squeezed States in 20 km Fiber". *Applied Sciences* 9.12 (2019). DOI: 10.3390/app9122397.

[Rei89] M. D. Reid. "Demonstration of the Einstein-Podolsky-Rosen Paradox Using Nondegenerate Parametric Amplification". *Physical Review A* 40.2 (1989). DOI: 10.1103/PhysRevA.40.913.

[Sam12] A. Samblowski. *State Preparation for Quantum Information Science and Metrology*. Ph.D. Thesis. Gottfried Wilhelm Leibniz Universität Hannover, 2012.

[Sch+18] A. Schönbeck, F. Thies, and R. Schnabel. "13 dB Squeezed Vacuum States at 1550 Nm from 12 mW External Pump Power at 775 nm". *Optics Letters* 43.1 (2018). DOI: 10.1364/OL.43.000110.

[Sch+22] R. Schnabel and A. Schonbeck. "The "Squeeze Laser"". *IEEE Transactions on Quantum Engineering* 3 (2022). DOI: 10.1109/TQE.2022.3224686.

[Sch18] A. Schönbeck. *Compact Squeezed-Light Source at 1550 nm*. Ph.D. Thesis. Universität Hamburg, 2018.

[Slu+85] R. E. Slusher, L. W. Hollberg, B. Yurke, J. C. Mertz, and J. F. Valley. "Observation of Squeezed States Generated by Four-Wave Mixing in an Optical Cavity". *Physical Review Letters* 55.22 (1985). DOI: 10.1103/PhysRevLett.55.2409.

[Sul+22] I. Suleiman, J. A. H. Nielsen, X. Guo, N. Jain, et al. "40 km Fiber Transmission of Squeezed Light Measured with a Real Local Oscillator". *Quantum Science and Technology* 7.4 (2022). DOI: 10.1088/2058-9565/ac7ba1.

[Tay+13] M. A. Taylor, J. Janousek, V. Daria, J. Knittel, et al. "Biological Measurement beyond the Quantum Limit". *Nature Photonics* 7.3 (2013). DOI: 10.1038/nphoton.2012.346.

[Toh+25] B. Tohermes, S. Verclas, J. N. Hohmann, D. Haupt, and R. Schnabel. "Directly Measured Squeeze Factors over GHz Bandwidth from Monolithic PPKTP Resonators". *New Journal of Physics* 27.9 (2025). DOI: 10.1088/1367-2630/ae0512.

[Toh25] B. Tohermes. *Generation and Fiber-Based Distribution of High-Bandwidth Entanglement for Continuous Variable Quantum Key Distribution*. Ph.D. Thesis. Universität Hamburg, 2025.

[Tse+19] M. Tse, H. Yu, N. Kijbunchoo, A. Fernandez-Galiana, et al. "Quantum-Enhanced Advanced LIGO Detectors in the Era of Gravitational-Wave Astronomy". *Physical Review Letters* 123.23 (2019). DOI: 10.1103/PhysRevLett.123.231107.

[Urs+07] R. Ursin, F. Tiefenbacher, T. Schmitt-Manderbach, H. Weier, et al. "Entanglement-Based Quantum Communication over 144 km". *Nature Physics* 3.7 (2007). DOI: 10.1038/nphys629.

[Vah+08] H. Vahlbruch, M. Mehmet, S. Chelkowski, B. Hage, et al. "Observation of Squeezed Light with 10-dB Quantum-Noise Reduction". *Physical Review Letters* 100.3 (2008). DOI: 10.1103/PhysRevLett.100.033602.

[Vah+16] H. Vahlbruch, M. Mehmet, K. Danzmann, and R. Schnabel. "Detection of 15 dB Squeezed States of Light and Their Application for the Absolute Calibration of Photoelectric Quantum Efficiency". *Physical Review Letters* 117.11 (2016). DOI: 10.1103/PhysRevLett.117.110801.

[Ver+26] S. Verclas, C. Darsow-Fromm, B. Tohermes, and R. Schnabel. "Fiber Distribution of Phase-Stabilized GHz-bandwidth Squeezed Vacuum States of Light between Two Buildings". *Optica Quantum* 4.1 (2026). DOI: 10.1364/OPTICAQ.567418.

[Wal+08] D. F. Walls and G. J. Milburn. *Quantum Optics*. 2nd ed. Berlin: Springer, 2008.

[Wal+16] N. Walk, S. Hosseini, J. Geng, O. Thearle, et al. "Experimental Demonstration of Gaussian Protocols for One-Sided Device-Independent Quantum Key Distribution". *Optica* 3.6 (2016). DOI: 10.1364/OPTICA.3.000634.

[Woo+82] W. K. Wootters and W. H. Zurek. "A Single Quantum Cannot Be Cloned". *Nature* 299.5886 (1982). DOI: 10.1038/299802a0.

[Wu+86] L.-A. Wu, H. J. Kimble, J. L. Hall, and H. Wu. "Generation of Squeezed States by Parametric Down Conversion". *Physical Review Letters* 57.20 (1986). DOI: 10.1103/PhysRevLett.57.2520.

[Yan+24] J. Yang, Z. Jiang, F. Benthin, J. Hanel, et al. "High-Rate Intercity Quantum Key Distribution with a Semiconductor Single-Photon Source". *Light: Science & Applications* 13.1 (2024). DOI: 10.1038/s41377-024-01488-0.

[Yin+20] J. Yin, Y.-H. Li, S.-K. Liao, M. Yang, et al. "Entanglement-Based Secure Quantum Cryptography over 1,120 Kilometres". *Nature* 582.7813 (2020). DOI: 10.1038/s41586-020-2401-y.

[Zah+24] M. Zahidy, M. T. Mikkelsen, R. Müller, B. Da Lio, et al. "Quantum Key Distribution Using Deterministic Single-Photon Sources over a Field-Installed Fibre Link". *npj Quantum Information* 10.1 (2024). DOI: 10.1038/s41534-023-00800-x.

[Zan21] J. Zander. *Squeezed and Entangled Light: From Foundations of Quantum Mechanics to Quantum Sensing*. Ph.D. Thesis. Universität Hamburg, 2021.

[Zha+20] Y. Zhang, Z. Chen, S. Pirandola, X. Wang, et al. "Long-Distance Continuous-Variable Quantum Key Distribution over 202.81 km of Fiber". *Physical Review Letters* 125.1 (2020). DOI: 10.1103/PhysRevLett.125.010502.

Resources

I used several tools to achieve the results presented in this thesis and list them here. For the calculations of mode matchings, I used the program JamMT, version 0.24, programmed by André Thüring and Nico Lastzka. Drawings of the setups and other pictures were generated using Inkscape and the component library designed by Alexander Franzen. For data analysis and plot generation, I used Python3, running in a JupyterLab notebook. I used several electrical components in this setup, that were designed and built by former group members. The thesis was written using Overleaf/ShareLaTeX, licensed by the Universität Hamburg.

List of publications

2025
B. Tohermes, S. Verclas, J. N. Hohmann, D. Haupt, and R. Schnabel
"Directly Measured Squeeze Factors over GHz Bandwidth from Monolithic PPKTP Resonators",
New Journal of Physics 27.9 (2025)
DOI: 10.1088/1367-2630/ae0512

2026
S. Verclas, C. Darsow-Fromm, B. Tohermes, and R. Schnabel
"Fiber Distribution of Phase-Stabilized GHz-Bandwidth Squeezed Vacuum States of Light between Two Buildings",
Optica Quantum 4.1 (2026)
DOI: 10.1364/OPTICAQ.567418

Danksagung

Am Ende tragen immer zahlreiche Menschen zu einer erfolgreichen Promotion bei und ich möchte mich an dieser Stelle dafür bedanken.

Zu allererst gilt mein Dank natürlich Roman. Ich habe alle drei Abschlussarbeiten in deiner Gruppe gemacht und denke allein das zeigt, wie viel Spaß es mir gemacht hat Teil dieser Gruppe zu sein. Für die interessanten Projekte, die offene Tür und die Möglichkeit auch auf zahlreiche Konferenzen zu fahren möchte ich dir sehr herzlich danken!

Meinen beiden Gutachtern und dem ganzen Prüfungskomitee danke ich für die Unterstützung bei meinem recht ambitionierten Zeitplan am Ende.

Daran schließt sich auch der Dank an die Gruppe an. So viel Unterstützung, Hilfsbereitschaft und Zusammenhalt ist bestimmt nicht selbstverständlich und insbesondere meinen (wechselnden) Büromitbewohnern danke ich für die Diskussionen, Unterhaltungen und gute Atmosphäre.

Bei Bene möchte ich bedanken für die hervorragende und geduldige Betreuung, auch über die Masterarbeit hinaus. Viele Stunden im Labor, im Kriechkeller, auf dem Boot oder mit Musik haben mir stets viel Spaß gemacht.

Besonderen Dank möchte ich auch an Mikhail aussprechen. Dein Wissen und die freundliche Hilfsbereitschaft mit der du es jederzeit vermittelst sind eine riesengroße Hilfe wenn man gerade wieder daran verzweifelt sein Experiment zu verstehen. Ganz zu schweigen von deinem Feedback für meine Theoriekapitel, die du in Rekordzeit durchgearbeitet hast und damit den sehr sportlichen Zeitplan meiner Promotion ermöglicht hast.

Stephan und Chris möchte ich danken für den Code für meine Locks. Ohne euren Input und eure Hilfe hätte es weder so schnell noch so gut funktioniert und auch die stetig wechselnden Anforderungen, die mir mein Experiment immer wieder offenbart hat konnten stets umgesetzt werden.

Chris danke ich außerdem für so viel Zeit in der Kletterhalle, im Gebirge und als am Ende die zeitkritische Phase begann auch im Labor oder bei der Unterstützung mit Layoutproblemen und ominösen Fehlermeldungen.

Nahezu 24/7 IT Unterstützung ist für ein Promotionsvorhaben extrem nützlich.

Bei Lina möchte ich mich für die regelmäßigen Klettersessions und auch den ersten Ausflug an den Fels bedanken. In all dem Chaos war es oft das Highlight meiner Woche.

Ich bin sehr froh über die Unterstützung meiner Familie - obwohl vielleicht weder der Inhalt meines Weges noch der Weg selbst für euch nachvollziehbar waren, konnte ich fast immer mit bedingungslosm Rückhalt rechnen und in der stressigsten Zeit sogar mit Quiche und Erdbeeren.

Hierzu gehört auch mein Patenonkel Andreas und seine Familie. Nicht nur für das Buch mit Antworten auf wirklich alle Fragen, sondern auch für die zahlreichen Mittagessen, Abendessen, Kuchenrunden und Gespräche über Alles außer Gott und die Welt möchte ich mich herzlich bedanken. Eine solche Anlaufstation mit Essensversorgung in fußläufiger Nähe zum Labor hat so manchen finsteren Tag hell gemacht und mir oft die nötige Kraft und den Mut zum Weitermachen gegeben.

Dem Mo danke ich für so Vieles - Beratung (fachlich wie nicht fachlich), Unterstützung (von Mocheinsätzen über Kiwhirettungen bis hin zu passenden Situationseinordnungen), Cornrad, Städtebesichtigungen, Segeltörns und stumpfen Kommentaren über die ich noch tagelang lachen kann. Spitze.

Eidesstattliche Versicherung / Declaration on oath

Hiermit versichere ich an Eides statt, die vorliegende Dissertationsschrift selbst verfasst und keine anderen als die angegebenen Hilfsmittel und Quellen benutzt zu haben.

Sofern im Zuge der Erstellung der vorliegenden Dissertationsschrift generative Künstliche Intelligenz (gKI) basierte elektronische Hilfsmittel verwendet wurden, versichere ich, dass meine eigene Leistung im Vordergrund stand und dass eine vollständige Dokumentation aller verwendeten Hilfsmittel gemäß der Guten wissenschaftlichen Praxis vorliegt. Ich trage die Verantwortung für eventuell durch die gKI generierte fehlerhafte oder verzerrte Inhalte, fehlerhafte Referenzen, Verstöße gegen das Datenschutz- und Urheberrecht oder Plagiate.

Die eingereichte schriftliche Fassung entspricht der auf dem elektronischen Speichermedium.

Die Dissertation wurde in der vorgelegten oder einer ähnlichen Form nicht schon einmal in einem früheren Promotionsverfahren angenommen oder als ungenügend beurteilt.

Hamburg, den 14.06.2026

Unterschrift des Doktoranden